Formation and evolution of discs and bulges through cosmic time in CANDELS

Berta Margalef Bentabol



The University of Nottingham

Thesis submitted to the University of Nottingham
for the degree of Doctor of Philosophy, May 2017

"Astronomy compels the soul to look upwards and leads us from this world to another."

– Plato

Supervisor: Prof. Christopher Conselice

Examiners: Dr. Mark Swinbank
Prof. Frazer Pearce

Abstract

We examine a sample of 1495 galaxies in the UDS/CANDELS field to determine the evolution of two component galaxies, including bulges and discs, within massive galaxies at the epoch $1 < z < 3$ when the Hubble sequence forms. We fit all of our galaxies' light profiles with a single Sérsic fit, as well as with a combination of exponential and Sérsic profiles. The latter is done in order to describe a galaxy with an inner and an outer component, or bulge and disc component. We develop and use three classification methods (visual, F-test and the RFF) to separate our sample into 1-component galaxies (disc/spheroids-like galaxies) and 2-component galaxies (galaxies formed by an 'inner part' or bulge and an 'outer part' or disc). We then compare the results from using these three different ways to classify our galaxies. We find that the fraction of galaxies selected as 2-component systems increases on average 50% from the lowest mass bin to the most massive galaxies, and decreases with redshift by a factor of 4 from $z = 1$ to $z = 3$. We find that single Sérsic 'disc-like' galaxies have the highest relative number densities at all redshifts, and that 2-component galaxies have the greatest increase and become at par with Sérsic discs by $z = 1$. We also find that the systems we classify as 2-component galaxies have an increase in the sizes of their outer components, or 'discs', by about a factor of 3 from $z = 3$ to $z = 1.5$, while the inner components or 'bulges' stay roughly the same size. This suggests that these systems are growing from the inside out, whilst the bulges or protobulges are in place early in the history of these galaxies.

We then extend our study to a broader range in wavelength, using all available bands from the *HST* in the UDS/CANDELS field (H, J, i and V band) in order to calculate rest-frame magnitudes, stellar masses and SFRs for each component. We show that galaxies which are better fit as 2-component systems can have the stellar masses and star formation rates of their inner and outer components measured accurately. We examine the position of our

inner/outer components in the UVJ diagram, finding that the majority of both inner and outer components lie in the star forming region (68% and 90% respectively), but that the inner portions, the likely forming bulges, are dominated by dusty star formation. Furthermore, we show that the outer components of these forming galaxies have a higher star formation rate, and the relative star formation rate increases in outer components (or discs) as redshift decreases. On the other hand, the relative stellar mass of both components remains statistically constant at $z < 3$. This suggests that mass formed in the outer components of galaxies is being transferred to the inner components. Finally, we find that the presence of an AGN is more common in both 1-component spheroid-like galaxies and 2-component systems ($13 \pm 3\%$ and $11 \pm 2\%$) than in 1-component disc-like galaxies ($3 \pm 1\%$), demonstrating that the formation of a central inner component likely triggers the formation of the central massive black holes in these galaxies.

Lastly we explore the properties of spiral galaxies in UDS, GOODS-S and COSMOS CANDELS fields. We use the CANDELS Galaxy Zoo classification to select spiral galaxies, clumpy spiral and smooth discs. We show that galaxies classified as spirals decrease with increasing redshift, although part of this trend is due to redshift effects. After correcting such effects, we find that the number density of spirals galaxies increases by a factor of 14 ± 2 from $z = 2.5$ to $z = 0.5$. We find morphological differences between spiral galaxies and smooth discs, with the former being more 'disky' and asymmetric, and the latter being more centrally concentrated. We show that spiral galaxies, and in particular clumpy spirals, dominate the star formation at all redshifts, with average SFRs of $SFR = 40 \pm 3\ M_{\odot}\mathrm{yr}^{-1}$ and $SFR = 50 \pm 7\ M_{\odot}\mathrm{yr}^{-1}$ respectively, and that there is no benefit of having a large mass to produce spiral structures.

Published work

Much of the work in this thesis has been presented in several papers:

I **Margalef-Bentabol B.**, Conselice C. J., Mortlock A., Hartley W., Duncan K., Ferguson H. C., Dekel A., Primack J. R., 2016. *The formation of bulges, discs and two-component galaxies in the CANDELS Survey at* $z < 3$, MNRAS, 461, 2728.

II **Margalef-Bentabol B.**, Conselice C. J., Mortlock A., Hartley W., Duncan K., Kennedy R., Kocevski D. D., Hasinger G., 2017. *Properties of bulges and discs systems at* $z < 3$ *in CANDELS*, submitted to MNRAS.

III **Margalef-Bentabol B.** at al. *Properties of spiral galaxies at high redshift*, in preparation.

IV Lange, R., Moffett, A. J., Driver, S. P.; Robotham, Aaron S. G., Lagos, C. P., Kelvin, L. S., Conselice, C. J., **Margalef-Bentabol, B.**, et al. 2016. *Galaxy And Mass Assembly (GAMA):* $M_* - R_e$ *relations of* $z = 0$ *bulges, discs and spheroids*, MNRAS, 462, 1470.

Paper I contains the work detailed in Chapter 2. Paper II describes the work presented in Chapter 3. Paper III is a work in progress and is described in Chapter 4.

Acknowledgements

I would like to thank the STFC, the IAC and the University of Nottingham for sponsoring my Ph.D.

The first person I would like to thank is my supervisor, Christopher Conselice. Thank you for your support throughout my time in Nottingham and for your encouragement and guidance. I would also like to thank the rest of the staff in the department, for creating a friendly environment to work, in particular to Steven, for your disposition to always discuss my work and to Meghan, for your compassion and understanding.

Thanks to my science family for making the Ph.D. a bit less solitary: Alice, Jamie, Ken, Carl, Dongyao, Rach and Andrea. With you I was able to share my work and exchange opinions. You all have been very helpful during my Ph.D. Particular thanks to Will and Boris for all your help during the first months, and to Fernando for your patience and advise.

I would also like to thank my officemates for making our office the best one in the department: Kshitija, Lizzie, Rach, Carl, Evelyn, Kate, Julian, Rachel, Tom... Thanks for all the laughs and interesting conversations about science and, more often, about any other topic.

Thanks to all the friends I have made during this four years, especially Kshitija, Bruno, Ismael, Miguel, Rach, Charuta and Felipe. You have been a huge support trough the Ph.D. Thanks for not only being there to share astronomy and science but also for making my stay in Nottingham unforgettable. Thanks for all the memories both inside and outside the department. Thank you Kshitija for being my best friend and share with me hard times and success.

Thanks to the many of you that in any way have contributed to make the Ph.D. journey more enjoyable. Thanks for creating a wonderful atmosphere in the department, and for all the good times we have shared: pub on Fridays, astro-outings, Christmas celebrations, Eurovision parties, house parties and many more moments. Thanks to the 'coffee club' for the most needed breaks from work.

Finally, but most important, I would like to thank my family. Thanks mum and dad for always believing in me and making it possible for me to be here today. Thanks Juan for your countless help and discussions about my work, and for always responding when I needed you. Thanks Carla for giving me confidence and always being there when I needed your help or advise.

Contents

Preamble **I**

Abstract I

Published work III

Acknowledgements IV

List of Figures X

List of Tables XIV

1 Introduction **1**

1.1 Cosmology and our current view of the Universe 2

1.2 Galaxies in the Λ-CDM framework 5

1.3 Physical processes of galaxy formation 7

1.4 Galaxy classification 9

1.5 Bimodality of galaxies 11

1.5.1 Morphology and structure 11

1.5.2 Colour and star formation history 12

1.6 High redshift universe and galaxy evolution 13

1.7 Bulges and discs 16

1.8 Aim of the thesis and structure 17

2 The evolution of discs and bulges **19**

2.1 Introduction . . . 19
2.2 Data . . . 21
2.2.1 Imaging . . . 21
2.2.2 Redshifts and stellar masses . . . 23
2.3 Method . . . 25
2.3.1 One component model . . . 26
2.3.2 Two component model . . . 26
2.3.3 Morphological K-correction . . . 27
2.3.4 Classification . . . 29
2.4 Results . . . 36
2.4.1 Method comparison and basic trends . . . 37
2.4.2 Number density evolution of galaxy components . . . 38
2.4.3 Total stellar mass density . . . 41
2.4.4 The size evolution of components . . . 44
2.5 Conclusions . . . 49

3 The star formation history of discs and bulges 52

3.1 Introduction . . . 52
3.2 Data . . . 54
3.2.1 Imaging . . . 54
3.2.2 Sample of galaxies . . . 54
3.3 Method . . . 55
3.3.1 Structural parameters . . . 55
3.3.2 Multiwavelengh study . . . 56
3.3.3 SEDs . . . 56
3.3.4 Star formation rates . . . 59

3.4 Results . . . 61
3.4.1 Colours . . . 61
3.4.2 Star formation rates of inner and outer components . . . 66
3.4.3 Stellar masses of components . . . 71
3.4.4 Presence of AGN . . . 72
3.5 Conclusions . . . 73

4 High redshift spirals 76
4.1 Introduction . . . 76
4.2 Data . . . 78
4.2.1 Redshifts and stellar masses . . . 79
4.3 Method . . . 80
4.4 Results . . . 84
4.4.1 Fractions . . . 84
4.4.2 Stellar mass comparison . . . 90
4.4.3 UVJ diagram . . . 90
4.4.4 Structure . . . 91
4.4.5 Star formation activity . . . 98
4.5 Conclusions . . . 99

5 Summary and future work 102

A Simulations of high redshift galaxies 105
A.1 Details of the simulations . . . 105
A.2 Results . . . 106

B Extended photometry 112

Bibliography 117

List of Figures

1.1 Cosmic microwave background 4

1.2 Illustris simulation 6

1.3 Hubble's original tuning-fork 9

1.4 Sérsic profile 11

1.5 Bimodality in g-r colour and colour-magnitude diagram 13

1.6 Evolution of SFR density with redshift 15

2.1 Stellar mass and effective radius versus redshift 23

2.2 Comparison between effective radius and Sérsic index obtained in the J-band and H-band 28

2.3 Example of the visual classification method 30

2.4 Examples of galaxies visually classified as 1-component, 2-component and peculiar galaxies 31

2.5 F-score technique used in the RFF method 35

2.6 RFF method applied to the whole sample 35

2.7 Fraction of 2-component galaxies as a function of stellar mass 38

2.8 Fraction of 2-component galaxies as a function of redshift 38

2.9 Number density $n_{\rm d}(z)$ as a function of redshift 39

2.10 Total number density evolution 42

2.11 Ratio of the number density of red and blue galaxies 42

2.12 Mass density as a function of redshift 44
2.13 Mean mass density evolution 45
2.14 Size evolution 46
2.15 Evolution of the ratio between the sizes of discs and bulges 47
2.16 Evolution of the ratio between the flux of discs and bulges 48
2.17 Evolution of galaxy size with redshift in comparison with nearby galaxies 49

3.1 Stellar mass versus redshift 55
3.2 Comparison between stellar masses 59
3.3 Comparison between the stellar masses and SFRs obtained from the 1 and 2-component fitting 59
3.4 UVJ diagram for 1-component galaxies 62
3.5 UVJ diagram for bulges and discs of 2-component galaxies 63
3.6 Rest-frame $U - V$ colour as a function of stellar mass 64
3.7 Rest-frame $U - V$ colour as a function of redshift 65
3.8 SFR as a function of stellar mass 67
3.9 Ratio between SFR of bulges and discs as a function of stellar mass . . . 68
3.10 Ratio between SFR of bulges and discs as a function of redshift 69
3.11 Ratio between sSFR of bulges and discs as a function of redshift 69
3.12 sSFR as a function of stellar mass and morphology 70
3.13 Ratio between stellar mass of bulges and discs as a function of redshift . . 71
3.14 Stellar mass of bulges and discs as a function of redshift 72
3.15 SFR distribution for galaxies with and without AGN 73

4.1 The decision tree of Galaxy Zoo CANDELS 81
4.2 Comparison between smooth discs selected visually and smooth galaxies with $B/T < 0.5$ 83

4.3 Distribution of B/T for smooth discs selected visually and smooth galaxies with $B/T < 0.5$ . . . 84
4.4 Fraction of different types of discs as a function of redshift . . . 85
4.5 Redshifted spiral galaxies . . . 86
4.6 Surface brightness comparison . . . 87
4.7 Fraction of recovered spiral galaxies . . . 87
4.8 Corrected fraction of spiral galaxies . . . 88
4.9 Number density evolution of the different types of discs . . . 88
4.10 Examples of spiral discs at $2 < z < 3$ . . . 89
4.11 Examples of clumpy spirals at $2 < z < 3$ . . . 89
4.12 Stellar mass versus redshift . . . 90
4.13 UVJ diagram at different redshif bins . . . 92
4.14 Rest-frame $U - V$ colour as a function of redshift . . . 93
4.15 Evolution of the structural parameters . . . 94
4.16 Evolution of the CAS parameters . . . 96
4.17 Asymmetry versus clumpiness . . . 97
4.18 Concentration versus asymmetry . . . 97
4.19 SFR and sSFR as a function of redshift . . . 98
4.20 SFR as a function of stellar mass . . . 100

A.1 Comparison of the surface brightness of the HRS galaxies with the HRO galaxies . . . 106
A.2 Comparison between the results from the fitting for the HRS galaxies versus the LRO sample . . . 107
A.3 Comparison between the magnitude of the components for HRS and LRO galaxies . . . 109

A.4 Comparison between the effective radii of the components for HRS and LRO galaxies 110

A.5 Comparison of the fraction of 2-component galaxies between observations and simulations 111

A.6 Fraction of 2-component galaxies as a function of mass for the HRS galaxies 111

B.1 Comparison between the computed rest-frame magnitudes obtained using 4 and 17 bands 113

B.2 Comparison between the SFRs obtained using 4 and 17 bands 114

B.3 Comparison between the stellar mass obtained using 4 and 17 bands . . . 114

B.4 B/T flux ratio as a function of wavelength 116

B.5 B/T ratio between the rest-frame magnitudes of 2-component galaxies . 116

List of Tables

2.1 Parameters of the fittings to the mean number density 40

2.2 Parameters of the fittings to the mean mass density 43

3.1 Fraction of galaxy components that are passive and star forming 62

4.1 Fraction of galaxies with different disc classifications that are passive and star forming 91

A.1 Fraction of 2-component galaxies selected by the three methods for different subsample of galaxies. 107

Chapter 1

Introduction

The Galaxy we live in, the Milky Way, is just one of the about 2 trillion estimated galaxies in the observed Universe (Conselice *et al.* 2016). However, less than a century ago scientists still believed that our Galaxy was the whole Universe. By the end of the eighteenth century astronomers had already discovered a number of astronomical objects referred as 'nebulae', which differ from stars in being fuzzy and extended. Around 100 of such objects were first catalogued by Messier between 1771 and 1784. A couple of years later, Caroline and William Herschel carried out a more detailed search of nebulae. The number of nebular object was extended by John Herschel to 5079 and published in the *General Catalogue of Nebulae and Clusters of Stars* (CG) by 1864. However, the nature of nebulae was controversial for many years, with some scientists arguing that they were objects within the Milky Way and others advocating for an extragalactic origin, with nebulae being seen as individual 'island universe', just like the Milky Way. The debate continued until 1925, when Edwin Hubble was able to resolve stars (in particular a class of variable stars called Cepheids) in the spiral nebulae Andromeda, and showed, from distances estimated form these Cepheids variables, that Andromeda was outside the Milky Way (Hubble 1925). Hubble's discovery changed the view of our Universe and marked the beginning of extragalactic astronomy.

1.1 Cosmology and our current view of the Universe

The evolution of space-time is governed by the theory of General Relativity (Einstein 1916)

$$R_{ab} - \frac{1}{2}R \cdot g_{ab} = \frac{8\pi G}{c^4}T_{ab}. \tag{1.1}$$

where g_{ab} is the metric tensor, R_{ab} and R are the Ricci tensor and curvature scalar, respectively, associated with the metric, G the gravitational constant, c the speed of light and T_{ab} the energy-momentum tensor.

Since Albert Einstein established this theory, scientists have been looking to construct mathematical models of the Universe as a whole. The current prevailing model is the Big Bang cosmological model.

The Big Bang theory established that the Universe was once (about 13.7 billion years ago) very dense and hot, and since then it has expanded becoming less dense, and cooler. The basic equations for this cosmological model come directly from Einstein's General Relativity under two key assumptions: that the distribution of matter and energy in the Universe is homogeneous, and that the distribution is isotropic – that is, the Universe looks the same everywhere and in every direction. The combination of these assumptions is referred to as the 'cosmological principle'.

In a first instance Einstein assumed that the Universe had to be static. In order to achieve that he included the additional term Λg_{ab} to the Einstein equation, where Λ is known as the 'cosmological constant'. Later, Alexander Friedmann (Friedmann 1922) and then Georges Lemaître (Lemaître 1927) realizing that this solution was unstable obtained the mathematical and physical description of an expanding Universe, in agreement with General Relativity. These theories were endorsed by Hubble's observations in 1929, when he noticed that galaxies are moving away from us in all directions. He showed that the recession velocities of galaxies were proportional to their distance (Hubble 1929; Hubble & Humason 1931), demonstrating that our Universe is expanding. As the Universe expands, the light waves are stretched out and the energy is reduced. This makes the light that reaches us from galaxies to be redshifted. In conclusion, galaxies are simply being carried along with the expansion of the space between them.

Since the Universe is expanding, the idea that it must have been denser and also hotter at earlier times naturally arises. The Big Bang theory does not include the very beginning of the Universe, it only tracks it back to a point where it was extremely hot and dense. In this limit, temperatures and densities were high enough that protons and neutrons existed as free particles, not bound up in atomic nuclei. About 2-3 minutes after the Big Bang the era of primordial nucleosynthesis started, when the expanding Universe had cooled enough so that protons and neutrons could fuse, producing mainly helium (^{3}He, ^{4}He), with some deuterium, lithium and beryllium. The reactions only lasted briefly due to the fact that the Universe's temperature and density were dropping rapidly as it expanded, until fusion was no longer possible. Precise predictions can be made about the relative abundance of the light elements from the primordial nucleosynthesis: about 24% of the ordinary matter in the Universe should be helium produced during this epoch, and this is in very good agreement with observations, providing strong support for the Big Bang theory (Olive & Skillman 2004).

After the primordial nucleosynthesis, the Big Bang theory predicts that the Universe was full of a very hot and dense plasma made of free nuclei and electrons. In such an environment light cannot travel freely as photons are constantly scattering off of charged particles. As the Universe expanded, it cooled to the point that electrons and nuclei could form atoms (recombination). Since atoms are electrically neutral and only interact with photons of a particular energy, most photons were suddenly able to travel much larger distances without interacting with any matter at all (decoupling of matter and radiation). The Universe became transparent and photons from that time have been moving freely through the Universe since. This relic radiation from the early hot Universe is known as the cosmic microwave background radiation (CMB, Figure 1.1). The CMB was first observed by Penzias and Wilson in 1965. While investigating the properties of atmospheric noise, they found a uniform background at microwave frequencies which could not be explained by instrumental noise or any known radio source. The CMB was shown to be isotropic and to have a temperature of about 2.7K, which is in the range predicted by the Big Bang theory (Penzias & Wilson 1965; Dicke *et al.* 1965). The discovery of the CMB established the Big Bang as the standard cosmological model.

The Big Bang theory became very successful as it predicts and explains many observables of the primitive Universe. However, there are some limitations, and problems that are

based solely on this theory cannot be explained, such as the horizon and flatness problem. The horizon problem arises from the fact that the CMB radiation temperatures throughout the Universe are almost exactly the same in every direction. Two regions can have the same conditions if at some point they were close enough for information to be exchanged between them, so that they can reach an equilibrium. However, distant regions in opposite directions of the sky are so far apart that, assuming standard Big Bang expansion, they could never have been in causal contact with each other. This is because the light travel time between them exceeds the age of the Universe. In fact, some of the regions will be forever disconnected as evidenced by the emergence of an event horizon in this kind of universe (Margalef-Bentabol, Margalef-Bentabol & Cepa 2012). Yet when astronomers look in opposite directions, they see that the microwave background looks the same to very high precision, which is very difficult to explain without assuming that somehow all the regions of the known Universe were casually connected once.

The flatness problem refers to observations showing that the geometry of the Universe is nearly flat, with the density parameter (or flatness parameter) Ω very close to 1. But under the Big Bang cosmology any curvature (positive or negative) would rapidly grow with time. Therefore, the fact that the curvature observed today is so close to being flat implies that in the first seconds of the Big Bang it must have been precisely flat ($\Omega = 1$) which seems such a rather special case.

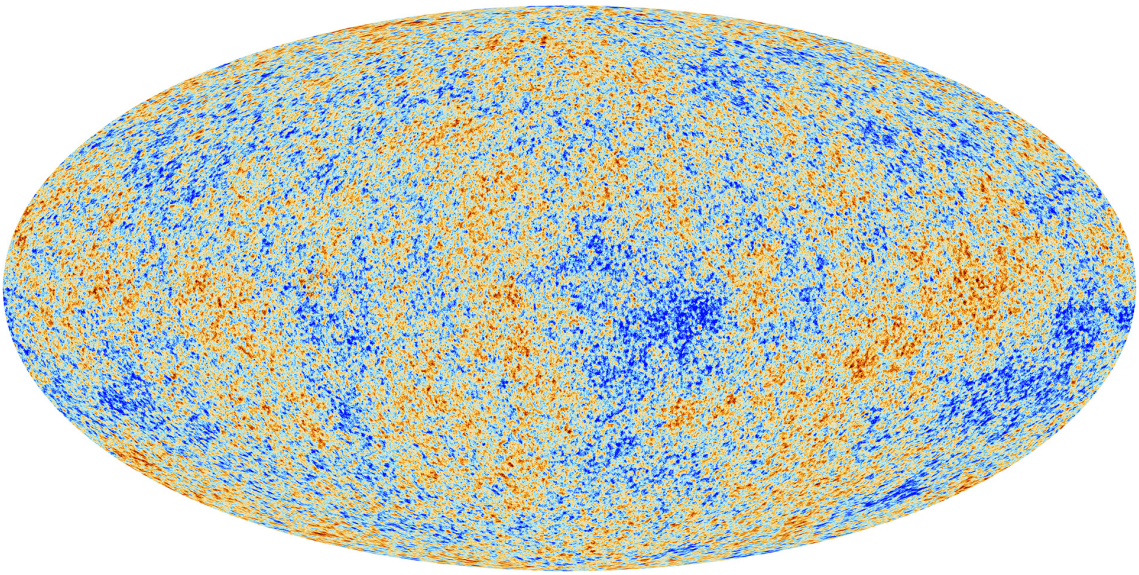


Figure 1.1: The anisotropies of the Cosmic Microwave Background (CMB) as observed by Planck. Credit to ESA and the Planck Collaboration.
http://www.esa.int/spaceinimages/Images/2013/03/Planck_CMB

To address these problems, a mechanism called 'Inflation' was introduced by Guth in 1981, although it is still a matter of debate. In the inflationary model (Guth 1981), our Universe starts out as a rapidly expanding bubble of pure vacuum energy, with no matter or radiation. It consists of a period that lasted from 10^{-36} to 10^{-34} seconds of exponential expansion, when the Universe grew by a factor of 10^{43} (Liddle 2003). During inflation the energy density of the Universe was dominated by vacuum energy that was later converted into the kinetic energy of matter and radiation that fills the Universe today. After this, the Universe heated up again and the standard Big Bang process began. An inflation phase before the Big Bang started would make the Universe flat, which solves the flatness problem. It also explains the horizon problem. In an inflationary phase, the expansion of space is accelerated by vacuum pressure, and light can travel effectively faster than it would in a spacetime filled with matter. Thus, by the end of the inflationary period, light could have connected the whole Universe.

1.2 Galaxies in the Λ-CDM framework

The current standard model of Big Bang cosmology is known as the Λ-cold dark matter (Λ-CDM) model, which represents a universe with cold dark matter (CDM) and a parameter Λ known as the cosmological constant, associated with dark energy and responsible for the acceleration of the Universe. According to this model the Universe is made up roughly of 71% dark energy, 24% dark matter and 4% baryonic matter (Ade *et al.* 2016).

The existence of dark matter was first proposed by Zwicky (Zwicky 1933). His studies of galaxy velocities in clusters suggested that there should be more mass present in clusters than could be accounted for by the visible mass of the galaxies. The existence of this additional mass was necessary in order to provide sufficient gravitational pull to keep the clusters from flying apart. Since then, many other studies have corroborated the existence of dark matter, including measurements of rotational curves for spiral galaxies (Oort 1940; Rubin, Thonnard & Ford 1978), or the mass inferred from X- ray temperature observations of elliptical galaxies, or clusters. CDM is a hypothetical form of dark matter that would be composed of the so called Weak Interacting Massive Particles (WIMPs). The most likely WIMP candidates are the neutralinos, which are the lightest stable particle in supersymetric theories. The main characteristic of CMD is that its particles move

slowly, at non-relativistic velocities, which makes the large-scale structure of the Universe grow in a bottom-up manner (Peebles 1982; Fantin, Merrifield & Green 2008).

When the CMB was created, superposed upon the smooth background were small fluctuations on density of matter. The constant amplifications of the initially small fluctuations gave rise to the large size structures we observe in the Universe. Regions which were slightly overdense compared to their surroundings had larger than average gravitational potential and so accreted matter (mostly dark matter as it is far more abundant than baryonic matter) from their surroundings, becoming in the process more overdense. Therefore, dark matter halos form first from hierarchical clustering, to create larger halos through subsequent mergers (Lacey & Cole 1993), and dragging with them baryonic matter in the form of gas that stars are made from. When sufficient density of this gas was present, the luminous content of their galaxies formed from the cooling and condensation of gas within the potential wells of these dark matter halos.

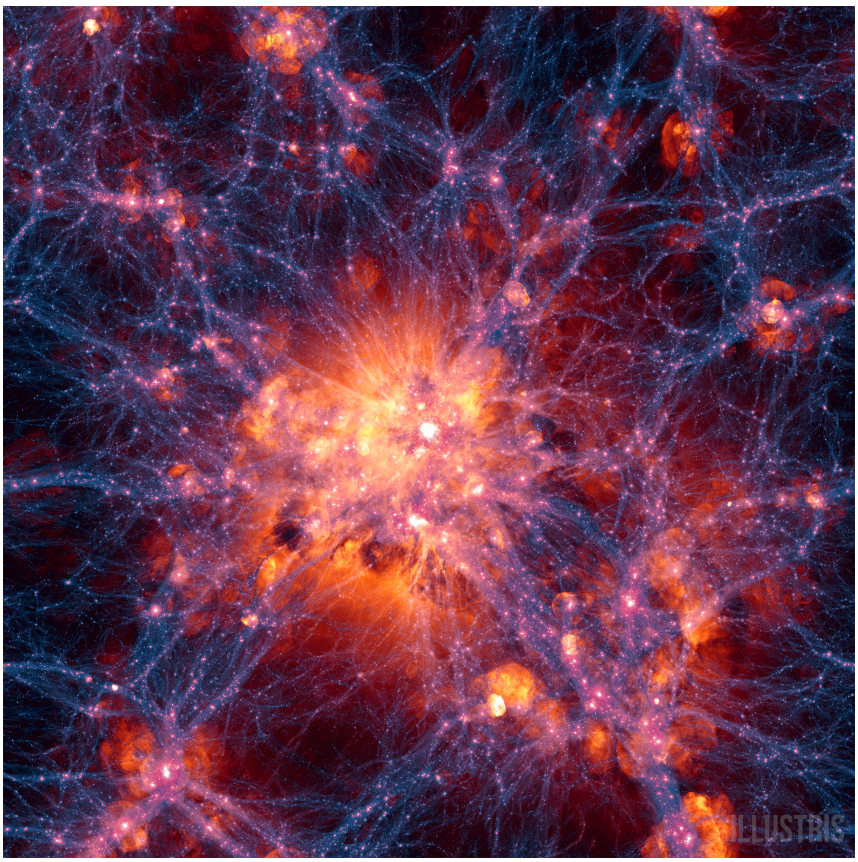


Figure 1.2: Large scale projection through the Illustris volume at $z = 0$, centered on the most massive cluster, covering a depth of 15 Mpc/h. The dark matter density is shown overlaid with the gas velocity field. *http://www.illustris-project.org/media/*.

Numerical N-body simulations, such as the Millennium simulation (Springel *et al.* 2005), have explored hierarchical formation in great detail, and allow us to visualize the distribution of matter in the Universe. More recently, hydrodynamical simulations like EAGLE (Schaye *et al.* 2015) and Illustris (Vogelsberger *et al.* 2014) are not only able to trace the dark matter but also the gas through hydrodynamical prescriptions and subgrid physics (the main physical processes include in hydrodynamical simulations are gas cooling, star formation, and stellar and AGN feedback, explained in 1.3). These simulations show a filament-dominated large scale structure (Figure 1.2), and favour the hierarchical assembly of galaxies. They are able to successfully predict many properties of galaxy populations, although there are still some unresolved discrepancies with observations, such as the satellite and the cuspy halo problem.

1.3 Physical processes of galaxy formation

Our current view on galaxy formation is still incomplete. However, thanks to the advance in numerical and hydrodynamical simulations we have now a better understanding of the critical processes of galaxy formation, within the Λ-CDM framework. In the following paragraphs we explain the main processes responsible of galaxy formation that take place in dark matter halos.

Radiative cooling

Cooling plays a crucial role in galaxy formation, as gas needs to cool in order to collapse and form a galaxy. The main cooling mechanism relevant for galaxy formation is radiative cooling, in which gas loses energy through the emission of photons as a consequence of two body interaction, such as collisional excitation (the impact of a free electron positions a bound electron into an excited level and, as it decays, it emits a photon), collisional ionization (the impact of a free electron ionizes a bound electron, taking kinetic energy from the free electron), recombination (a free electron recombines with an ion, and the kinetic energy of the electron is radiated away) and bremsstrahlung emission (a free electron is accelerated by an ion, emitting a photon).

Conservation of angular momentum

Halos acquire angular momentum due to tidal torques from neighbouring overdensities, as they merge, grow and drag gas. The formation of disc galaxies is the result of the conservation of the angular momentum of the gas collapsing in the dark matter halos. Spheroids, on the other hand, can be formed in violent mergers of discs galaxies that are able to change the ordered motions of discs into random motions. Internal, secular processes (e.g. bars) can also lead to the formation of spheroids.

Star-formation

Star formation is a critical process in galaxy formation, as galaxies do not exist without stars. Star formation occurs in giant molecular clouds, which are dense self-gravitating region of the interstellar medium, with temperatures of about 10K. If the mass of the cloud is greater than a critical mass, known as the *Jean mass*, which depends on temperature and density, then the molecular cloud starts collapsing. Due to initial inhomogeneities, denser regions of the cloud fragment and collapse locally. A cloud fragment becomes increasingly denser and hotter, rising its opacity until cooling becomes inefficient and it is opaque to its own radiation. The temperature keeps on increasing and, eventually, the central temperature reaches the hydrogen ignition threshold and the start is born. Starts frequently form in groups, and the distribution of their masses follows and empirical function known as the initial mass function (distribution of initial masses for a population of stars). According to this function the majority of newly formed stars are low mass with fewer high mass stars.

Feedback

There are different processes that can suppress star formation. This can be achieved by removing gas from a galaxy (e.g. ram pressure striping), stooping the gas from accreting into the interstellar medium (e.g. strangulation) or by feedback processes, which heat the gas and thus prevent star formation. Feedback can be produce by stellar winds, in which case, a massive star loses a substantial amount of mass and transfers kinetic energy into the surrounding gas. Supernova explosions can also produce an enormous amount of energy

that heats the gas and prevents further star formation. Another important feedback source is provided by active galactic nuclei (AGN). There are several mechanisms by which AGN can release a large amount of energy and momentum into the gas, suppressing cooling and star formation on the galaxy, such as AGN driven winds originated in the region surrounding the galaxy (kinematic feedback), or highly collimated and powerful AGN jets that ionize the gas (radiative feedback).

1.4 Galaxy classification

After the investigation of 400 extragalactic nebulae, Hubble was the first to propose a morphological classification system of galaxies (Hubble 1926). The Hubble classification scheme can be represented in a diagram, sometimes referred to as the 'tuning fork' diagram (Figure 1.3). This diagram is composed of two sections, the elliptical galaxies and the spirals (a few percentage of galaxies were classified by Hubble as irregulars but he did not include them in the diagram). As seen in Figure 1.3, elliptical galaxies (E) were subdivided according to their ellipticity $\varepsilon = (1 - b/a)$ (a and b denote the semimajor and semiminor axes respectively), from completely round (E0) to higher ellipticities (E7). The spirals were further separated into 'normal' spirals (S) and barred spirals (SB). Each of the latter series was subdivided into three sections, according mostly to the tightness of the spiral arms, and designated by the letters a, b, and c. He also introduced the transition stage of lenticulars (S0/SB0) between ellipticals and spirals.

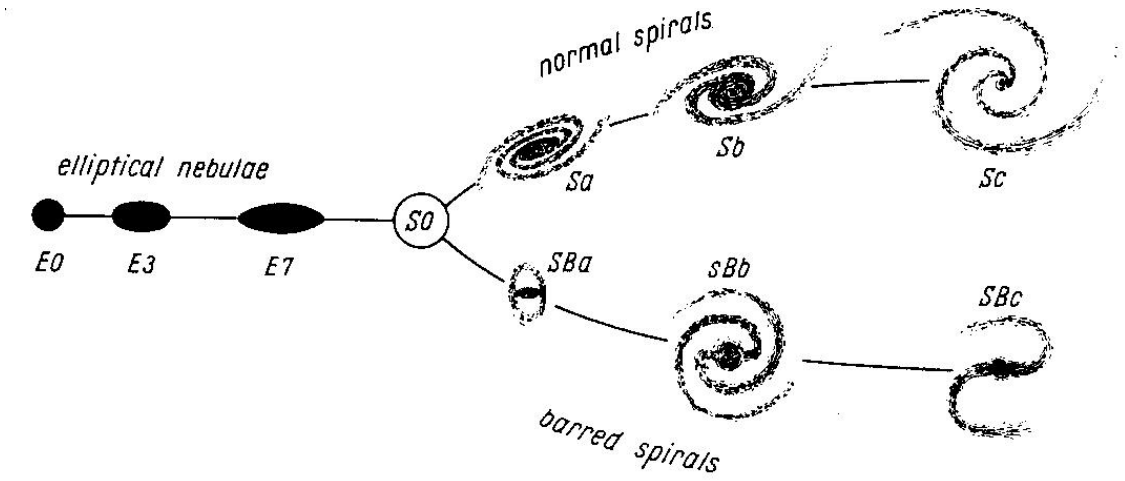


Figure 1.3: Hubble's original tuning-fork diagram from *Realm of the Nebulae* (Hubble 1936).

The Hubble classification is still widely used, as it is able to represent the vast majority of galaxies in the local universe. The main properties of these different types of galaxies are described in the following paragraphs.

Elliptical galaxies They are smooth, round and almost featureless, centrally concentrated systems. They have mostly Population II stars and contain little to no gas or dust. Therefore, they have few young stars, which results in low rates of star formation. They are generally red in colour due to the dominance of older, cooler stars, which suggests that most ellipticals formed long ago, which is why they are also referred as early-type galaxies.

Lenticular galaxies They are a transition type between ellipticals and spirals. They are smooth and featureless galaxies with a prominent rotating disc in addition to the central elliptical bulge. The disc lacks any spiral arms and contains no gas, dust or bright young stars. They consist of mainly old stars, and therefore have little star formation.

Spiral galaxies These galaxies contain a prominent disc composed of Population I stars, gas and dust. They may also have a bulge of Population II stars. The disc contains spiral arms, filaments outlined by clumps of bright hot O and B stars, and the compressed dusty gas out of which these stars form. The spiral arms are sites of ongoing star formation, and are brighter than the surrounding disc because of the young OB stars that inhabit them. These stars give the blue colour to the galaxy/disc. Around $^2/_3$ of spirals also have a central bar composed of stars. They are referred as late-type galaxies.

Peculiar/Irregular galaxies These galaxies do not have a distinctive regular shape and do not fall into any of the regular classes of the Hubble sequence. Stars, gas and dust are spread randomly. They are generally small galaxies and have ongoing star formation in the nearby universe. Some peculiars are ellipticals or spiral galaxies that have been violently distorted by a recent encounter with a neighbour galaxy. Some are very young galaxies that have not yet reached a symmetric state.

1.5 Bimodality of galaxies

1.5.1 Morphology and structure

In the local universe there is a clear bimodality in the distribution of the galaxy's morphologies, as seen in the Hubble diagram, with most of the galaxies classified as disc-dominated or elliptical systems. Visual morphology can be quantified with structural parameters. The most used method for obtaining a parametrization of galaxy morphology is by fitting the surface brightness of the galaxy to some known function, with the Sérsic function being the most famous (Sérsic 1968):

$$\Sigma(R) = \Sigma_e \exp\left\{-\kappa_n\left[\left(\frac{R}{R_e}\right)^{1/n} - 1\right]\right\}, \tag{1.2}$$

where R is the distance from the centre, the parameter R_e is the effective radius, such that half of the total flux is within R_e, and represents a proxy for the size of the galaxy. Σ_e is the surface brightness at the effective radius R_e. The parameter n is the Sérsic index. Finally κ_n is a positive parameter that for a given n, can be determined from the definition of R_e and Σ_e.

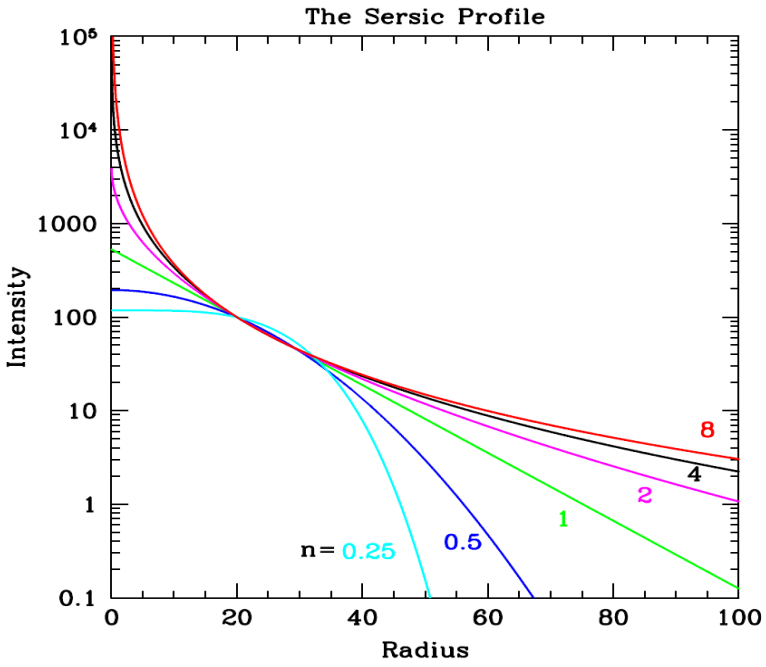


Figure 1.4: The Sérsic profile form given by Equation 1.2, for different values of Sérsic index, n. *http://users.obs.carnegiescience.edu/peng/work/galfit/README.pdf.*

Figure 1.4 shows the Sérsic profile for different values of n. There are two cases of particular interest, when $n = 4$ (de Vaucouleurs profile, de Vaucouleurs 1959) and $n = 1$ (exponential profile), traditionally used to describe respectively the light profile of classical bulges and discs. The Sérsic index parameter determines the shape of the light profile and, on broad terms, the morphology of the galaxy. Therefore, the bimodality observed in morphology is also seen in terms of structural parameters such as Sérsic index. Several studies (e.g., Ravindranath *et al.* 2004; Bell *et al.* 2004; Nair & Abraham 2010; Buitrago *et al.* 2013; Mortlock *et al.* 2013) have shown that galaxies with light profiles best fit with high Sérsic index ($n > 2.5$) are often ellipticals whereas galaxies best fit with low Sérsic index ($n < 2.5$) are often disc type galaxies.

1.5.2 Colour and star formation history

There is also a clear colour bimodality in the galaxy population in the local universe (Strateva *et al.* 2001; Kauffmann *et al.* 2003; Baldry *et al.* 2004; Balogh *et al.* 2004). The left panel of Figure 1.5 shows this bimodality in the g-r colour distribution for SDSS galaxies, with a relatively narrow peak at the red end of the distribution and a broader peak in the blue end. The right panel of Figure 1.5 shows that galaxies populate mainly two distinct regions in the colour-magnitude diagram: the *red sequence* and the *blue cloud*. Galaxies with red colours populate the *red sequence*, in the upper part of the diagram and they follow a tight relation between colour and magnitude. Galaxies with bluer colours have a weaker correlation and populate what is known as the *blue cloud*, in the lower region of the diagram. These two populations of galaxies are not completely separated in the colour-magnitude diagram, and in between both regions a transition zone is found, called the *green valley*.

It has long been established that optical colour is tightly correlated with morphology (de Vaucouleurs 1961), and even more recent studies showing that the colour bimodality is linked to the bimodality observed in morphology (e.g., Strateva *et al.* 2001; Blanton *et al.* 2003; Wolf, Gray & Meisenheimer 2005; Conselice 2006), with the *red sequence* being mainly composed of elliptical/early type galaxies, and the *blue cloud* consisting of late type galaxies or discs.

The optical colours that we measure are obtained from the integrated light of all the stars within a galaxy, and hence reflects the stellar composition of galaxies. Galaxies that

appear blue in optical wavelengths often host O and B stars or other young stars. These are hot and young massive stars with relatively short lives. They are very bright in the blue region of the visible spectrum, and their presence indicates recent or ongoing star formation. In the absence of OB stars, the visible light of galaxies will be dominated by older, redder, lower mass stellar populations, and therefore such galaxies will look red in the optical. Red colour indicates that there has not been star formation activity for some time, or the presence of dust. Hence, the colour in a galaxy is a proxy for the its star formation history. The bimodality observed in the colour distribution and in morphology is therefore linked to a bimodality in star formation activity: disc-dominated galaxies are mostly blue and star forming, while ellipticals or spheroid-dominated systems have redder colours and are passive/quiescent galaxies with no signs of recent star formation activity.

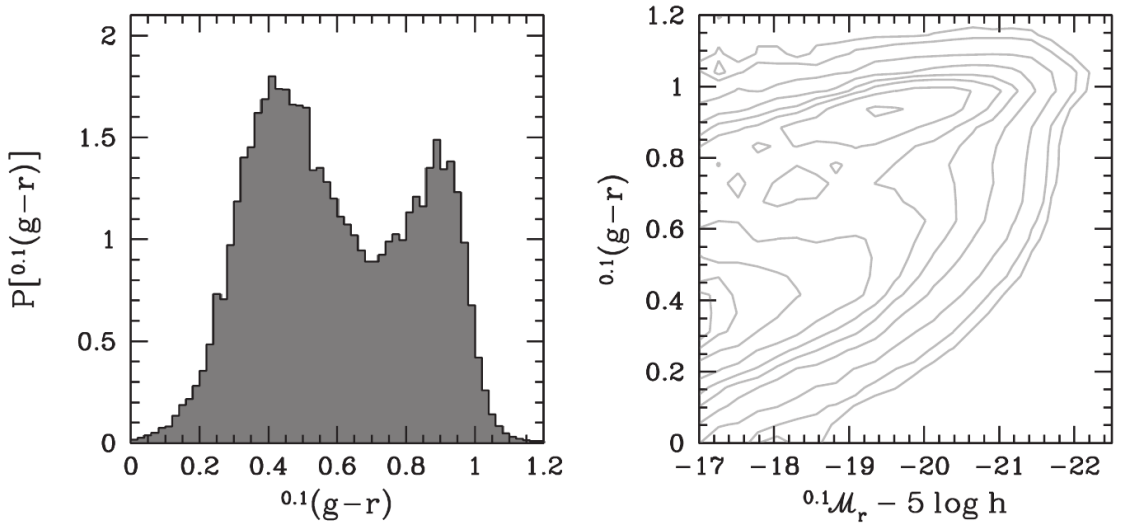


Figure 1.5: The probability density of g-r galaxy colours (left) and the colour-magnitude relation (right) of galaxies in SDSS. The 0.1 present on the axis labels shows that these quantities have been converted to the same rest-frame bands at $z = 1$. Image from Mo, van den Bosch & White (2010).

1.6 High redshift universe and galaxy evolution

Galaxies at high redshift look very different to galaxies in the local Universe. We observe that in the local Universe most massive galaxies are classifiable into Hubble types, i.e. with a well defined structure, such as spheroids or spirals. However, at higher redshift, a population of peculiar galaxies dominates in terms of number densities (e.g., Conselice, Blackburne & Papovich 2005; Mortlock *et al.* 2013). In particular, it is found that the majority of galaxies at $z > 2$ are peculiar with a smaller number of spheroid-like galaxies

(e.g., Mortlock *et al.* 2013; Huertas-Company *et al.* 2016), and with very few traditional disc galaxies. At lower redshifts we find a gradual transition between peculiar and Hubble type galaxies with an approximate 50:50 split between peculiars and Hubble types at $z \sim 1.5$ (Conselice, Blackburne & Papovich 2005; Mortlock *et al.* 2013; Huertas-Company *et al.* 2016).

Thus, during the epoch of $1 < z < 3$ galaxies must have undergone a large amount of evolution which results in morphological transformations. Galaxy structure and morphology are important observables in order to both describe galaxies fully, as well as a critical property for understanding how galaxies form and evolve through cosmic time. One of the traditional ways to characterize the evolution of galaxies is to examine the effective radius and Sérsic index of galaxy populations to determine how these parameters have evolved (e.g., Ferguson *et al.* 2004; Daddi *et al.* 2005; Trujillo *et al.* 2006, 2007; Toft *et al.* 2007; Buitrago *et al.* 2008; van Dokkum *et al.* 2010; Cassata *et al.* 2011). For instance, Buitrago *et al.* (2008) and others studied the size evolution of massive galaxies showing that, while at $z > 1$ these galaxies are extremely compact, in the local Universe we observe that their counterparts are larger, so there must have been a growth in physical size over cosmic time at a given mass. However, this only tells part of the story, as at the same time these galaxies grow in size they also become less peculiar, and develop into bulge+disc systems. This is something that simple Sérsic fitting cannot fully quantify. These findings have been confirmed and expanded upon in great detail by many others since with many explanations for the observed evolution (e.g., Bluck *et al.* 2012; Barro *et al.* 2013; van Dokkum *et al.* 2014; van der Wel *et al.* 2014).

A correlation is also found between stellar mass and galaxy size (mass-size relation), with the more massive galaxies having larger sizes on average, both in the local Universe (Shen *et al.* 2003; Lange *et al.* 2015) and at higher redshifts (van der Wel *et al.* 2014). This suggests that mass growth is accompanied by size growth. There are several physical processes that have been proposed to explain this strong size evolution that also increases the stellar mass, such as gas poor mergers (Khochfar & Silk 2006; Naab, Johansson & Ostriker 2009) and accretion of cold gas along filaments (Dekel *et al.* 2009; Conselice *et al.* 2013). In these scenarios, galaxies grow in size by adding stellar mass to the outer regions.

It appears that the stellar mass of galaxies plays an important role in their evolutionary path. Therefore, an important question in galaxy evolution is how galaxies assemble their stellar mass. Mergers are a common way for a galaxy to build up mass. Another method would be via in-situ star formation. The in-situ star formation is fuelled by hot gas which cools within the galaxy and forms stars, or which has been brought into the galaxy. These two process are known to have increasing importance as we look back in time (e.g., Madau *et al.* 1996; Dekel, Sari & Ceverino 2009; Bridge, Carlberg & Sullivan 2010; Bluck *et al.* 2011), but it is uncertain how each process contributes to the growth of stellar mass over cosmic time.

Star formation activity is another galaxy property linked to stellar mass that evolves with cosmic time (Daddi *et al.* 2007; Noeske *et al.* 2007; Whitaker *et al.* 2012), in such a way that galaxies of equal stellar mass were more highly star forming at earlier cosmic times. This is reflected in the star formation history (SFH) of the Universe. It is widely accepted that the star formation rate (SFR) density in the Universe peaks at $z \sim 2$ and declines thereafter (Lilly *et al.* 1996; Madau, Pozzetti & Dickinson 1998; Hopkins & Beacom 2006; Madau & Dickinson 2014, see also Figure 1.6). Hence, at high redshift, galaxies generally are more star forming.

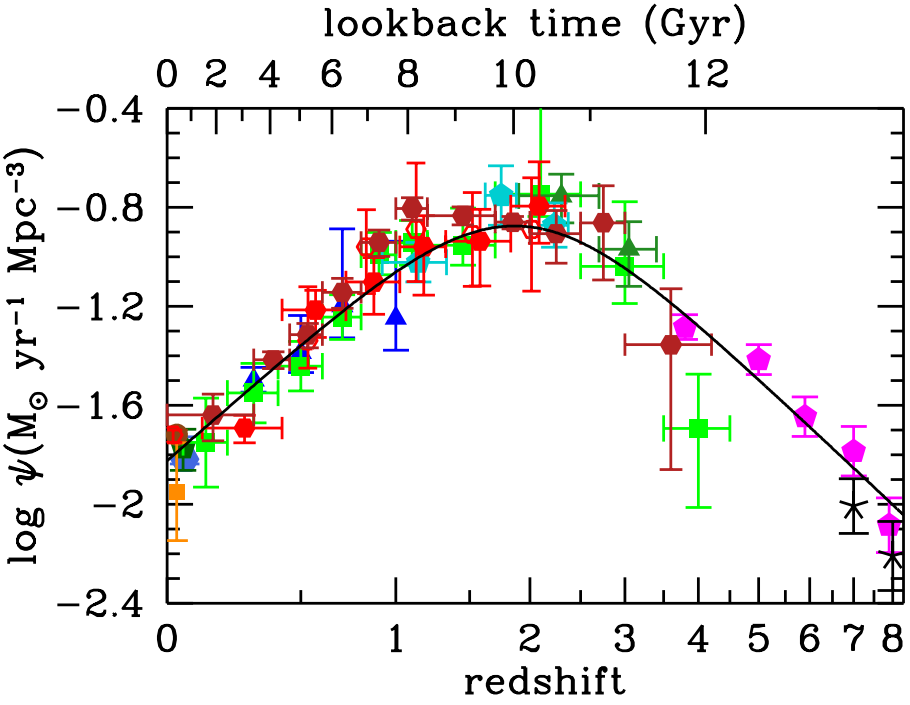


Figure 1.6: Evolution of SFR density with redshift. This Figure, which gathers results from (Madau & Dickinson 2014) and references therein, shows the peak of the SFR of the Universe at $z \sim 2$.

The bimodal distribution in colour observed in the local Universe appears to be already in place by $z = 1 - 2$. But as redshift decreases, the population of passive galaxies increases due to star-forming galaxies shutting down their star formation while, at the same time, they change their morphology. Despite the clear link between morphology and star formation activity, it is not well understood the exact connection between these two processes. Different studies have proposed different mechanisms to explain this connection, such as morphological quenching (Martig *et al.* 2009), in which a galaxy shuts down its star formation activity due to a morphological transformation. Another internal cause linked to galaxy quenching is the presence of an active galactic nuclei (AGN), in which case AGN feedback can heat the surrounding medium and thus prevent the accretion of cold gas (Croton *et al.* 2006; Bluck *et al.* 2011). However, there are other properties that may play an important role in the star formation activity or quenching of a galaxy, such as environment and stellar mass. Galaxies also seem to quench when they reach a characteristic mass (Peng *et al.* 2010; Ilbert *et al.* 2013).

1.7 Bulges and discs

Another paradigm in galaxy formation and evolution is how and when the disc and bulge component form in a galaxy, and in which way their evolution is connected. These two dominant galaxy structures have very different properties. Discs are rotationally supported structures with high gas and dust content, and they show evidence of recent or ongoing star formation. Their surface brightness can be fit by an exponential profile (Freeman 1970). Within the CDM model, they are formed in dark matter halos which have acquired enough angular momentum via torques (Peebles 1969; Fall & Efstathiou 1980) from interacting structures. Bulges are generally divided into two categories: classical bulges and pseudo-bulges. Classical bulges resemble elliptical galaxies and, like them, are supported by the velocity dispersion of stars. They have an older stellar population with not much dust or star-forming regions. Classical bulges are more spherically symmetric and their surface brightness is well fit by a Sérsic profile, generally with $n > 2.5$. They are thought to be formed via mergers or due to disc instabilities which bring gas into the central parts. Pseudo-bulges, on the other hand, are characterized by their more disc-like features (Andredakis & Sanders 1994; Kormendy & Kennicutt 2004) and are more actively star forming. They are rotationally dominated and have shallower surface

brightness ($n \lesssim 2$). They are believed to be the product of secular evolution of the disc, formed from material that moves towards the center due to bars or other nonaxisymmetries (Kormendy & Kennicutt 2004).

It is however still unclear how and when these different components form, and how they are related to each other. To address these problems it is vital to investigate the internal properties of these individual components at high redshift and to trace the evolution of their properties through cosmic time. Thanks to the high-resolution images such as WFC3 *HST*-images it is now possible to separate the surface brightness profiles of high redshift galaxies into their bulge and disc components (e.g., Bruce *et al.* 2012, 2014a,b). These previous works have performed bulge to discs decomposition of massive galaxies at high redshift, and have looked at the properties of bulges and discs separately. They find that bulges gradually emerge in bulge+discs system at $1 < z < 3$, while pure discs are more predominant at $z > 2$. Their findings also favour the formation of bulges as a result of violent discs instabilities. Nonetheless there is still much uncertainty about which component forms first and in which way. This thesis will explore these topics, and address the formation and evolution of bulges and discs separately and how they may be forming in tandem.

1.8 Aim of the thesis and structure

The aim of this thesis is to investigate when the bulges and discs form and how they evolve through cosmic time. We also investigate how structure and morphology are linked to star formation activity, and how stellar mass is assembled into bulge and disc systems. To this end we use the CANDELS/UDS data. The thesis also aims to study the properties of spiral galaxies at high redshift.

In Chapter 2 we perform bulge to disc decomposition on the H-band images of a sample of galaxies with $\log M_* > 10$ and $1 < z < 3$, from the UDS/CANDELS field. We study some of the ways to classify galaxies as either one component systems (i.e. disc-like or spheroid-like galaxies) or two component galaxies (with a bulge and a disc). We explore how the different types of galaxies evolve through cosmic time in terms of number densities, mass densities and size.

In Chapter 3 we continue our study by using a broader range of wavelength. We look where the different types of galaxies and components lie in the UVJ diagram and explore their SFHs as reflected by their rest-frame U-V colours. We compute stellar masses and SFRs for the bulge and disc component separately and explore how they evolve with redshift.

In Chapter 4 we look for spiral structures at high redshift, using the CANDELS Galaxy Zoo classification. We study the properties of these spiral galaxies and compare them with smooth discs that do not show any spiral pattern.

In Chapter 5 we summarise the result from previous Chapters and discuss future work.

Throughout this thesis we use AB magnitude units and assume the following cosmology: $H_0 = 70\ \mathrm{kms}^{-1}\mathrm{Mpc}^{-1}$, $\Omega_\Lambda = 0.7$, and $\Omega_m = 0.3$.

Chapter 2

The evolution of discs and bulges

2.1 Introduction

In the local Universe galaxies have a well defined structure and can be mostly classified into disc-dominated, spheroidal systems, or mixed systems with a spheroidal component surrounded by a disc. On the other hand, at higher redshift ($z > 2$) the majority of galaxies are peculiar (Conselice, Blackburne & Papovich 2005; Mortlock *et al.* 2013; Huertas-Company *et al.* 2016). Thus, during the epoch of $1 < z < 3$ galaxies must have undergone a large amount of evolution resulting in, or produced by, morphological transformations.

To comprehend how galaxies make the transition to become the galaxies we observe in the nearby Universe, it is especially important to study them at high redshift ($z > 1$) when they are undergoing these transformations and, furthermore, to do so in a wavelength which probes the underlying stellar mass of the system. Since one of the major hallmarks of the Hubble sequence is the bulge and disc dichotomy, a natural next step in understanding the evolution of galaxies and their structures is to determine when and how discs and bulges, and especially disc+bulge systems, first formed.

These higher order structural parameters can be obtained by light decomposition, i.e. by fitting galaxy surface brightness profiles to well known functions, such as exponential plus de Vaucouleur light profiles. However, for high redshift galaxies, this is quite a difficult task, as galaxies are not resolved as well as they are in the local Universe. It is

thus critically important to understand the effects of redshift on our measurements of the light decomposition of these galaxies, which we also examine.

Due to the advent of the WFC3 camera on *Hubble*, we can take advantage of high quality and high resolution images of high-z galaxies and, instead of just studying them as a whole, we can perform bulge to disc decomposition with unprecedented accuracy. In fact, there have been studies at high redshift using light decomposition in two dimensions using different codes and methods (e.g., Buitrago *et al.* 2008; van der Wel *et al.* 2012; Bruce *et al.* 2012; Lang *et al.* 2014) with a variety of results suggesting that galaxies indeed become more 'disky' at high redshift, i.e. massive galaxies contain on average lower Sérsic indices at high redshift than at lower redshifts (van der Wel *et al.* 2012). The bulge-disc decomposition allows us to study properties of these two fundamental components separately. In these works galaxies are typically fitted using a combination of a de Vaucouleurs and an exponential profile to describe, respectively, an assumed bulge and a disc component in each galaxy.

Previously, using bulge and disc decompositions, Bruce *et al.* (2012) claim that at low redshift, massive galaxies are bulge-dominated. While at redshifts $1 < z < 2$ galaxies are a mix of bulge+disc systems and by $z > 2$ they are mostly disc-dominated, up to $z = 3$ there are other results showing that stellar mass correlates with the redshift at which Hubble type galaxies start to dominate over peculiar (Mortlock *et al.* 2013). Nevertheless, it remains unclear what causes this transition and when the dominant structures of the local Universe (bulges and discs) appear as well as if these are related events. In this Chapter we investigate the structures of these distant galaxies to determine when, and in what way, discs and spheroids first appear in the massive galaxy population.

We perform one and two component light decompositions using GALFIT (Peng *et al.* 2002) and GALAPAGOS (Barden *et al.* 2012) to a mass selected sample of galaxies at $1 < z < 3$. We fit the observed two-dimensional surface brightness profiles of galaxies with several models, the first one being a single Sérsic profile (with free n and R_e), and the second one a combination of Sérsic profile (again with free n) and an exponential profile. The latter combination describes, respectively, a bulge and a disc. However, it is important to notice that we do not assume that this dichotomy translates directly and simply to high redshift systems, where something more complicated, or a transition phase

are potentially present between peculiar systems and the classic bulge+disc systems we see in today's Universe. By allowing the Sérsic index to vary we are considering more general bulges, in comparison with previous works where bulges are assumed to be the classical bulge described by a Sérsic law with $n = 4$. In this Chapter, we also study a larger sample of galaxies at high redshift than previous works and a wider range in masses. This can lead to a better interpretation of the role that total stellar mass plays in the evolution of bulges and discs.

By fitting the surface brightness to such models, we obtain raw structural parameters for both one and two dimensional fits. Nonetheless, it is important to know whether an individual galaxy is better fit by a two-component profile (bulge+disc) rather than a single Sérsic profile, as in the case for pure spheroid-like galaxies and disc-like galaxies. This is a difficult task and there have been attempts using different methods: Simard *et al.* (2011) use the F-test probability to determine the most appropriate model, while Lang *et al.* (2014) use both the reduced χ^2 of the model fits and the Akaike information criterion (AIC). In this Chapter we study and combine three different methods: visual classification, F-test and a method based on the Residual Flux Fraction, RFF (Hoyos *et al.* 2012), and explore how each method affects the results.

This Chapter is set out as follow: Section 2.2 is devoted to describing the data we use. In Section 2.3 we describe how the structural parameters of the galaxies in our sample are obtained, and explain the different methods used to classify them. In Section 2.4 the main results are gathered, and in Section 2.5 we discuss and summarize the results.

2.2 Data

2.2.1 Imaging

For this work we examine a sample of 1495 galaxies at redshifts $1 < z < 3$ with stellar masses $M_* \geq 10^{10}\mathrm{M}_\odot$ (see Figure 2.1) from the CANDELS UDS field. CANDELS (Grogin *et al.* 2011; Koekemoer *et al.* 2011) is a Multi Cycle Treasury Program which images the distant Universe with both the near-infrared Wide Field Camera 3 (WFC3) and the visible-light Advanced Camera for Surveys (ACS). In total, CANDELS consists of 902 orbits with the *Hubble Space Telescope* (*HST*) and covers 800 arcmin^2. The survey targets five distinct fields (GOODS-N, GOODS-S, EGS, UDS and COSMOS) at two

distinct depths. The deep portion of the survey is referred to as 'CANDELS/Deep', with exposures in GOODS-N and GOODS-S. 'CANDELS/Wide' is the shallow portion and images all five CANDELS fields. We have used the WFC3 data from the UDS which comprises 4×11 tiles and covers an area of 187 arcmin^2 in the $F160$ (H-band) filter. The 5σ point-source depth for this filter is $H = 27.1$ (AB mag).

The CANDELS UDS field is a subset of the larger UDS area which contains data from the *U*-Band CHFT, *B*, *V*, *R*, *i*, *z*-band SXDS data and *J*, *H* and *K*-band data from UKIDSS. This includes $F606W$ and $F814W$ imaging ACS, $H160$, and CANDELS $J125$-band *HST* WFC3 data, *Y* and *Ks* bands taken as part of the HAWK-I UDS and GOODS-S survey (HUGS; VLT large programme ID 186.A-0898, PI: Fontana; Fontana *et al.* 2014). For the CANDELS UDS, the 3.6 and 4.5 μm data are taken as part of the *Spitzer* Extended Deep Survey (SEDS; PI: Fazio; Ashby *et al.* 2013). SEDS is deeper than SpUDS, which is used in the UDS data set, but is only available over a 0.17 deg^2 region. Therefore, SEDS is a more appropriate choice for the smaller CANDELS UDS region. For a detailed discussion of the CANDELS UDS region photometry see Galametz *et al.* (2013).

The raw exposures from WFC3 and ACS cameras are processed and reduced by the CANDELS team and combined to create the final science mosaics (as explained in Koekemoer *et al.* 2011). First, a bad pixel mask is created, and regions containing bad pixels (such as satellites trails) are masked where necessary. This task is followed by a bias subtraction based on the mean value of all the pixels in the 'overscan region' at the edge of the detector at the time of each readout. This region is insensitive to illumination and is used to measure the bias level of the detector (introduced in order to always keep the signal positive). In other cases bias frames are acquired by taking zero second exposures with the camera shutter closed. Images are then corrected for dark current using reference files. CCD detectors produce a residual 'dark' current even in the absence of illumination. This intrinsic charge is generated due to thermal motion and it is, therefore, highly temperature dependent. To measure the dark current a long exposure is taken with the shutter closed. Lastly, CCDs do not have a uniform response, and flatfield exposures are used to correct this pixel-to-pixel sensitivity variation across the CCD. Flatfields are obtained by uniformly illuminating the CCD, either by taking images of the sky under twilight conditions (sky flats) or by taking images of a reflective smooth screen inside the dome of the

telescope illuminated by artificial lights (dome flats). The science images are then divided by the flatfield exposures as the sensitivity variation is a multiplicative effect.

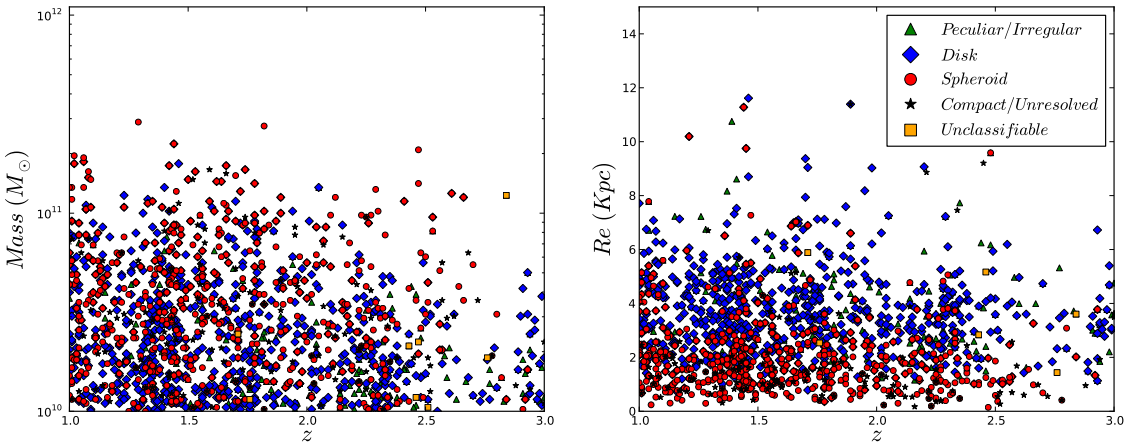


Figure 2.1: The stellar masses (left) and effective radius, R_e, from our 1-component fit (right) vs. redshift for galaxies used in this work. Colours represents the classification from Kartaltepe *et al.* (2015). Green triangles are peculiar or irregular galaxies, blue diamonds are disc galaxies, red circles are spheroids, black stars represent compact or unresolved sources, and yellow squares, unclassifiable objects.

In Figure 2.1 we show how the stellar mass and effective radii of our galaxies are distributed with redshift, along with the morphological classification from Kartaltepe *et al.* (2015), where galaxies are visually classified into five main morphology classes. Such classes are based on the Hubble sequence types: discs, spheroids, irregular/peculiar, compact/unresolved and unclassifiable (more than one of these options can be selected for each galaxy). We divide our sample into star-forming and passive galaxies using the rest-frame UVJ colours (see Mortlock *et al.* 2013), where a galaxy is classified as red/passive if it satisfies the following criteria

$$\begin{cases} (U-V) > 1.3 \\ (V-J) < 1.6 \\ (U-V) > 0.88(V-J) + 0.49 \end{cases} \tag{2.1}$$

and as blue otherwise (see Ownsworth *et al.* 2016 for more details).

2.2.2 Redshifts and stellar masses

We use a combination of photometric and spectroscopic redshifts as described in Mortlock *et al.* (2015) and Hartley *et al.* (2013). The photometric redshifts and stellar masses we

use are described in Mortlock *et al.* (2013). The photometric redshifts were computed by fitting template SEDs to the photometric data points described in the previous Section using the EAZY code (Brammer, van Dokkum & Coppi 2008). The apparent K-band magnitude is included as a prior. The photometry was fit to the linear combinations of the six default EAZY templates, and an additional template which is the bluest EAZY template with a small amount of Small Magellanic Cloud-like extinction added ($A_V = 0.1$). The redshifts are retrieved from a maximum likelihood analysis. For full details of the fitting procedure and resulting photometric redshifts see Hartley *et al.* (2013) and Mortlock *et al.* (2015).

A comparison of the photometric redshifts used in this work to spectroscopic redshifts which are available in the UDS was carried out in Mortlock *et al.* (2015) where it is shown the spectroscopic redshifts versus the photometric redshifts for the 285 CANDELS galaxies with spectroscopic redshifts (see also Galametz *et al.* 2013, for details). The dispersion of $z_{\rm photo.}$ vs. $z_{\rm spec.}$ is $\delta z/(1+z) = 0.026$ for the photometric redshifts, after removing the 2% of catastrophic outliers. However, note that we have only a small sample of spectroscopic redshifts to compare to within the CANDELS UDS region.

Stellar masses are obtained by fitting the $u'BVRi'z'JHK$ bands and IRAC channel 1 and channel 2 to a large grid of synthetic SEDs created from the stellar population of Bruzual & Charlot (2003), using a Chabrier Initial Mass Function (IMF) (Chabrier 2003). Dust is included in the templates using the reddening law of Calzetti *et al.* (2000). The SFH is characterized by an exponential declining law with several ages, metallicities and dust extinctions. The models are parametrized by an age since the onset of star formation, and by an e-folding time such that

$$SFR(t) \propto SFR_0\, e^{-t/\tau}, \tag{2.2}$$

where the values of τ ranges between 0.01 to 10.0 Gyr. Age ranges from 0.001 to 13.7 Gyr (templates that are older than the age of the Universe at the redshift of the galaxy being fit are excluded). The metallicity fraction Z/H range from 0.0001 to 0.05. The dust content is parametrized, following Charlot & Fall (2000) by τ_ν, the effective V-band optical depth, with values $\tau_\nu = 0,\ 0.4,\ 0.8,\ 1.0,\ 1.33,\ 1.66.\ 2,\ 2.5,\ 5.0$. As the UDS sample is complete down to $10^{9.5} M_\odot$ at $2.5 < z < 3$ (see Mortlock *et al.* 2015), therefore, our sample of massive galaxies is mass complete. We use as a PSF the combination of

the TinyTim simulated PSF and a stacked star empirical PSF. The reason for using this PSF is that the TinyTim $PSFs$ are better in the core region (where empirical $PSFs$ tend to broaden), while empirical $PSFs$ appear to fit real stars better in the wings.

2.3 Method

We have used GALFIT and GALAPAGOS to perform our morphological analysis on our sample. GALFIT is a two-dimensional fitting code used to model the surface-brightness of an object with predefined functions. This program allows the user to fit any number of components and different light profiles (e.g., Sérsic, Exponential disc, Gaussian, Moffat, Nuker, etc.) The most used and useful functions to describe galaxies are the Exponential disc profile and the Sérsic profile (Sérsic 1968) for fitting, respectively, disc and bulges/spheroids.

The Sérsic profile has the following functional form given by,

$$\Sigma(R) = \Sigma_e \exp\left\{-\kappa_n\left[\left(\frac{R}{R_e}\right)^{1/n} - 1\right]\right\}, \tag{2.3}$$

where the parameter R_e is the effective radius, such that half of the total flux is within R_e. Σ_e is the surface brightness at the effective radius R_e. The parameter n is the Sérsic index, and it determines the shape of the light profile. Finally κ_n is a positive parameter that for a given n, can be determined from the definition of R_e and Σ_e. It satisfies the equation $\Gamma(2n) = 2\gamma(2n, \kappa_n)$, a non-linear equation which can be solved numerically, where Γ is the gamma function and γ is the incomplete gamma function (see Graham & Driver 2005). The classic de Vaucouleurs profile that describes spheroids and massive galaxy bulges is a special case of the Sérsic profile with $n = 4$ and $\kappa_4 = 7.67$. The Exponential disc profile is also a special case of the Sérsic function when $n = 1$ and $\kappa_1 = 1.68$. The best fit model is obtained by χ^2-minimisation using a Levenberg-Marquardt algorithm in GALFIT.

We carry out our fitting with GALAPAGOS and GALFIT. GALAPAGOS is a software that uses SExtractor (Bertin & Arnouts 1996) to detect and extract sources and performs an automated Sérsic profile fit using GALFIT. It is divided into four main stages: the first one detects sources by running SExtractor, the second one cuts out postage stamps for all detected objects, the third block estimates the sky background, prepares and runs GALFIT,

and the last stage compiles a catalogue of all galaxies. We then fit all of our sample galaxies with both 1 and 2 dimensional profiles.

2.3.1 One component model

We run GALAPAGOS on all of our H-band galaxy images to fit our sample galaxies with a single Sérsic profile, with n as a free parameter as in equation (2.3). GALAPAGOS creates a mask for each individual postage stamp and decides whether a neighbouring object is masked or fit simultaneously, taking into account the distance and relative brightness to the main object. It also calculates the sky value to be used in the fit. As a result we obtain, for all sources, the following parameters: position of the galaxy within the stamp (x, y), effective radius R_e, Sérsic index n, AB-magnitude m, axis ratio q and position angle PA. We discard any fitting with unphysical parameters: effective radius smaller than 0.5 pixels, or larger than the size of the image stamp, $q < 0.1$, and $n < 0.5$ or $n > 8$ ($\sim 7\%$ of the objects).

2.3.2 Two component model

After the previous procedure, we then run GALFIT on the same postage stamps and use the sky value obtained by GALAPAGOS in Section 2.3.1 for the single component fit. We fit the surface brightness of the main galaxy to a Sérsic (free n) plus an exponential profile (Sérsic profile with n fixed to $n = 1$), where the total light distribution (Σ) is the sum of these two models:

$$\Sigma(R) = \Sigma_e \exp\left\{-\kappa_n\left[\left(\frac{R}{R_e}\right)^{\frac{1}{n}} - 1\right]\right\} + \Sigma_e \exp\left[-1.68\left(\frac{R}{R_e} - 1\right)\right], \qquad (2.4)$$

fitting simultaneously or masking neighbour objects in the same way GALAPAGOS does for the one component model. We constrain the centre of both components to be the same. The result is a list of structural parameters for all the sample galaxies: position in the stamp (x, y), effective radius of bulge and disc components $(R_{e\,\mathrm{B}}, R_{e\,\mathrm{D}})$, Sérsic index of the bulge n_{B}, AB-magnitude for bulge and disc $(m_{\mathrm{B}}, m_{\mathrm{D}})$, axis ratio of bulge and disc $(q_{\mathrm{B}}, q_{\mathrm{D}})$ and position angle of both components $(PA_{\mathrm{B}}, PA_{\mathrm{D}})$. As in the previous model, we exclude any fitting with unphysical parameters in any component for the effective radius, axial ratio or Sérsic index $(R_{e\,\mathrm{B}}, R_{e\,\mathrm{D}}, q_{\mathrm{B}}, q_{\mathrm{D}}, n_{\mathrm{B}})$.

Adding an extra component increases the degrees of freedom, hence it is more likely that the fitting gets trapped in a local minimum of χ^2 in the minimisation process. To ensure that the χ^2 obtained from the fitting is the global minimum, we have run GALFIT starting with different initial values of magnitudes, effective radius and Sérsic index. For the Sérsic index, we choose alternatively as initial values $n = 1, 2.5, 4$. The starting values of the magnitudes of each components are: both equal to a magnitude that corresponds to half of the total flux obtained from the one component model, one magnitude which correspond to 80% of the total flux while the other is 20% and vice versa. The starting values for the effective radius are: both equal to the effective radius obtained from the one component model, one of the components half the size of that radius while the other is 20 times larger, and vice versa. We therefore run GALFIT for the $3^3 = 27$ possibilities. We choose the model that delivers the smallest χ^2 and does not have any unphysical parameters.

We first try to fit all the central components of our galaxies with a free n for the Sérsic profile (first term of eq. 2.4), but in some cases ($\sim 40\%$) the fitting results in an unrealistic Sérsic index (either too small or too big). In such cases, we redo the fitting with the Sérsic index fixed first at $n = 4$ and then at $n = 1$ in eq. 2.4, and choose the fitting with the smallest χ^2. In $\sim 73\%$ of these cases, the model prefers $n = 1$. There are still some objects ($\sim 20\%$) that do not have any realistic result with two components, those will be directly classified as 1-component galaxies (if the fitting in this case is considered good) in all methods. In the end, only about $\sim 8\%$ of the galaxies are not well represented with either the one or the two component model. These galaxies are either very compact objects, or considerably faint/small, and have an average redshift of $z = 2$.

We later discuss in Section 2.4.4 how the ratio of the fluxes in the two components changes with redshift. Overall we find that there is a fairly broad distribution of the ratio between the fluxes of the two components. Only about 6% of the galaxies have a second component which is less than 10% of the total flux. Otherwise, 70% of the sample of 2-component galaxies are disc-dominated, with $B/T < 0.5$.

2.3.3 Morphological K-correction

We also investigate whether we should consider the effect of the morphological K-correction in our study, as the quantitative structure of galaxies changes as a function of wave-

length (e.g., Taylor-Mager *et al.* 2007). Using the H-band in the range $1 < z < 3$ means that we are observing and comparing galaxies at a rest-frame wavelength from visible to near-IR (Conselice *et al.* 2011). Therefore, the difference in rest-frame wavelength is smaller than 350 nm at the highest and lowest redshifts. To test whether this difference can have an effect on the structure and morphology of our galaxies, we select a subsample with $z \sim 1$ and fit their surface brightness to a single Sérsic profile in the J-band. The observed rest-frame in this case is $\sim$ 600 nm and by comparing with the same galaxies in the H-band, we see the effect caused by a difference in rest-frame wavelength of $\sim$ 200 nm which is in a similar range to that of our whole sample of galaxies. In the right panel of Figure 2.2 we see that we recover the same Sérsic index whether we use the J- or H-band, although we observe a large scatter particularly for high values of the Sérsic index. This is expected if we notice that, for $n \gtrsim 4$, an increase in Sérsic index does not significantly change the intensity profile (see Figure 1.4). In the left panel of Figure 2.2 we observe a small offset between the effective radius obtained from the J- and H-band. The reddest band (H) is more sensitive to the red central bulge while the J-band is more sensitive to the blue disc, which explains the larger values of the effective radius in the J-band. Nonetheless, as the difference in the effective radius obtained from both bands is small and the Sérsic index is well recovered, we think that the spanning in redshift for our sample of galaxies does not affect the observed structure and morphology. Therefore, we can continue our study without having to consider the morphological K-correction.

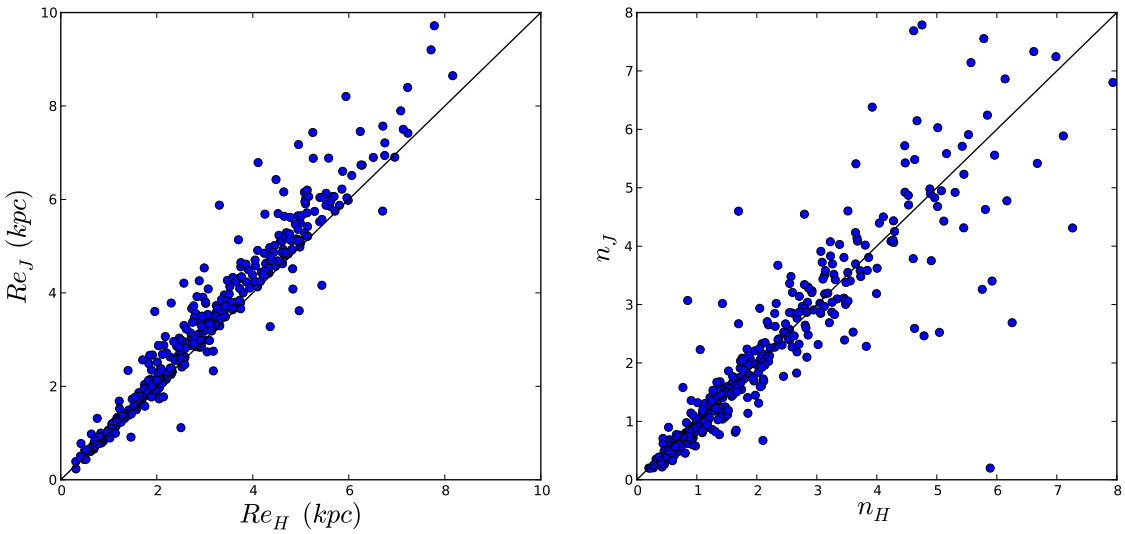


Figure 2.2: Comparison between effective radius (left) and Sérsic index (right) obtained from fitting the surface brightness in the J-band and H-band with a single Sérsic profile at $z = 1$ with a $\Delta\lambda = 200$ nm difference.

2.3.4 Classification

Once we have the two models for each of our galaxy profiles, we need a method to choose whether to use 1 or 2 component fits for each galaxy. This is critical for both determining the evolution of 1-component galaxies, as well as for how multiple component galaxies form and evolve over the epoch $1 < z < 3$. In this work we investigate three different methods of deciding whether a galaxy is better 'fit' as a 1 or 2 component system, and compare the results of these methods to see how internally consistent they are. Our first method consists in visually classifying galaxies into 1- or 2-component systems. Our second method is based on an index called the Residual Flux Fraction (RFF), and the final method is based on a statistical test (F-test). Let us explain them in detail.

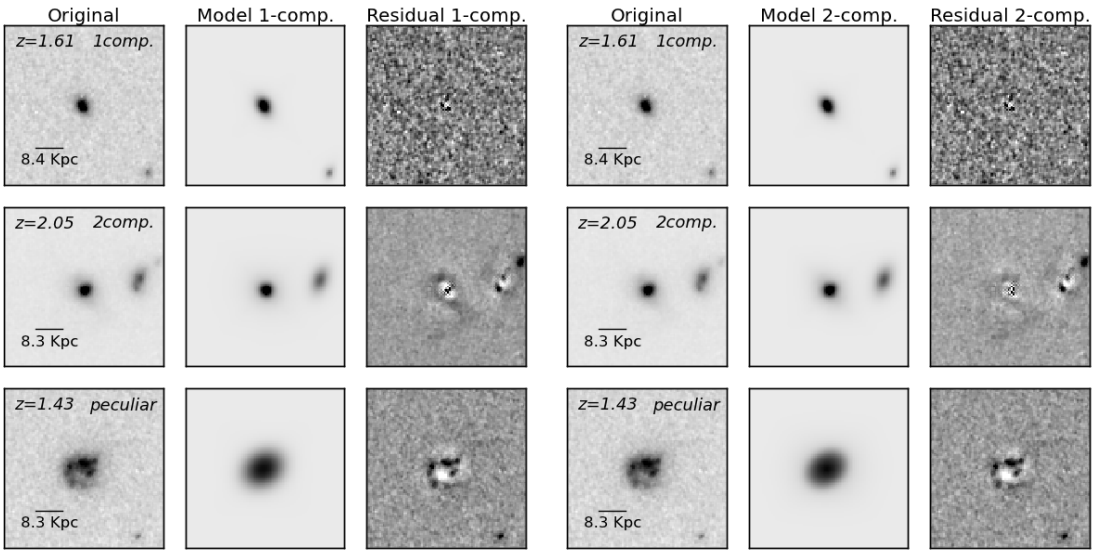
Visual inspection

The first method of determining whether a galaxy has one or two components consists of visually inspecting all the sample galaxies, and their correspondent residual images from both 1 and 2 component best fit models. In Figure 2.3a we show examples of the fitting using one component for three different types of galaxies. For each model we show the original image (left), the model image (middle), and the residual image (right) which is obtained by subtracting the model to the original image. Analogously, in Figure 2.3b we show the fitting using two components.

We have visually classified all the galaxies in our sample into one of three types (examples in Figure 2.4) based on both the visual appearance of the galaxy and also the residuals left over from the galaxy after the best fitting one and 2-component profiles are fit.

One component galaxies. These are disc-like or spheroid-like galaxies, which show no evidence of needing a second component. Indeed, a single Sérsic profile fitting is able to reproduce well the surface brightness of the galaxy as shown by the lack of structures left in the residual image.

Two component galaxies. These are sometimes disc galaxies with a bulge component. They are better fit with a composition of a Sérsic profile plus exponential profile. They show less residual light from the 2-component models than with the single



(a) 1-component model **(b)** 2-component model

Figure 2.3: Visual classification. Left: 1-component model (original image, model and residual). Right: 2-component model (original image, model and residual). Top row: example of 1-component best fit. Middle row: example of 2-component best fit. Bottom row: example of a peculiar galaxy.

one, although a significant amount of residual can be left due to spiral arms in the disc.

Peculiar galaxies. These are disturbed galaxies or mergers. They show residuals from both models, and the addition of another component does not improve the fitting.

There is a very small fraction of galaxies ($\sim 3\%$) that are removed from our sample: unresolved or unclassifiable (due to problems with the image) galaxies. Note that galaxies classified as one or 2-component galaxies can display irregular or merger features, but unlike peculiar galaxies, they are still well represented by either the single Sérsic model or the Sérsic plus exponential model respectively, as these features do not dominate the structure of the galaxy.

Residual Flux Fraction

The Residual Flux Fraction, or RFF (Hoyos *et al.* 2011) is defined as the fraction of the signal contained in the residual image that cannot be explained by fluctuations of the background. Hence, the smaller the RFF value the better the fitting. This index is defined

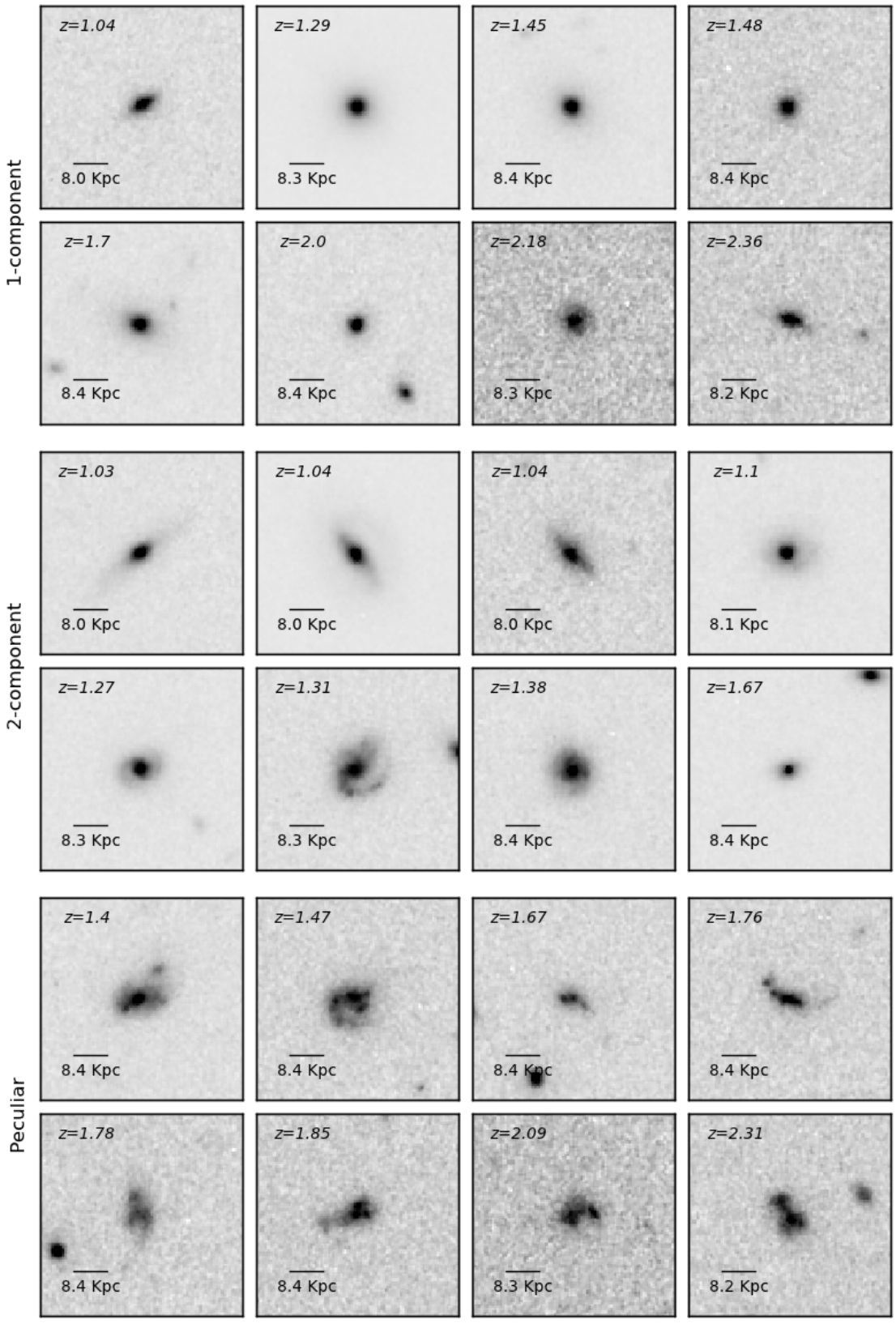


Figure 2.4: Examples of galaxies visually classify as 1-component galaxies (top), 2-component galaxies (middle) and peculiar galaxies (bottom). The postage stamps are 6×6 arcseconds in size.

as follows

$$RFF = \frac{\sum_{(j,k)\in A} |I_{j,k} - I^{\rm GALFIT}_{j,k}| - 0.8 \sum_{(j,k)\in A} \sigma_{B\,j,k}}{FLUX_AUTO}, \tag{2.5}$$

where I is the actual galaxy image, $I^{\rm GALFIT}$ is the model image created by GALFIT, σ_B is the background RMS image and $FLUX_AUTO$ is the total flux of the galaxy calculated by SExtractor. Finally, A represents the area in which we calculate this index. The 0.8 factor in the numerator guarantees that for a Gaussian noise error image, the expected value of the RFF is 0 (see Hoyos *et al.* 2011, for details). It is important to note that the RFF diagnosis does not work well for large areas (Hoyos *et al.* 2011). In those cases, as the galaxy decays towards zero flux at large radius, outer areas will dominate the RFF computation, making it small even when the residual is not good at the centre. Taking this into consideration we have decided to use the area inside the $2.5R_{kron}$ radius of each galaxy to calculate the RFF, where R_{kron} is the Kron radius obtained from SExtractor (e.g., Zhao, Aragón-Salamanca & Conselice 2015).

To calculate the first term of the numerator in equation (2.5), we sum the absolute value of the pixels inside the chosen area from the residual image (original image subtracted by the model). If there is a nearby, but different, object inside this area we do not take into account the pixels corresponding to that object, in order to reduce as much as possible bad fittings from nearby objects affecting the RFF of the main object. To compute the second term of the numerator we assume

$$\sum_{(j,k)\in A} \sigma_{B\,j,k} = N\langle\sigma_B\rangle, \tag{2.6}$$

where $\langle\sigma_B\rangle$ is the mean value of the background sigma for the whole image, and N the number of pixels in the area we are considering in the calculation of the RFF (excluding those pixels belonging to nearby objects). We obtain the value $\langle\sigma_B\rangle$ directly from the sky measures from SExtractor.

We compute the RFF for both the one and two component models (denoted as RFF_1 and RFF_2 respectively) for all the objects in our sample. Peculiar/irregular galaxies and spirals have similar RFF values, namely the average value of RFF for the 1-component model in spirals is $RFF_1 = 0.07$ while for peculiars it is $RFF_1 = 0.08$, making it difficult to distinguish these two populations using just the RFF. To solve this problem we use our visual classification (Section 2.3.4) to separate these two populations.

Spheroid-like galaxies have small RFF_1 ($RFF_1 \lesssim 0.5$) and $RFF_2 \cong RFF_1$, as they are well fit by a single Sérsic profile model. Meanwhile, galaxies that contain a bulge and a disc will generally have a larger RFF_1 ($RFF_1 \gtrsim 0.5$), due to the spiral arms and $RFF_2 < RFF_1$, as the two-component fitting will be better than the single-component model. Therefore they will occupy a different region in the plane of RFF_2 vs. RFF_1 (see Figure 2.5).

We have also used the F-score technique (Hoyos *et al.* 2012) to find the border in the RFF_2 vs. RFF_1 diagram that best separates these two populations (1-component and 2-component galaxies). This method consists in finding the parameters of a function (the border, that in our case will be a second order polynomial) that maximise the F-score, F_β (van Rijsbergen 1979), defined as

$$F_\beta = \frac{1+\beta^2 pr}{\beta^2 p + r}, \tag{2.7}$$

where r and p are the sensitivity or completeness of both populations and are given by the equations

$$r = \frac{\#\{True\ Population_1\}}{\#\{True\ Population_1\} + \#\{False\ Population_2\}} \tag{2.8}$$

$$p = \frac{\#\{True\ Population_2\}}{\#\{True\ Population_2\} + \#\{False\ Population_1\}} \tag{2.9}$$

In these definitions $\#\{True\ Population_1\}$ is the number of objects correctly classified as $Population_1$ by the method while $\#\{False\ Population_1\}$ is the number of those objects of the $Population_2$ misclassified as belonging to $Population_1$. We define analogously $\#\{True\ Population_2\}$ and $\#\{False\ Population_2\}$. Hence r measures the fraction of the actual elements in $Population_1$ correctly classified as $Population_1$. Finally β is a control parameter, specified by the user, that determines the relative importance of r and p. We have chosen $\beta = 1.0$ because having a complete sample of the $Population_1$ is as important as having a complete sample of $Population_2$.

To apply this method to our sample of galaxies we have performed the F-score technique in a training sample. This training sample is formed by the galaxies that have been visually classified most confidently as either 1-component ($Population_1$) or 2-component systems ($Population_2$). This allows us to obtain the (second order polynomial) line that best separates these two populations, from which we can then classify the rest of the galaxies

in our sample according to this criterion. It is interesting to note that in our case, changing the value of β does not significantly change the border line, as both populations of the training sample are clearly separated in the RFF_2 vs. RFF_1 plane. This maximisation has been performed with the Amoeba algorithm (Press *et al.* 1988), using a second order polynomial as the border line. The result of this maximization is shown in Figure 2.5 and can be expressed as

$$RFF_2 = -0.023 + 1.40RFF_1 - 0.94RFF_1^2. \tag{2.10}$$

This line gives the following values for the completeness of the two populations, for the training sample: $r = 0.95$, $p = 0.97$.

As mentioned earlier, once we know this line, we can plot in the RFF_2 vs. RFF_1 plane all our objects (see Figure 2.6) and classify them according to their position with respect to the equation of line (2.10): as 1-component galaxies if they lie above the line or as 2-component galaxies if they are under the line. In Figure 2.6 we plot the entire sample and, just for comparison with the visual classification, we have plotted in blue circles those objects that have been visually classified as 1-component galaxies and in red triangles those classified as 2-component galaxies. There is overall a good agreement between the two methods.

F-test

The F-test is a statistical test in which the statistic has an F-distribution under the null hypothesis. An F-distribution is formed by the ratio of two independent χ^2 variables divided by their respective degrees of freedom.

We have performed the F-test following the method described in Simard *et al.* (2011), who also use it for 1 vs. 2 component separation within SDSS data. In our study we have two models: Sérsic profile (model 1) and a Sérsic+exponential profile (model 2). We consider the χ^2 for each model from the residual image, and take as degrees of freedom the number of resolution elements n_{res} minus the number of free parameters in the model. The number of resolution elements can be calculated as follow

$$n_{\rm res} = \frac{n_{\rm pixels}}{\pi\theta^2}, \tag{2.11}$$

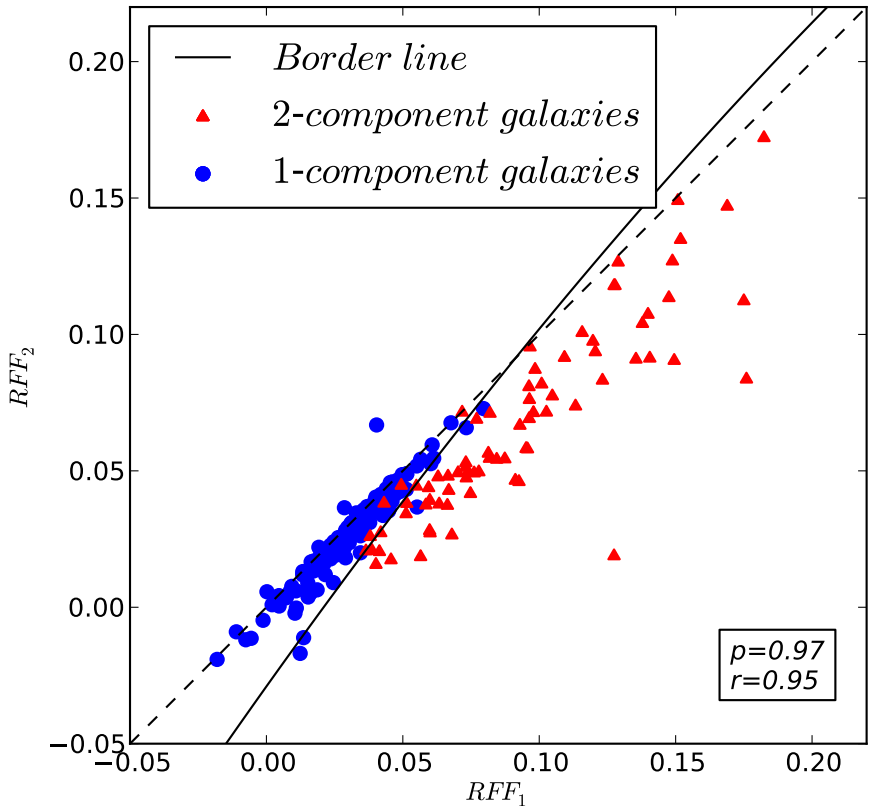


Figure 2.5: F-score technique using RFF measures (see Section 2.3.4 for more details). Using a training sample obtained by visual classification (red triangles: 2-component galaxies, blue circles: 1-component galaxies) we obtain the line (black solid line) that separates these two subsamples given by equation (2.10). p and r are the completeness of the two subsamples. The dash line is the identity function.

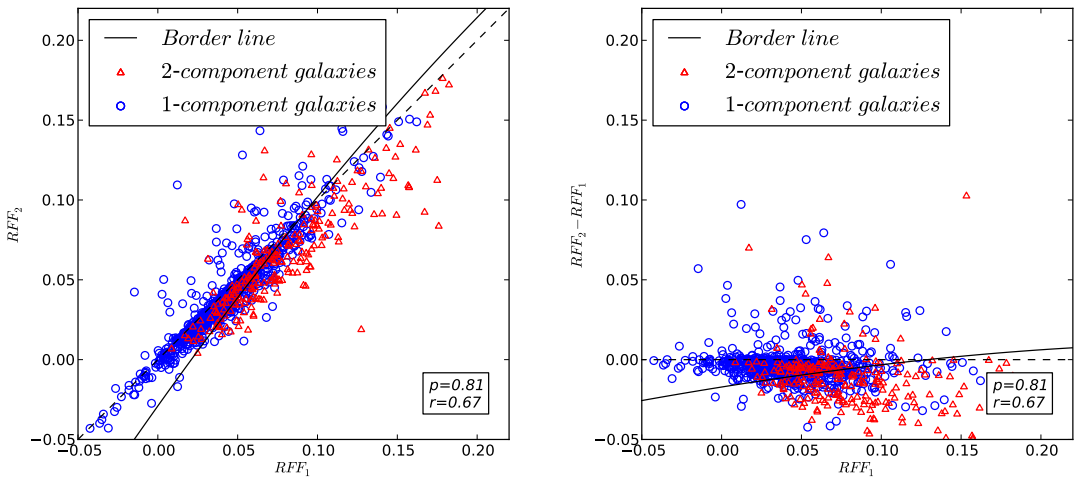


Figure 2.6: RFF_2 (left) and difference in $RFF = RFF_2 - RFF_1$ (right) versus RFF_1, with the classification of all the galaxies using equation (2.10) (black solid line), below which galaxies are considered as having 2 components, and above the line, they are classified as 1-component galaxies. Red triangles are galaxies visually classified as 2-component galaxies and blue circles as 1-component ones.

where $n_{\rm pixels}$ is the number of unmasked object pixels used in the fitting, and $\theta = 1.38$ pix is the H-band seeing half-width half maximum, in units of pixels. As in the RFF calculation, we compute the χ^2 in the area inside the $2.5R_{kron}$ of each galaxy.

To know whether the χ^2 from model 2 is significantly smaller than the χ^2 from model 1, we have to perform a one tailed test. The hypothesis of the test can be formulated as follows

- Null hypothesis H_0: $\chi^2_1 \leq \chi^2_2$ (the simpler model is correct).
- Alternative hypothesis H_1: $\chi^2_1 > \chi^2_2$.

From the statistic of the test $F = \chi^2_{\rm red,2}/\chi^2_{\rm red,1}$ the probability P of accepting the null hypothesis (i.e. the probability that the more complex model is not required) can be calculated. Following Simard *et al.* (2011) we set a 1σ threshold value $P_0 = 0.32$ below which we consider galaxies to be better fit by model 2 (Sérsic+exponential), and therefore, classified as 2-component galaxies. Meanwhile those with $P > P_0$ are classified as 1-component galaxies.

Notice however that with this method, we cannot distinguish peculiars from 1-component galaxies, as in both cases the more complex model is not required. As in the RFF method, we have used the visual classification to separate the peculiar galaxies. Those can also be separated by using the asymmetry index (e.g., Conselice *et al.* 2003), finding similar galaxies (Mortlock *et al.* 2013).

2.4 Results

In this Section we compare how the selection of our galaxy sample into one or two component types varies from one method to another. For our final results, we average the properties for the three methods, to take into account the strengths and weaknesses of each method. These final results include examining the fraction of 1- or 2-component galaxies as a function of redshift and stellar mass, as well as the evolution of the sizes of these components with redshift. In the Appendix A we present simulations to test the robustness of our conclusions.

2.4.1 Method comparison and basic trends

We first explore how the three methods select different galaxies as being 1-component or 2-component systems. We demonstrate this in Figures 2.7 and 2.8 which show the fraction of galaxies selected as 2-component galaxies by each method, as a function of mass and redshift respectively, normalized by the total number of galaxies in each bin. The first thing to take away from these figures is that the agreement between the three methods is good, with the average of the three methods shown as the black stars in both figures.

In more detail, we see that the fraction of 2-component galaxies increases with stellar mass (Figure 2.7) by a factor of ~ 2 from the lowest mass ($19 \pm 5\%$) to the highest mass bin ($43 \pm 6\%$). We explored the possibility that this trend was due to S/N instead of stellar mass, but we observed that regardless of the S/N the trend of 2-component galaxies with stellar mass was preserved, so we believe that this trend is real. This trend is also not a result of redshift effects as we show in the Appendix A.

In a similar way, we see a trend in terms of the fraction of 2-component galaxies within our $M_* > 10^{10}\mathrm{M}_\odot$ sample at $z < 3$ (Figure 2.8). The fraction of 2-component galaxies decreases with higher redshift for all the methods, from $35 \pm 6\%$ at $z \sim 1$ to $8 \pm 6\%$ at $z \sim 3$. This is a significant change over a relatively quick ~ 2 Gyr time-span. However, some of this evolution could be due to redshift effects (see Appendix A), so this must be a tentative conclusion at present.

Another thing to notice is that in terms of the fraction of 2-component galaxies evolving with redshift, the RFF method appears to be roughly constant while the other two methods decline with higher redshift. This is likely due to our galaxies having some residual light even at high redshift. This can arise from having two components at lower redshifts, where indeed the RFF agrees with the F-test and visual methods. However, at higher redshifts, what we are likely seeing is higher RFF values which are due to galaxy formation processes such as residuals from merging or star formation (e.g., Conselice *et al.* 2003; Conselice, Rajgor & Myers 2008; Bluck *et al.* 2012). These signatures would not as easily be seen in the other two methods.

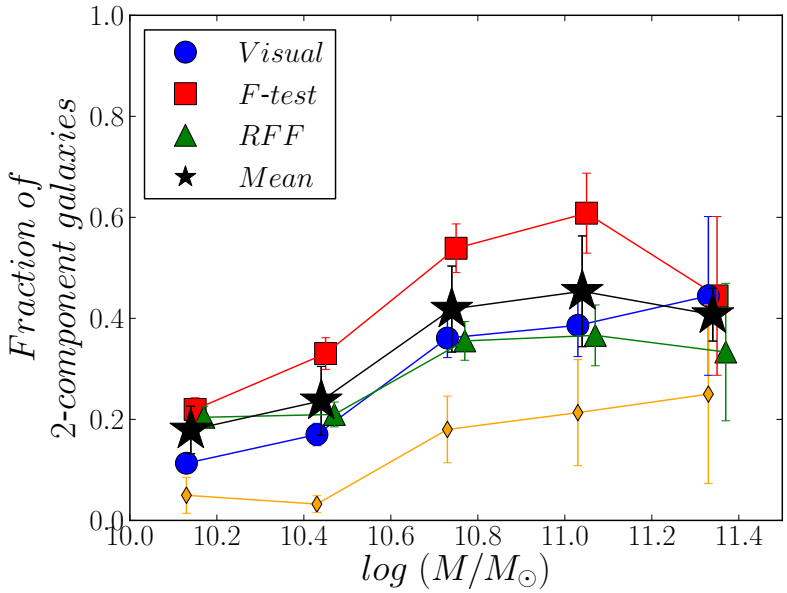


Figure 2.7: Fraction of 2-component galaxies as a function of stellar mass at redshifts $1 < z < 3$, selected by the three selection methods (visual classification: blue circles, F-test: red squares, and RFF method: green triangles) as a function of the stellar mass. The black stars represent the mean fraction in each mass bin. The yellow diamonds are the fraction of 2-component galaxies from the high redshift simulated galaxies (see Appendix A). Error bars represent the random errors.

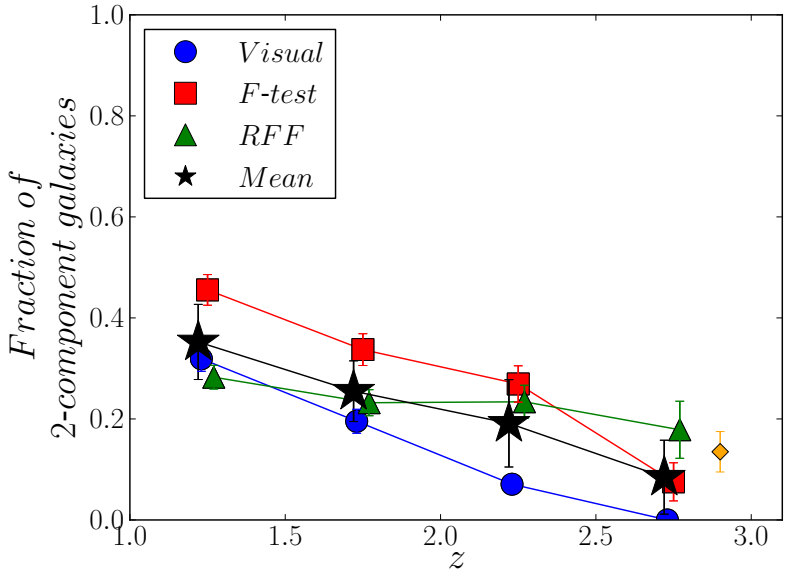


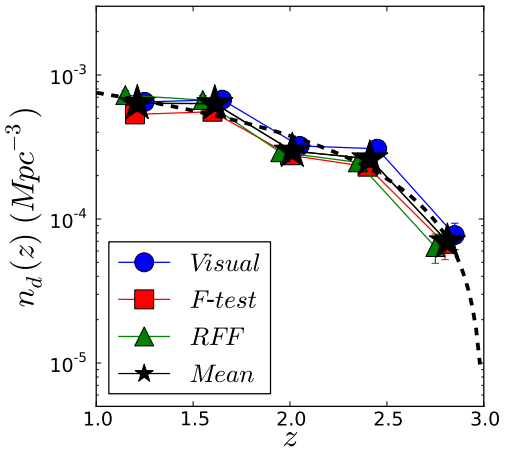
Figure 2.8: Fraction of 2-component galaxies selected by the three selection methods (visual classification: blue circles, F-test: red squares, and RFF method: green triangles) as a function of redshift. The black stars represent the mean fraction in each redshift bin. The yellow diamond is the fraction of 2-component galaxies from the high redshift simulated galaxies (see Appendix A). Error bars represent the random errors.

2.4.2 Number density evolution of galaxy components

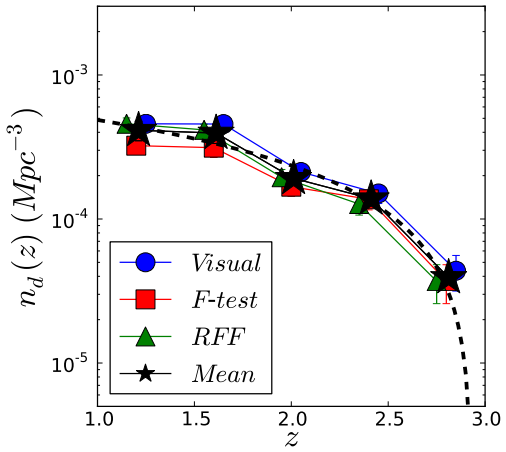
Investigating the number density (number of galaxies normalized by the co-moving volume) of different galaxy selections allows us to determine at which epoch different types of galaxies dominate, and how they evolve throughout the history of the Universe. We

can also compare the rate at which the number density grows between different kind of systems. In this work we explore how the number density of galaxies best fit with either 1 and 2 components evolve in terms of their number densities during the epoch $1 < z < 3$.

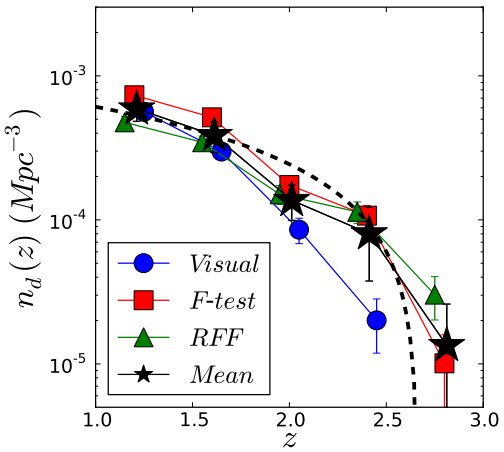
We have split our galaxies into four categories: 1-component discs or disc-like galaxies ($n < 2.5$), 1-component spheroids or spheroid-like galaxies ($n > 2.5$), 2-component galaxies, and peculiar galaxies. In Figure 2.9 we plot the number density of galaxies in five redshift bins for the different types of 1 and 2 component galaxies (number of galaxies normalized by the co-moving volume in Mpc^3 corresponding to that bin). In black we plot the mean number density of the three methods.



(a) 1-component disc-like galaxies.



(b) 1-component spheroid-like galaxies.



(c) 2-component galaxies.

Figure 2.9: Number density $n_{\mathrm{d}}(z)$ as a function of redshift for each type of galaxy (disc-like (a), spheroid-like (b) and 2-component galaxies (c)) for the three selection methods (visual classification, F-test and RFF method). The points are coloured as in Figure 2.7. The dashed black lines are the lines that best fit the mean values (note the log scale).

Function		Disc-like galaxies	Spheroid-like galaxies	2-component galaxies	Total UDS
Linear	$a\ (10^{-4})$	-3.8 ± 0.4	-2.5 ± 0.4	-3.6 ± 0.6	-8 ± 2
	$b\ (10^{-3})$	1.1 ± 0.1	0.7 ± 0.1	1.0 ± 0.1	2.5 ± 0.4
Power-law	α	-2.5 ± 0.3	-2.7 ± 0.3	-4.2 ± 0.8	-2.9 ± 0.8
	$\gamma\ (10^{-3})$	5 ± 1	4 ± 2	20 ± 15	20 ± 17
Exponential	z_0	1.1 ± 0.1	1.0 ± 0.1	0.6 ± 0.1	1.0 ± 0.3
	$n_0\ (10^{-3})$	2.1 ± 0.5	1.5 ± 0.4	4 ± 3	6 ± 4

Table 2.1: Parameters of the fittings to the mean number density of the different types of galaxies and to the total density of UDS.

We fit the mean number density $n_{\rm d}(z)$ of each type of galaxy using three different functions:

$$\text{Linear function} \qquad f_1(z) = az + b, \tag{2.12}$$

$$\text{Power-law function} \qquad f_2(z) = \gamma(1+z)^{\alpha}, \tag{2.13}$$

$$\text{Exponential function} \qquad f_3(z) = n_0 e^{(-z/z_0)}. \tag{2.14}$$

We show in Table 2.1 the result for all three fits, noting that the function that best fits the data is the linear function. To compare the number density of the different types of galaxies, we plot in Figure 2.10 all four number densities, and the total number density of galaxies in the CANDELS-UDS (Mortlock *et al.* 2015). The dashed lines show the best fit of the linear function, equation (2.12).

Already there are several trends which are visible on Figure 2.10. The first is the rise of the 2-component galaxies. While they make up a small fraction of the galaxy population at $z \sim 2.5$, they rise by a factor of 30 in number density to become just as abundant as the 1-component galaxies. This reveals that this epoch of $1 < z < 3$ is when 2-component galaxies form and dominate the abundances of massive galaxies.

We also compare in Figure 2.10 our number densities for the individual galaxy types and the total number density of all galaxies. The total number density of galaxies within the UDS (Mortlock *et al.* 2015) is calculated as:

$$\phi_{\rm Total} = \int_{M_1}^{M_2} \phi(M; \phi^*, M^*, \alpha) {\rm d}M, \tag{2.15}$$

where $M_1 = 10^{10}\mathrm{M}_\odot$ and $M_2 = 10^{12}\mathrm{M}_\odot$. The map $\phi(M)$ is the Schechter function (Schechter 1976) given by

$$\phi(M;\phi^*,M^*,\alpha) = \phi^*\ln 10\left(10^{M-M^*}\right)^{1+\alpha}\exp\left(-10^{M-M^*}\right), \tag{2.16}$$

where ϕ^* is the normalisation of the Schechter function, M^* is the turn over mass in units of dex, α is the faint end slope of the Schechter function and the variable M is the stellar mass in units of dex. The parameters ϕ^*, M^* and α depend on the redshift range, and the values we use to obtain ϕ_{Total} in each redshift bin are calculated in Mortlock *et al.* (2015).

From Figure 2.10 and Table 2.1 we see that the total number density of 1-component disc-like galaxies evolves at a similar rate to that of the 2-component galaxies, but its value is about 1.5 times larger. The number density of spheroid-like galaxies increases slower than those of the other types of galaxies. We observe that for the whole redshift range the number density of disc-like galaxies is the highest of the four types of galaxies. The $z \gtrsim 2$ spheroid-like galaxies have a higher number density than the 2-component galaxies, but at $z \lesssim 2$ the number density of 2-component galaxies become greater than the spheroid-like galaxies.

In Figure 2.11 we compare blue and red galaxies according to the UVJ selection (eq. 2.1) for the four different types of galaxies. Peculiar galaxies are mostly blue at all redshifts, with just a small number of them being red. For disc-like and 2-component galaxies, the fraction of blue galaxies is greater than half. Interestingly, at redshift $z \sim 3$ most of the spheroid-like galaxies are blue, but as redshift decreases, the fraction of red spheroids rapidly increases while blue spheroids decrease. By redshift $z \sim 1$, the vast majority (85%) of spheroid-like galaxies are red.

2.4.3 Total stellar mass density

By investigating the stellar mass density, we can determine which types of galaxies dominates the stellar mass in the Universe at which epoch. This is closely related to the number density evolution, but here we are investigating essentially whether the galaxies in each selection are more massive on average than in the other selections.

In Figure 2.12 we plot the mass density ρ_* of the different types of galaxies as a function of redshift, and in black we plot the mean mass density of the three methods.

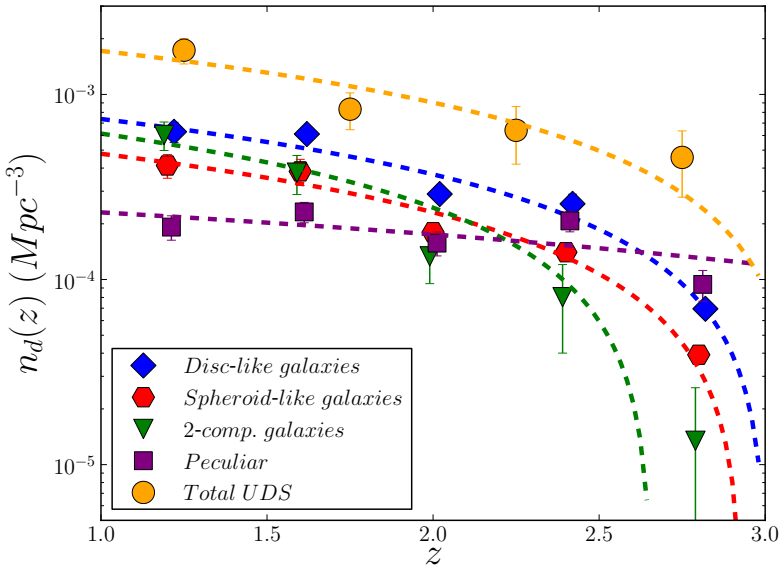


Figure 2.10: Total number density evolution of the different types of galaxies in our sample (disc-like galaxies: blue diamonds, spheroid-like galaxies: red hexagons, 2-component galaxies: green triangles, and peculiar galaxies: purple squares). The yellow circles are the total number density of galaxies in UDS calculated by equation (2.15). The dashed lines are the straight lines that better fit the mean values (in log scale).

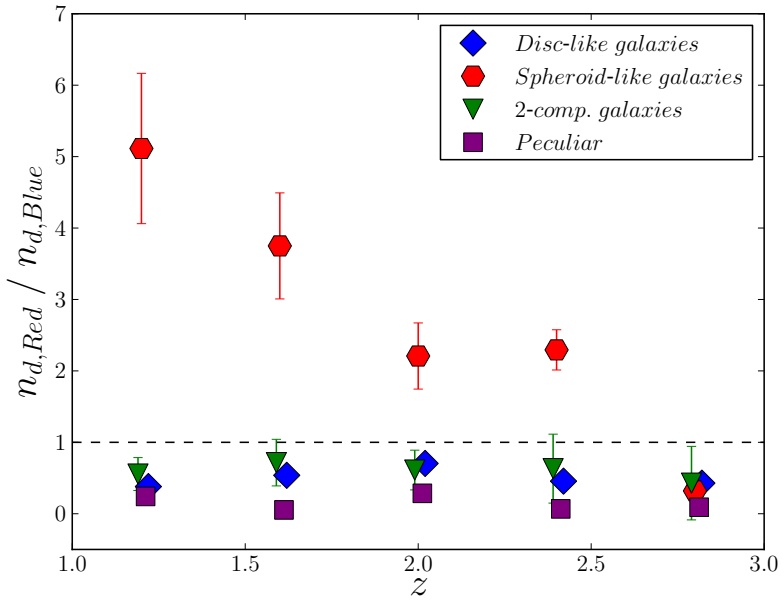


Figure 2.11: Ratio of the number density of red galaxies and blue galaxies for the different types of systems (disc-like galaxies: blue diamonds, spheroids-like galaxies: red hexagons, 2-component galaxies: green triangles, and peculiar galaxies: purple squares).

We fit the mean mass density of each type of galaxy using the same functions as in Section 2.4.2 (linear function, power-law and exponential function). We show the result of the fits in Table 2.2 for all three fits. In Figure 2.13 we plot the mass density for all four classes of galaxies using the average selection, as well as the total mass density from the UDS. The dashed lines show the best fit of the linear function, equation (2.12).

The total mass density of galaxies in the UDS is calculated as

$$\rho_{*,\mathrm{Total}} = \int_{M_1}^{M_2} M_* \phi(M; \phi^*, M^*, \alpha) \mathrm{d}M, \tag{2.17}$$

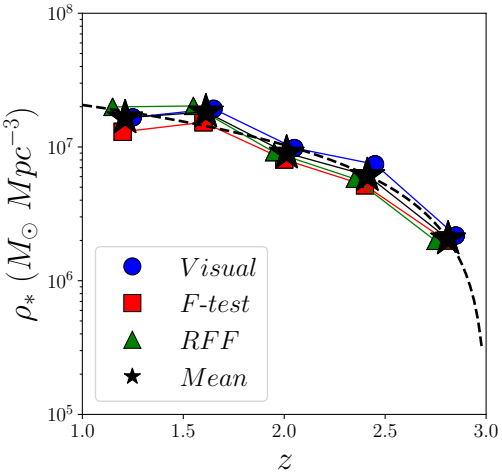
where $M_1 = 10^{10}\mathrm{M}_\odot$, $M_2 = 10^{12}\mathrm{M}_\odot$, and $\phi(M)$ is the Schechter function defined in equation (2.16).

The mass density of the 1-component galaxies evolves at similar rates independently of the Sérsic index selection (i.e. being discs or spheroids). The mass density of 2-component galaxies have the highest increase over the whole redshift range, and its contribution to the total mass density is smaller than that of 1-component galaxies at $z = 1.75 - 3$, but for $z = 1 - 1.75$ the mass density of this type of galaxy becomes dominant. The 2-component galaxies in fact dominate the mass density of massive galaxies at these lower redshifts.

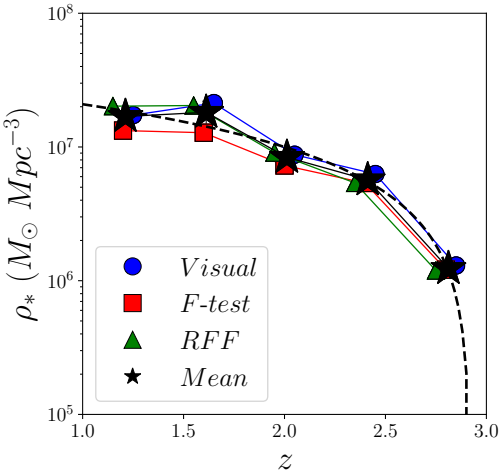
Overall, we find that the mass density for 2-component galaxies increases by a factor of $\sim$ 100, which is roughly a factor of 3 higher than for its number density increase. Therefore, we see a larger effect in the integrated mass density for our galaxies than the increase in the number density. This implies that the galaxies which are driving this increase are more massive at the lower end of the redshift range around $z \sim 1$ than at higher redshifts, relative to the 1- component galaxies. This implies that the most massive galaxies preferentially become the 2-component systems at lower redshifts, while the 1-component systems are relatively lower mass.

Function		Disc-like galaxies	Spheroid-like galaxies	2-component galaxies	Total UDS
Linear	$a\ (10^7)$	-1.0 ± 0.2	-1.1 ± 0.02	-1.8 ± 0.03	-3.6 ± 0.8
	$b\ (10^8)$	0.31 ± 0.04	0.32 ± 0.05	0.48 ± 0.06	1.1 ± 0.2
Power-law	α	-2.5 ± 0.3	-2.7 ± 0.3	-4.2 ± 0.8	-2.9 ± 0.8
	$\gamma\ (10^8)$	1.2 ± 0.5	1.6 ± 0.8	8.1 ± 0.4	11 ± 3
Exponential	z_0	1.1 ± 0.2	1.0 ± 0.1	0.6 ± 0.1	0.8 ± 0.3
	$n_0\ (10^8)$	0.5 ± 0.2	0.7 ± 0.2	2 ± 1	3 ± 1

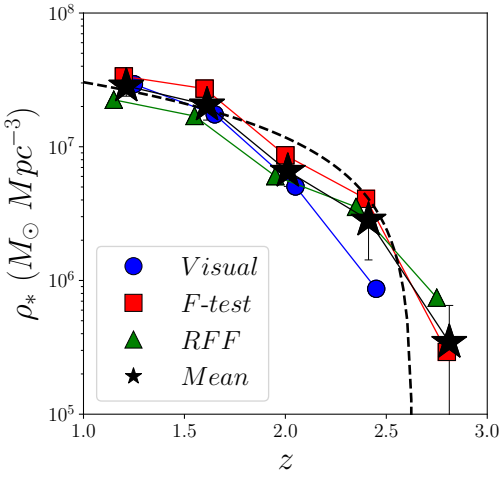
Table 2.2: Parameters of the fittings to the mean mass density of the different types of galaxies and to the total density of UDS.



(a) 1-component disc-like galaxies.



(b) 1-component spheroid-like galaxies.



(c) 2-component galaxies.

Figure 2.12: Mass density as a function of redshift for each type of galaxy in our sample (disc-like (a), spheroid-like (b) and 2-component galaxies (c)) for the three selection methods (visual classification, F-test and RFF method). The points are coloured as in Figure 2.7. The dashed black line are the straight lines that best fit the mean values (black stars) (in log scale).

2.4.4 The size evolution of components

We explore the evolution in size of our galaxy sample, and their components, to determine if the inner and outer components grow together or not. As the effective radius R_e calculated from GALFIT corresponds to the major axis of an ellipse containing half of the light, in order to compare with other results, we have calculated a circularized radius $R_{e,\mathrm{circ}} = R_e\sqrt{b/a}$, where b/a is the axis ratio. In Figure 2.14 we plot the median circularized effective radius of the 1-component galaxies, as well as the discs and bulges of 2-component galaxies, as a function of redshift (for the three different methods as well as the average of the three methods).

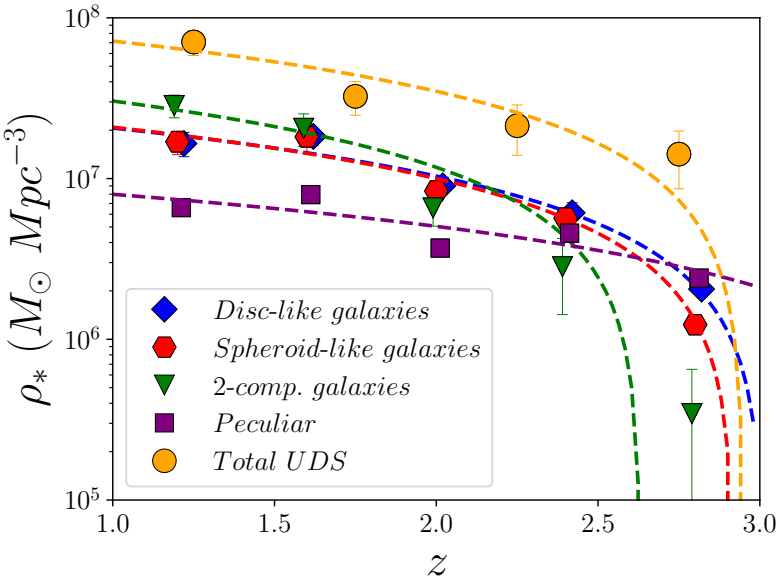
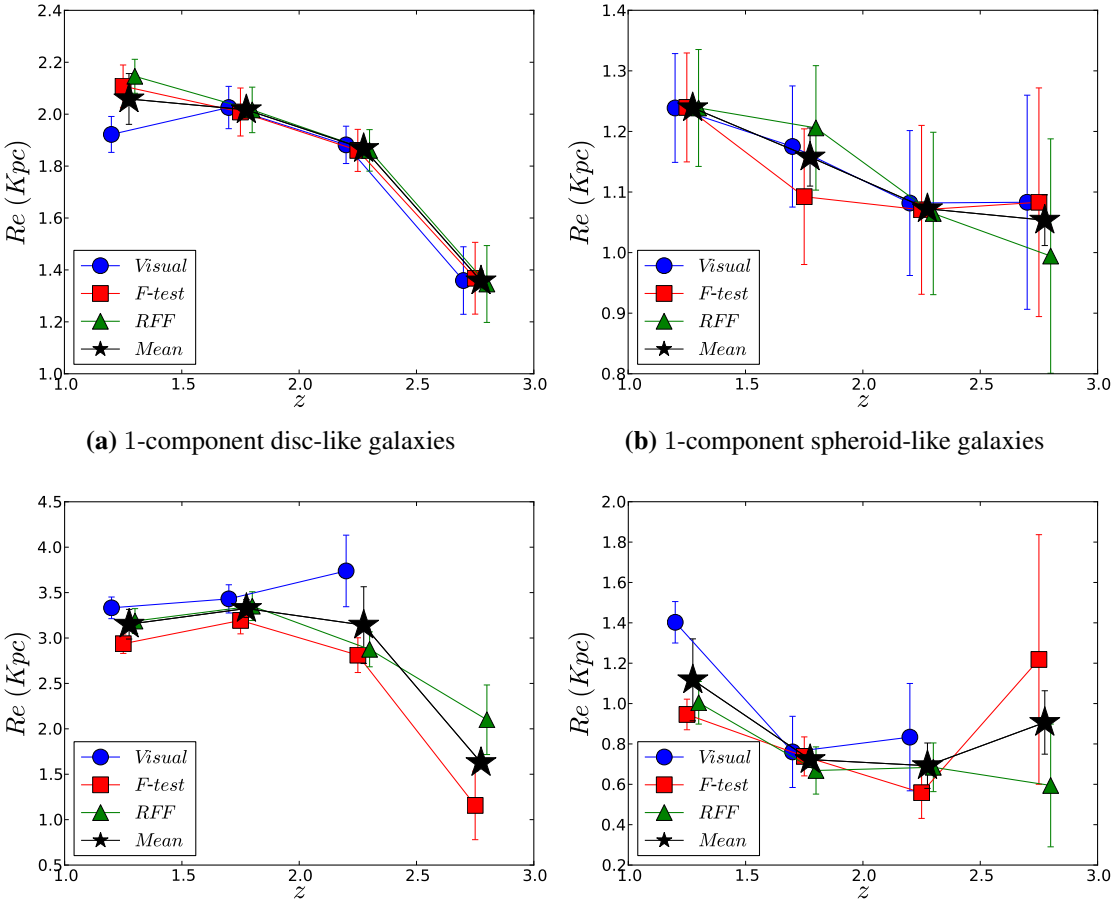


Figure 2.13: Mean mass density evolution of the different types of galaxies (disc-like galaxies: blue diamonds, spheroids-like galaxies: red hexagons, 2-component galaxies: green triangles, and peculiar galaxies: purple squares). The yellow circles are the total mass density of galaxies in UDS calculated by equation (2.17).

First, we observe that there is a trend for the 1-component galaxies: on average they grow in size at lower redshifts, although the evolution appears stronger in disc-like galaxies than in spheroid-like galaxies. Between $1 < z < 3$, the disc-like 1-component galaxies grow on average from 1.3 kpc to 2.1 kpc i.e. an increase of 60%. On the other hand, the 1-component spheroid-like galaxies grow on average from 1.05 kpc to 1.24 kpc i.e. an increase of only 18%. Thus during this epoch the disc-like systems dominate the growth. Note that our simulations of $z = 1$ galaxies to $z = 2.75$ show if anything this increase in size may be more dramatic (see Appendix A). These results also show that the 1-component disc-like galaxies are larger on average than 1-component spheroid-like galaxies.

We find a very interesting trend when we examine the evolution of the inner 'bulge' component and outer 'disc' component of 2-component galaxies. We first note that the discs in 2-component galaxies are larger in size than disc-like galaxies at all redshifts. The discs of the 2-component galaxies increases in size on average from 1.6 kpc to 3.2 kpc i.e. an increase of a factor of 2. On the other hand, we find that the bulge components of the 2-component systems increases very slightly from 0.9 kpc to 1.1 kpc on average.

What we are likely seeing therefore is an inside-out formation of 2-component galaxies such that the inner component is in place before the outer component. This is in agree-



(a) 1-component disc-like galaxies

(b) 1-component spheroid-like galaxies

(c) Discs of 2-component galaxies

(d) Bulges of 2-component galaxies

Figure 2.14: Observed size evolution with redshift. Plotted are the median sizes of galaxies in our sample: disc-like (a), spheroid-like (b), discs of 2-component galaxies (c) and bulges of 2-component galaxies (d) for the three different selection methods (visual classification, F-test and RFF method). The points are coloured as in Figure 2.7. In the y-axis we plot the median sizes of the galaxies. Notice that the visual classification does not select any 2-component galaxies at the highest redshift bin, and therefore, in the bottom plots there is not a blue point at high redshift. The error bars on the points represent the standard deviation.

ment with previous studies such as van Dokkum *et al.* (2010) and Carrasco, Conselice & Trujillo (2010) which study the evolution of massive galaxies since $z \sim 2$ at fixed aperture. Likewise, we find the inner component of our sample does not grow as significantly as the outer component does. This is seen more clearly in Figure 2.15, where we plot the ratio between the mean effective radius of the inner and outer component as a function of redshift. Discs seem to grow earlier, and they increase at a higher rate relative to the growth of the bulges until $z \sim 1.5$, when bulges appear to rapidly grow in size. We only have, however, one point showing this, which will need to be further confirmed. Nevertheless, in Figure 2.16 we observe that the ratio between the flux of these two components remains fairly constant with redshift.

Overall, what we find is that the stellar masses, as traced by the light distribution (assuming a similar mass to light ratio), of these components are increasing at a similar rate, while at the same time the sizes of the outer components are growing faster than their inner components. There are several ways to interpret this. One possibility to explain these observations is through how the additional mass is distributed in the two components. For the outer components, this new mass is added to the outer parts, increasing the size of the disc component, but within the bulges the additional mass is still centrally concentrated. This is one way in which the mass ratio can remain constant while the size ratio increases with time. This is further investigated in Chapter 3.

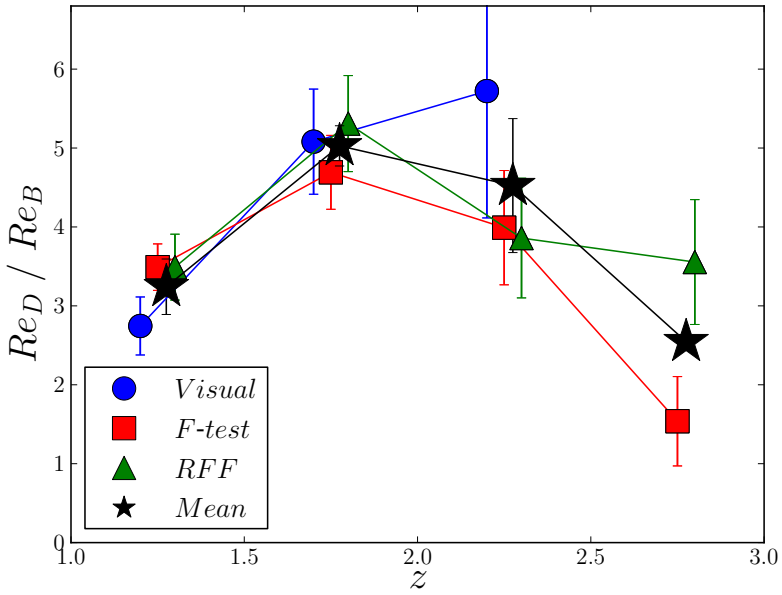


Figure 2.15: Evolution of the ratio between the sizes of discs and bulges of 2-component galaxies. Notice that the visual classification does not select any 2-component galaxies at the highest redshift bin, and therefore, there is not a blue point at high redshift.

It may be argued that the circularized effective radius $R_{e,circ}$ is not the most appropriate quantity to measure the size of discs, as for flat disky objects, $R_{e,circ}$ will depend on the inclination. In which case, the size could be better quantify by the effective radius R_e (major axis of an ellipse containing half of the light). However, we find that using R_e instead of $R_{e,circ}$ for our disky objects does not change our results. In the case of 1-component discs we observe the same growth of 60% over the redshift range, but the sizes are about ~ 1.4 times larger than the circularized radius. For discs of 2-component galaxies, we observe an increase of a factor of 1.7 over the redshift range, which is still

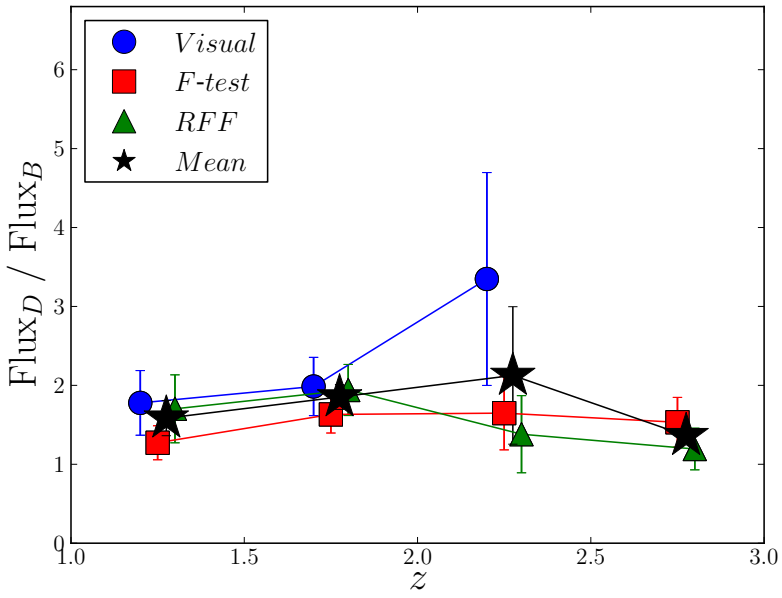


Figure 2.16: Evolution of the ratio between the flux of discs (Flux_D) and bulges (Flux_B) of 2-component galaxies. Notice that the visual classification does not select any 2-component galaxies at the highest redshift bin, and therefore, there is not a blue point at the highest redshift bin.

much stronger than the growth of the bulges at the same redshifts. In this case, the sizes are on average about 1.6 times greater than using the circularized values.

In Figure 2.17 we plot the ratio between the sizes of the galaxy components (disc-like galaxies, spheroid-like galaxies, discs of 2-component galaxies and bulges of 2-component galaxies), and the sizes of galaxies within the nearby Universe at the same mass. These nearby galaxy sizes were obtained by the size–mass relation from GAMA results (Lange *et al.* 2015). We use the early-type relation to compare with spheroid-like galaxies, and the bulges of 2-component galaxies, and the late-type relation for comparison with disc-like galaxies and discs in 2-component galaxies.

- Early type $\quad R_e(\mathrm{kpc}) = c \left(\dfrac{M_*}{\mathrm{M}_\odot} \right)^{\eta}$
- Late type $\quad R_e(\mathrm{kpc}) = d \left(\dfrac{M_*}{\mathrm{M}_\odot} \right)^{\lambda}$

where $c = 36.04 \times 10^{-5}$ kpc, $\eta = 0.38$, $d = 25.26 \times 10^{-3}$ kpc and $\lambda = 0.21$.

We have over-plotted the data from Buitrago *et al.* (2008) (galaxies in the same redshift range as our sample but with higher masses at $M_* > 10^{11}\mathrm{M}_\odot$) calculating the ratios in the same manner. 2-component discs seem to remain the same over redshift while compared with their low redshift counterparts, there may be a slight growth before $z = 2.5$, but

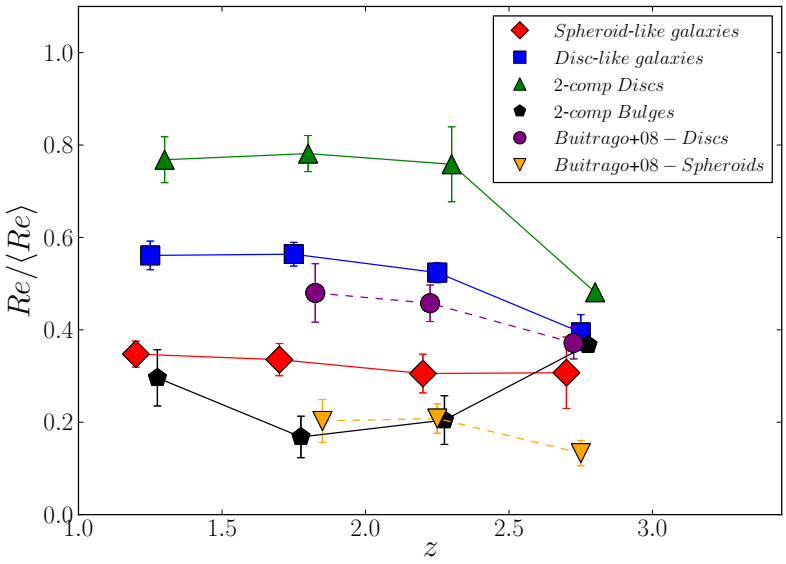


Figure 2.17: Evolution of the ratio between the sizes of the galaxy components (disc-like galaxies, spheroid-like galaxies, disc of 2-component galaxies and bulges of 2-component galaxies), and the sizes of galaxies from the nearby Universe at the same mass $\langle R_e \rangle$.

they remain constant at lower redshifts. Disc-like galaxies are smaller at high redshift compared with disc-like galaxies of the same mass at the present time, in agreement with Buitrago *et al.* (2008). Spheroid-like galaxies also seem to have grown in size over cosmic time, but not as much as disc-like galaxies. The bulges of disc-like galaxies seem to have grown with time, particularly after $z = 2$. We observe that size of spheroid-like galaxies and bulge of 2-component galaxies is less than 40% of that of early-type galaxies in the local universe. This implies a significant growth from $z = 1$ to present day for spheroid dominated galaxies. Disc-like galaxies undergo a less dramatic growth over the same epoch. These results are in agreement with previous studies, such as van der Wel *et al.* (2014), where they observe a growth by a factor of ~ 2 since $z = 1$ for early-type galaxies of similar masses, and only a moderate growth is seen for late-type galaxies.

2.5 Conclusions

We have carried out a detailed investigation of the light decomposition of galaxies within the CANDELS UDS field using 1495 massive galaxies with $M_* > 10^{10}\mathrm{M}_\odot$ at $1 < z < 3$. In this work we set out a new methodology for deciding whether a galaxy should be considered a single or 2-component system using the observed H-band imaging, and then we examined the evolution of the individual component's sizes and mass as a function of redshift and stellar mass.

We have used three different methods to determine if a galaxy is better fit by a 1 or 2 component model for their surface brightness distributions. The three methods are: visual morphology, the F-test, and by examining the residual flux fraction (RFF). We find that all three methods are largely in agreement with each other, and we calculate the mean value of the various parameters we study derived within the 3 methods.

One major result is that the fraction of 2-component galaxies increases with higher stellar mass for all three methods. In fact, on average there are ~ 2 times more galaxies selected as 2-component for the most massive galaxies than in the lowest mass bin. We also find an evolution with redshift, such that the fraction of 2-component systems decreases from about 35% to 8% from $z = 1$ to $z = 3$. However, this decrease with redshift might be partially due to the degraded data at higher redshifts.

We find that disc-like galaxies have the highest relative number density at all redshifts, while spheroid-like galaxies have the lowest increase in that epoch, and by $z \sim 2$, 2-component galaxies exceed both of them in number density. The contribution to the total density due to 2-component galaxies becomes dominant at $z < 1.75$ in spite of their being the lowest at $z > 1.75$. At redshift $z \sim 3$ the majority of spheroid-like galaxies are blue, but as redshift decreases, the number of red spheroid-like galaxies rapidly increases. The other populations of galaxies remain mostly blue for all redshifts.

We also find that for 2-component galaxies there is an increase in the sizes of their outer components, or 'discs' by about a factor of three from $z = 3$ to $z = 1.5$, while the inner components or 'bulges' stays roughly the same size. This suggests that these systems are growing from the inside out, whilst the bulges are in place early in the history of these galaxies. This is also seen to a lesser degree in the growth of single 'disc-like' galaxies vs. 'spheroid-like' galaxies over the same epoch.

We also carry out image simulations to determine how reliable our results are. We do this by reproducing how our galaxies would look at higher redshifts (for more details see Appendix A), we conclude that the decrease in size we observe within discs and bulges for 2-component galaxies in Figure 2.14 must be real, as the simulations show that we can accurately recover the size of the bulges in the simulated redshifted galaxies, including the smallest ones. Discs are also well recovered except for the smallest ones ($Re_{\rm D} < 2\ kpc$), where we recover larger discs than the originals. However, this may

hint that we are indeed observing small discs at the highest redshift bin. The simulations where the F-test is used to find 2-component galaxies may induce us to think that the decrease in the fraction of 2-component galaxies is due to simply redshift. However, the visual classification, which is a reliable tool to distinguish patterns, only accounts for half of the decrease, suggesting that the observed reduction is real (see Figure A.5). It thus seems more reasonable to think that the F-test is not as reliable using the same threshold P_0 for all redshifts. This might be due to the fact that for high redshift, galaxy features are blended with the noise.

Chapter 3

The star formation history of discs and bulges

3.1 Introduction

By $z = 1$, as seen in Chapter 2, the dominant galaxy population is formed by systems that have an inner and an outer component (or bulge and disc) (Bruce *et al.* 2012; Mortlock *et al.* 2013; Margalef-Bentabol *et al.* 2016). However, it is still unclear how and when these different types of galaxies form, and how they are related to each other. There are in fact many different theories for the formation of bulges and discs. For example some models predict that bulges form at high redshift due to disc instabilities and grow via minor mergers (Hopkins *et al.* 2010). Disk formation may also occur due to gas accretion around a bulge which formed early in the history of the universe, either through a rapid collapse or from multiple mergers of galaxies. It is yet to be solved which component forms first, and how these inner and outer components evolve together or separately. To solve these problems it is vital to investigate the internal properties of galaxies which have multiple components at high redshift and to trace the evolution of their properties through cosmic time.

Furthermore, the bi-modality observed in morphology at low redshift in the galaxy population appears to translate to star-formation activity, with discs being blue and star-forming, and bulges/spheroids red and passive (Strateva *et al.* 2001; Kauffmann *et al.* 2003). This bi-modality in morphology and star formation activity is also observed at

higher redshifts (Brammer *et al.* 2009; Whitaker *et al.* 2011), but the separation is less clear, and there is some evidence for a population of blue bulges and red discs (Bamford *et al.* 2009; Conselice *et al.* 2011). Therefore a key question is how morphology and star formation/quenching are related. Several mechanisms have been proposed to explain this, such as morphological quenching (e.g., Martig *et al.* 2009), the presence of an AGN (Croton *et al.* 2006; Bluck *et al.* 2011), or environment effects.

In this Chapter we compare the formation histories of different types of galaxies, as measured through their surface brightness profile shapes. Moreover, for those systems which can be decomposed into two components we examine the evolution of the inner and outer components as a function of redshift. We also explore how the rest-frame $U - V$ colour changes with redshift, and the role of stellar mass in producing evolution within separate components. Finally, we investigate how the star formation activity of both the bulge and the disc evolves with cosmic time, and how this affects the assembly of stellar mass in galaxies.

With the CANDELS data from WFC3 and ACS we are now able to probe the components of galaxies from the ultra-violet to the near-infrared. Studying galaxies and their components at these different wavelengths allows us to probe the properties of bulges and discs separately. We do this by modelling the spectral energy distributions (SEDs) of the bulge and the disc, uniquely and distinctly, after decomposing the galaxy at all the observed wavelengths. From this, we are able to trace the evolution of the stellar populations within these components, as well as measure the contribution to the total stellar mass and SFR from each of the components (Bruce *et al.* 2014a,b).

In addition to evolving in morphology from peculiar to Hubble type systems we know that galaxies become more massive as time passes. There are different ways in which a galaxy can add stellar mass, such as through star formation bursts, or mergers, but it is not clear how the inner and outer components of galaxies grow together. 2-component systems seem to add mass in the outer parts of the galaxy while they grow in size (Margalef-Bentabol *et al.* 2016). However, the detailed evolution of mass within these components is still uncertain, and this is another issue we examine in this Chapter.

The structure of this Chapter is as follow. Section 3.2 is devoted to describe the data we use. In Section 3.3 we describe how we calculate the structural parameters, stellar masses,

rest-frame colours and SFRs. In Section 3.4 the main results of the Chapter are gathered, and in Section 3.5 we discuss and summarize the results.

3.2 Data

3.2.1 Imaging

We examine a sample of galaxies in the CANDELS UDS field. Details about the CANDELS UDS field are explained in Chapter 2. In addition to H band we also use the near-infrared J band, and the visible bands i and V.

3.2.2 Sample of galaxies

We use the same sample of galaxies from Chapter 2. Redshifts and initial stellar masses are computed as described in Mortlock *et al.* (2015) and Hartley *et al.* (2013). That sample is selected from the WFC3 region of UDS, and comprise galaxies at redshifts $1 < z < 3$ and $M_* > 10^{10} M_\odot$. For this work, in addition to near infrared images (H-band and J-band) from the WFC3 camera, we also use the V-band imaging and i-band from the ACS camera. The regions that these two cameras map do not completely overlap, and therefore the final sample for this work (1074 galaxies) only consists of galaxies with both near-infrared and visible-light images.

Galaxies in our sample are classified as either, 1-component, 2-component or peculiar galaxies. The classification is done following the method in Chapter 2, in which different methods (Visual classification, F-test, RFF) to classify galaxies into 1 or 2 components are compared and investigated. As each method has different bias in selecting 2 component galaxies, for this work we classify galaxies as a 2-component objects if at least two methods agree in that classification, and as a 1-component galaxy otherwise. The peculiar population is separated by visual inspection, as done in Mortlock *et al.* (2015). In Figure 3.1 we show our sample of galaxies in the mass and redshift space. 1-component galaxies are further classified according to their Sérsic index, as disc-like galaxies ($n < 2.5$) or spheroid-like galaxies ($n > 2.5$).

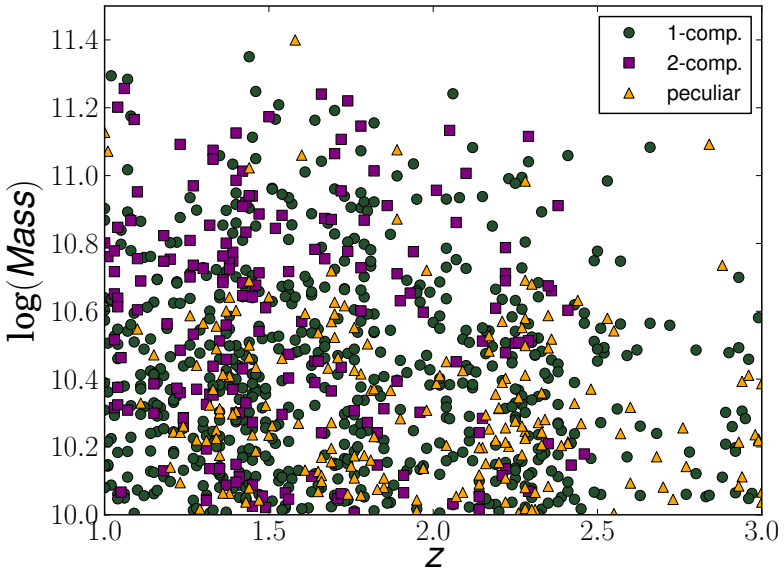


Figure 3.1: The stellar mass distribution with redshift for our initial stellar mass selected sample of galaxies (as calculated in Mortlock *et al.* 2015) versus redshift, for 1-component galaxies (green circles), 2-component galaxies (purple squares) and peculiars (yellow triangles).

3.3 Method

3.3.1 Structural parameters

In Chapter 2 we obtained the structural parameters of each galaxy in our sample from the *Hubble* WFC3 H-band images using GALFIT and GALAPAGOS. We fit the surface brightness with two models. Model 1 consists of a single Sérsic profile, with n as a free parameter, and represents well a 1-component galaxy. Model 2 describes a galaxy with two components, represented by an inner Sérsic and an outer exponential profile. From the best fit to model 1 systems we obtain the following parameters: position of the galaxy within the image stamp (x, y), effective radius R_e, Sérsic index n, AB-magnitude m, axis ratio q and position angle PA. On the other hand, for model 2: position in the stamp (x, y), effective radius of bulge and disc component $(R_{e\,\mathrm{B}}, R_{e\,\mathrm{D}})$, Sérsic index of the bulge n_{B}, AB-magnitude for bulge and disc $(m_{\mathrm{B}}, m_{\mathrm{D}})$, axis ratio of bulge and disc $(q_{\mathrm{B}}, q_{\mathrm{D}})$ and position angle of both components $(PA_{\mathrm{B}}, PA_{\mathrm{D}})$. We exclude any fitting with unphysical parameters: effective radius smaller than 0.5 pixels, or larger than the size of the image stamp, $q < 0.1$, and $n < 0.5$ or $n > 8$, which implies that about 8% of the galaxies are not well represented by either model 1 or model 2. These galaxies which are not fit are either very compact objects, or considerably faint/small, and have an average redshift of $z = 2$.

3.3.2 Multiwavelengh study

To extend our study to a broader range in wavelength than previously done, we use the other bands available from *HST* in the CANDELS/UDS field (J, i, V bands). In the redshift range of $1 < z < 3$ the observed H-band samples the underlying stellar mass better than bluer wavelengths, and therefore we adopt the structural parameters of Sérsic index and radius obtained from fitting to the H-band for the other wavelengths to measure consistent fluxes within the same physical area. Using GALFIT we fit the surface brightness with models 1 and 2, with all the parameters in each model fixed to those of the best fit determined by the H-band fit, but allowing the magnitude/s to vary as a free parameters. This implies for model 1 keeping fixed the position on the stamp, the effective radius, Sérsic index, axial ratio and position angle. For model 2 we fix the position on the stamps, the effective radius of the disc and the bulge, the Sérsic index of the bulge, the axial ratio and position angle for bulge and disc. The sky level for each object, in the different bands, is calculated using GALAPAGOS (Barden *et al.* 2012). We run GALAPAGOS in each band using the detections determined from the H-band, and obtain the local sky around all the objects in our sample, as explained in Barden *et al.* (2012).

3.3.3 SEDs

Once we obtain a full SED for our components, the stellar masses are measured using SMPY (Duncan *et al.* 2014), a template fitting code with SEDs derived from the synthetic stellar population models of Bruzual & Charlot (2003). The model SEDs are generated from a single stellar population. We use the initial mass function (IMF) of Chabrier (2003). Nebular emission lines are added to the pure stellar component, and dust extinction in included in the templates using the extinction law of Calzetti *et al.* (2000). The star formation history (SFH) is characterised by an exponentially declining model with various ages, metallicities and dust extinctions.

$$SFR(t) \propto SFR_0\, e^{-t/\tau}, \tag{3.1}$$

where the values of τ ranges between -10 to 10 Gyr (negative τ values represent exponentially increasing histories). Age ranges from 0.02 to 9.6 Gyr, dust attenuation is allowed to vary from $0 \leq A_V \leq 4$, and metallicity fraction Z/H from 0.0001 to 0.05.

Next, each SED template is redshifted in the range $1 \leq z \leq 3$ in steps of $\Delta z = 0.02$ and attenuation by intergalactic neutral hydrogen is applied following the prescription of Madau (1995). Finally, the resulting grid of SEDs is integrated through the response filter for each of the observed band, dimmed by the corresponding distance modulus for each redshift. The fitting of our SEDs to the observed photometry is done using a Bayesian-like approach. For a given stellar mass M and template type t, the normalized likelihood is given by

$$L(M,t) = \frac{e^{-\frac{1}{2}\chi^2(M,t)}}{\sum_{t'} \int dM' \cdot e^{-\frac{1}{2}\chi^2(M,t)}}. \tag{3.2}$$

The sum in the denominator is performed over all the templates, and the χ^2 value is given by

$$\chi^2(M,t) = \sum_{j}^{N_{filters}} \frac{(M \cdot F_j(t) - F_j^{obs})^2}{\sigma_j^2}, \tag{3.3}$$

where $F_j(t)$ is the template flux in the j filter, while F_j and σ_j^2 are the observed flux and observed flux error, respectively, in the j. However, there are significant degeneracies in the fitting procedure, particularly between dust, age and metallicity (see Dunlop *et al.* 2013 for a detail discussion), and various combinations of the free parameters can produce equally acceptable fits. The main sources of uncertainty in stellar mass comes from the degeneracies in the fitting and the lack of knowledge of the correct SFH. In addition, the uncertainty in stellar mass depends on the rest-frame wavelength coverage of the photometry (Mobasher *et al.* 2015).

As we show in Appendix B, to be able to obtain reliable rest-frame colours, SFRs and stellar masses from the SED fitting, we need photometry not only in the four *HST* bands but also in the U band, K band and Spitzer channel 1 at $3.6\mathrm{nm}$ ($ch1$). However, we do not have high enough resolution images in these bands to perform our bulge to disc decompositions for our sample of galaxies.

We therefore make use of the photometric catalogue from Galametz *et al.* (2013). The photometry from this catalogue is performed with a different method, using different apertures than in this work, and so, we cannot simply combine both catalogues. However, it is a fair assumption that colours (in particular $U-V$, $H-K$, $H-ch1$) are the same

in both catalogues, that is:

$$\begin{aligned}(U_{this\ work} - V_{this\ work}) &= (U_{Galametz13} - V_{Galametz13}) \\ (H_{this\ work} - K_{this\ work}) &= (H_{Galametz13} - K_{Galametz13}) \\ (H_{this\ work} - ch1_{this\ work}) &= (H_{Galametz13} - ch1_{Galametz13})\end{aligned} \tag{3.4}$$

We then obtain the magnitudes we would derive if we would have measured the resolved imaging on the missing bands - i.e. $U_{this\ work}$, $K_{this\ work}$ and $ch1_{this\ work}$, and incorporate them to our photometric catalogue. In Appendix B we explore how our results from the SED fitting improve by adding these three bands to our photometry.

For the 2-component systems we make another assumption, because the Galametz *et al.* (2013) catalogue does not have bulge to disc decomposed photometry. We first estimate, from a sample of nearby galaxies (see Appendix B for details), how the B/T changes as a function of wavelength over a broad range, and use this information along with the previously calculated magnitudes ($U_{this\ work}$, $K_{this\ work}$ and $ch1_{this\ work}$) to infer the magnitudes for the bulge and disc component in K, $ch1$ and U band.

In Figure 3.2 we compare the stellar masses from the initial catalogue we selected our sample from (Mortlock *et al.* 2015) to those masses calculated in this work, assuming all galaxies have a single component. On average the stellar masses calculated in this work are 0.2dex larger, which is within the nominal error budget of stellar mass measures (e.g., Mortlock *et al.* 2015). The systematic offset found in Figure 3.2 between the two mass estimates could arise from using different fitting codes and free parameters as well as from the difference in wavelength coverage. The large scatter may be cause by the errors in the stellar masses due to degeneracies in the SED fitting. Through the rest of the Chapter we use these new masses.

For the 2-component galaxies we have photometry for both the bulge and the disc, and therefore we are able to perform SED fitting for each component separately allowing us to measure stellar masses and SFRs within both components. In Figure 3.3 we consider the 2-component galaxies, and compare the stellar mass (left) and SFR (right) assuming that their light is in a single component, to the sum of the stellar mass/SFR of each separate component. We find a good correlation between the stellar masses measured between 1-

and 2-component systems. There is also a good correlation between the star formation measured, but with a higher scatter.

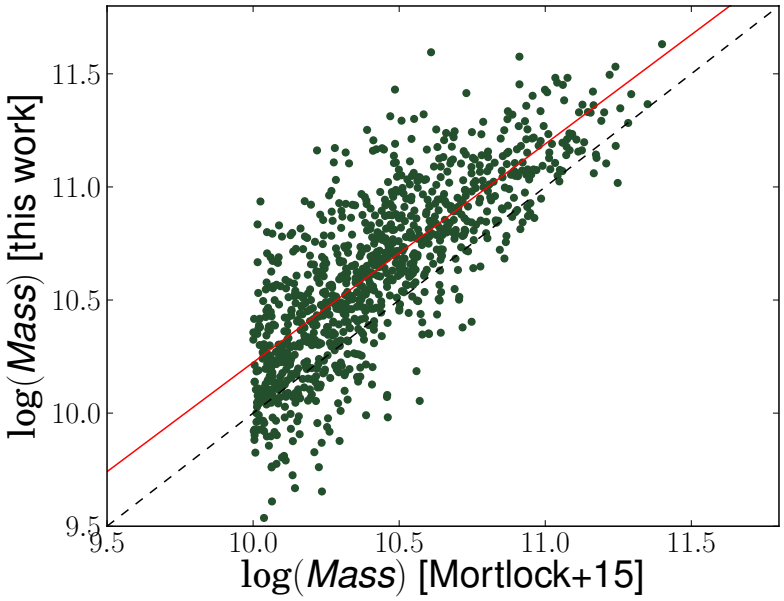


Figure 3.2: Comparison between the stellar masses calculated in this work and in Mortlock *et al.* (2015). This is assuming that the light profiles are in single Sérsic fits. The dashed line is a 1:1 relation between the two measures of the stellar masses. The red line is the best fit line to the data.

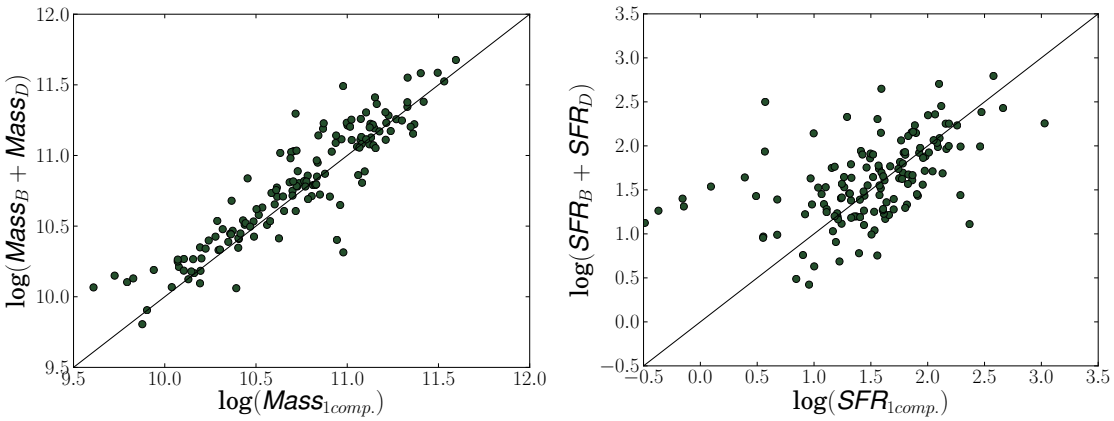


Figure 3.3: Comparison between the 2 and 1 component models for galaxies classified as 2- component systems. Left: Total stellar mass of the galaxies as given by the mass of the bulge and disc ($Mass_B + Mass_D$) from the 2-component model compared to the total mass of the galaxy obtain from the 1-component model. Right: total $SFR = SFR_B + SFR_D$ from the 2-component model compared to the SFR obtained from the 1-component fitting.

3.3.4 Star formation rates

The rest-frame UV is a good SFR indicator, as it traces the presence of young and short live O and B stars produced by recent star formation. Furthermore, the UV is the only star

formation indicator which we can use to resolve the SFHs in galaxies (e.g., Ownsworth *et al.* 2012). By applying a scaling factor of the UV luminosity, the SFR can be calculated, however, this depends on the assumed IMF (e.g., Kennicutt 1983). The downside of calculating the SFR from the UV luminosity is its susceptibility to dust extinction, and therefore a dust correction has to be applied. We use a correction based on the UV slope, which is explained below.

To calculate the SFR we obtain the rest-frame UV luminosities (at 2800Å) from the best fit SED model of the stellar mass fitting, we then use the Kennicutt (1998) conversion from 2800Å luminosity to SFR assuming a Chabier IMF:

$$SFR_{UV}(M_{\odot}\mathrm{yr}^{-1}) = 8.24 \times 10^{-29} L_{2800}(\mathrm{ergs\ s^{-1}Hz^{-1}}). \tag{3.5}$$

This gives the SFR before a dust correction is applied.

Dust correction

We use the UV slope as an estimate for the dust extinction. Meurer, Heckman & Calzetti (1999) found a correlation between the UV slope β and the attenuation due to dust. Following the method described in Ownsworth *et al.* (2016) we use ten UV windows defined by Calzetti, Kinney & Storchi-Bergmann (1994) to measure β by interpolating the flux in these windows from the SED fitting. We then convert the slope into a dust correction using the Fischera & Dopita (2005) dust model

$$A_{2800} = 1.67 \cdot \beta + 3.71.$$

However, the UV slope can also be affected by the age of the stellar population. Galaxies with old and passive stellar populations may have similar SEDs as highly obscured galaxies with young star-forming population. This means that passive galaxies can appear to be highly dust obscured, and thus we would derive higher SFR than they actually have.

To solve this problem we treat differently the passive and star-forming galaxies as selected by the UVJ diagram. We only use these dust corrections calculated by the UV slope for galaxies selected as star-forming within the UVJ diagram. For the passive population we assume that star-forming and passive galaxies have similar dust masses (e.g., Bourne *et al.* 2012). We therefore assume that, on average, passive galaxies have the same dust attenuation as star-forming ones within a range of redshift and similar stellar masses.

3.4 Results

In the following section we discuss the properties of the inner and outer components of our galaxy sample. We first describe the colours and the location of our components on a UVJ colour-colour diagram to put some constrains on the passivity and star formation presence within discs and bulges. We later discuss the directly measured SFRs of these galaxy components, as well as the stellar masses, and how these properties change with time.

3.4.1 Colours

Studying the colours of galaxies gives us information about the star formation activity of each component. That is so because blue objects indicate star formation activity, while red colour signifies that a galaxy is passive or dusty. The U, V and J rest-frame magnitudes are calculated from the flux measured by the U, V and J Bessel filters in the best SED model during the SED fitting. We divide our sample into star-forming and passive galaxies using the rest-frame UVJ colours, where a galaxy is classified as red/passive if it satisfies the following criteria (see Mortlock *et al.* 2013).

$$\begin{cases} (U-V) > 1.3 \\ (V-J) < 1.6 \\ (U-V) > 0.88(V-J) + 0.49 \end{cases} \tag{3.6}$$

and as blue otherwise.

Figure 3.4 shows where the 1-component galaxies in our sample lie in the UVJ diagram. The majority of disc-like galaxies, $78 \pm 6\%$, are in the star-forming region of the UVJ diagram, while $67 \pm 6\%$ of spheroid-like galaxies are in the passive region. This is consistent with the idea that galaxy morphology correlates with colour, and therefore star formation activity, in such a way that disc-dominated galaxies are more likely to be blue and star forming, while elliptical or spheroid-dominated galaxies are passive. However, note that this is only for galaxies which are best fit as single components, which in the nearby universe would be early-type ellipticals and pure disc galaxies.

We see something similar, but with some differences, when we look at the UVJ colours of the disc and bulge components. As can be seen in Figure 3.5, the majority of both

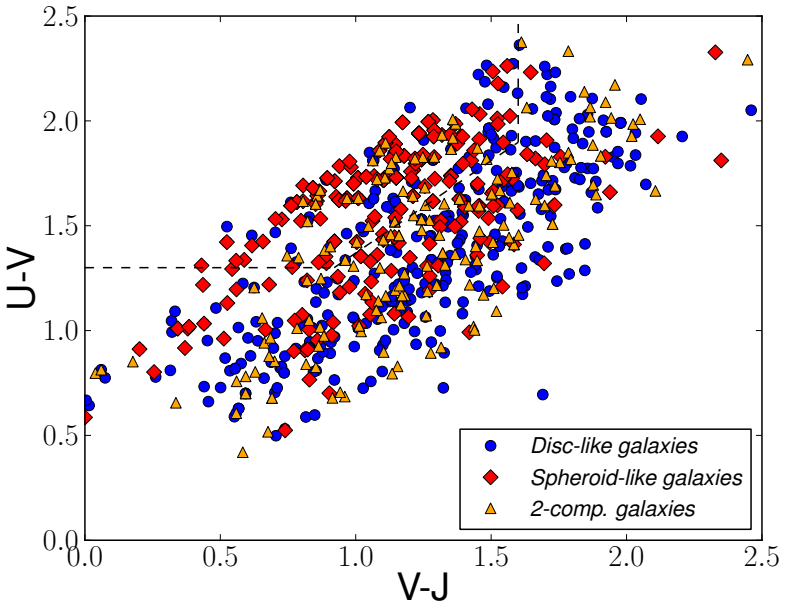


Figure 3.4: UVJ diagram for 1-component galaxies. The box in the left top corner represents the passive population (equation (3.6)).

bulges and discs are within the star-forming region ($68 \pm 9\%$ and $90 \pm 11\%$ respectively). However, a significant fraction of star-forming bulges, 30%, are in the dusty region of the diagram, while only 17% of star-forming discs lie in that region. The inner parts of two-component galaxies are therefore red due to the dust according to the UVJ diagram, rather than because of an old stellar population. The fraction of passive and star-forming objects are summarized in Table 3.1.

	Star-forming	Passive
1-comp. discs	$78 \pm 6\%$	$22 \pm 3\%$
1-comp. spheroids	$43 \pm 5\%$	$67 \pm 6\%$
2-comp. discs	$90 \pm 11\%$	$10 \pm 3\%$
2-comp. bulges	$68 \pm 9\%$	$32 \pm 5\%$

Table 3.1: Fraction of galaxy components that are passive and star forming, according to the UVJ selection given by equations (3.6).

We furthermore study the rest-frame $U - V$ colour as a function of stellar mass and redshift (Figure 3.6). We find that there is a trend with stellar mass for all types of galaxies and components, such that the rest-frame $U - V$ colour becomes redder at higher stellar masses as seen in Figure 3.6. There we plot the rest-frame $U - V$ colour as a function of stellar mass for 1-component galaxies (top panels) and for 2-component galaxies (bottom panels). On the left side we show the effect of the Sérsic morphology, and on the right

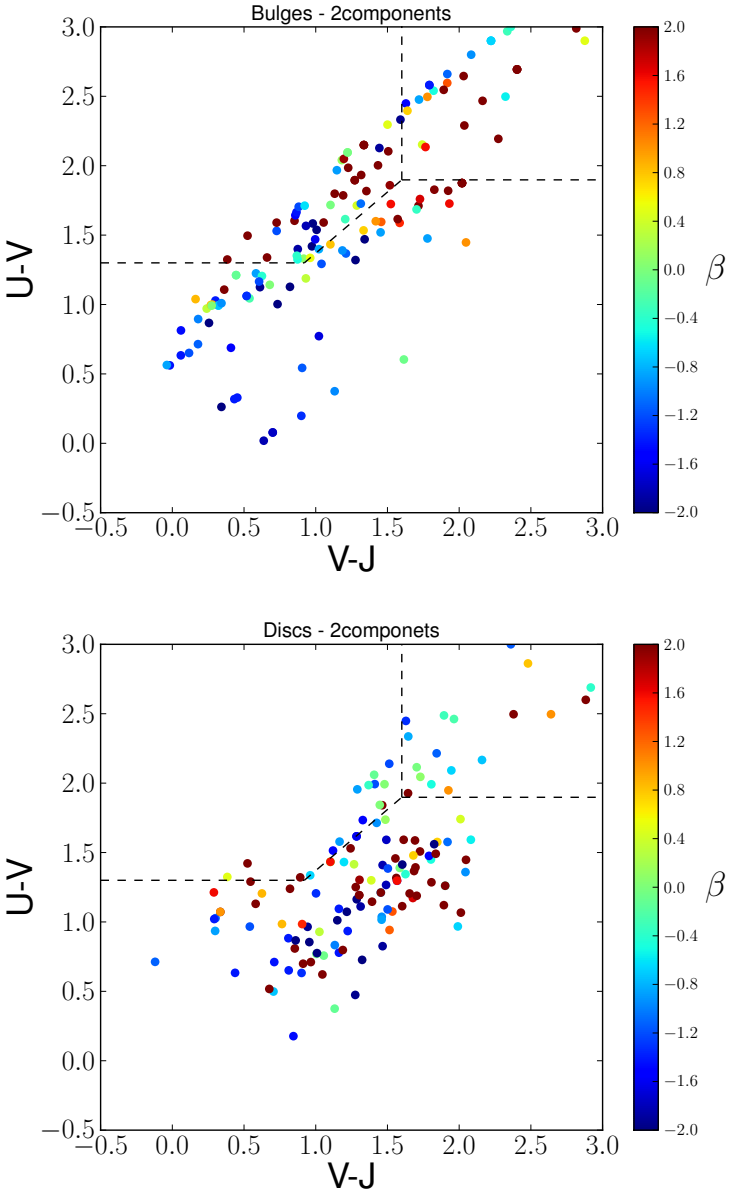


Figure 3.5: UVJ diagram for bulges (top) and discs (bottom) of 2-component galaxies. The box in the left top corner represents the passive population (equations (3.6)), and in the right top corner we find the dusty region. The colour bar represents the UV slope β.

we investigate the relation between the $U - V$ colour and stellar mass as a function of redshift.

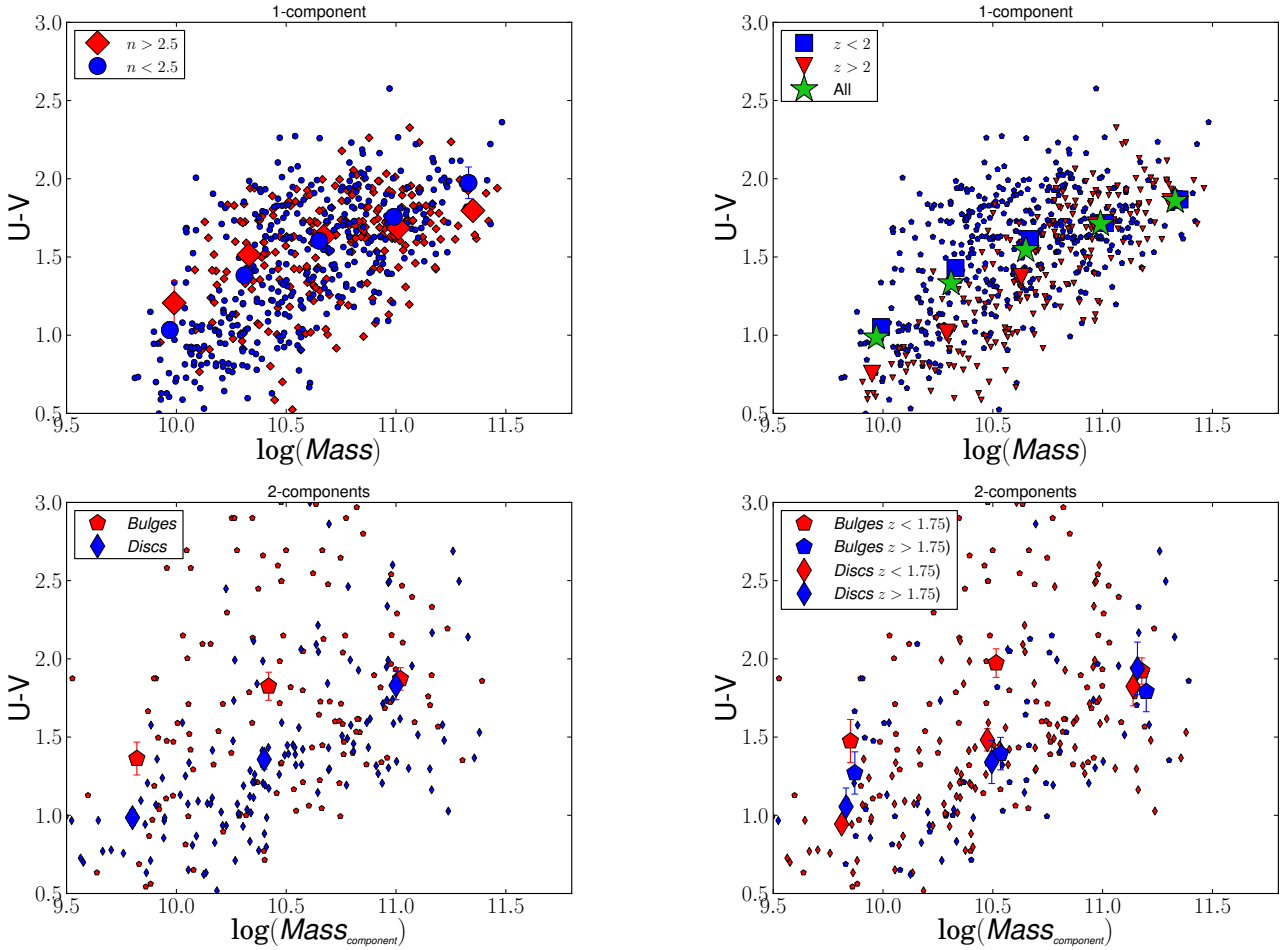


Figure 3.6: Rest-frame $U - V$ colour as a function of stellar mass. On the top panels we show the 1-component galaxies separated by Sérsic index (left), where blue diamonds are galaxies that have $n > 2.5$ (i.e. spheroid-like) and blue circles are for galaxies with $n < 2.5$ (disc-like); and by redshift (right), where blue squares are galaxies at $z < 2$, and red triangles are galaxies at $z > 2$. On the bottom panels we show the 2-component galaxies. Left: $U - V$ colour of bulges and discs as a function of the stellar mass of the component. Right: bulges and discs of 2-component galaxies separated in two redshift bins.

For the 1-component galaxies, the structure of a galaxy, as measured through the fitted Sérsic index, has a small effect on the colour over all redshifts. That is, we find the $U - V$ colour to be similar between disk-like and spheroid-like systems, but there are some differences. In Figure 3.7 (top panel) it appears that spheroid-like single component galaxies have slightly redder colours that disc-like galaxies at all redshifts, however this is the case only for galaxies with $\log M_* < 11$ (as seen in Figure 3.6). This apparent discrepancy arises from the fact that in Figure 3.7 the colours of galaxies with different masses are averaged, and galaxies with $\log M_* < 11$ are more numerous than the most massive ones.

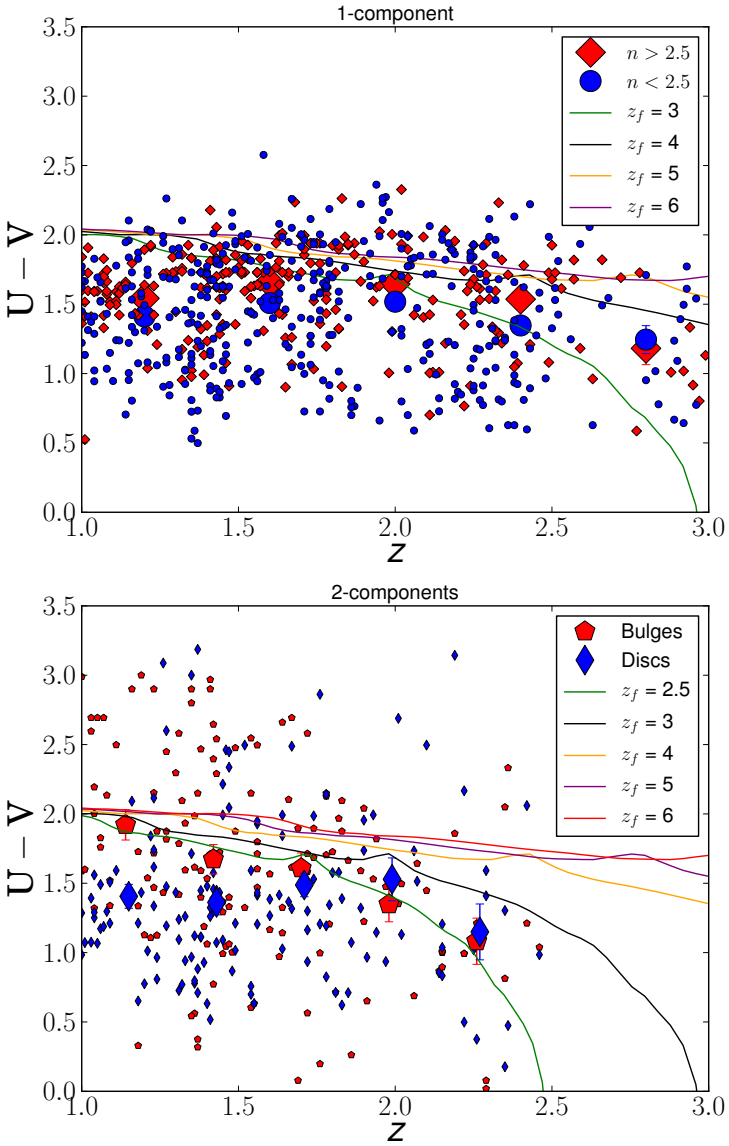


Figure 3.7: Rest-frame $U - V$ colour as a function of redshift. Top panel: 1-component galaxies separated by Sérsic index, where blue circles are disc-like galaxies ($n < 2.5$), and red diamonds are spheroid-like ones ($n > 2.5$). Bottom panel: 2-component galaxies, with bulges represented as red pentagons and discs as blue diamonds.

Nonetheless, the colour of disc-like and spheroid-like galaxies is comparable and, therefore, 1-component galaxies must have similar SFHs at similar stellar masses (Figure 3.7). We also observe that the colour changes with redshift significantly, particularly for galaxies with $\log M_* < 11$; lower mass galaxies become redder with time. The most massive galaxies are also the reddest and do not seem to become bluer with decreasing redshift. This shows that the most massive galaxies establish their red colour earlier than lower mass galaxies.

For the 2-component galaxies we also observe a difference in the evolution of colours according to the stellar mass of the components. The most massive bulges and discs ($\log M_* > 11$) have similar colours which do not change with redshift (Figure 3.6). Less massive bulges and discs ($\log M_* < 11$) change in colour in different ways through cosmic time. Although they may have a similar initial formation, as seen by their comparable colours at $z > 1.75$, at lower redshifts ($z < 1.75$) bulges become redder than discs. Therefore, low redshift bulges are redder than high redshift bulges, showing little new star formation. There is however no significant evolution of disc colour with redshift, for a given mass, which implies a continuous star formation, as seen in Figure 3.7, where we also observe how bulges become redder and therefore more passive in Figure 3.7.

In Figure 3.7 we overplot the $U - V$ colour evolution tracks derived from Bruzual & Charlot (2003) single stellar population models formed with a burst in star formation at different redshifts ($z = 2.5, 3, 4, 5, 6$). The average of the $U - V$ colour for bulges of 2-component galaxies is consistent with a galaxy that had a single star formation burst at $z = 2.5$. The discs of 2-component galaxies have bluer colours than any of the model tracks, which implies that they must have undergone continuous star formation activity. An analogous result holds for 1-component galaxies.

3.4.2 Star formation rates of inner and outer components

We know that there is a tight relation between stellar mass and SFR for star-forming galaxies, sometimes called the 'main-sequence' Noeske *et al.* (2007), with SFR increasing with stellar mass. For 1-component galaxies, we find that the SFR increases with stellar mass (Figure 3.8). In Figure 3.8 we show the star-forming main-sequence for disc-like and spheroid-like galaxies. For 2-component galaxies, a main-sequence is seen in the

star-forming discs, while the star-forming bulge have a wider range of SFR for a given stellar mass.

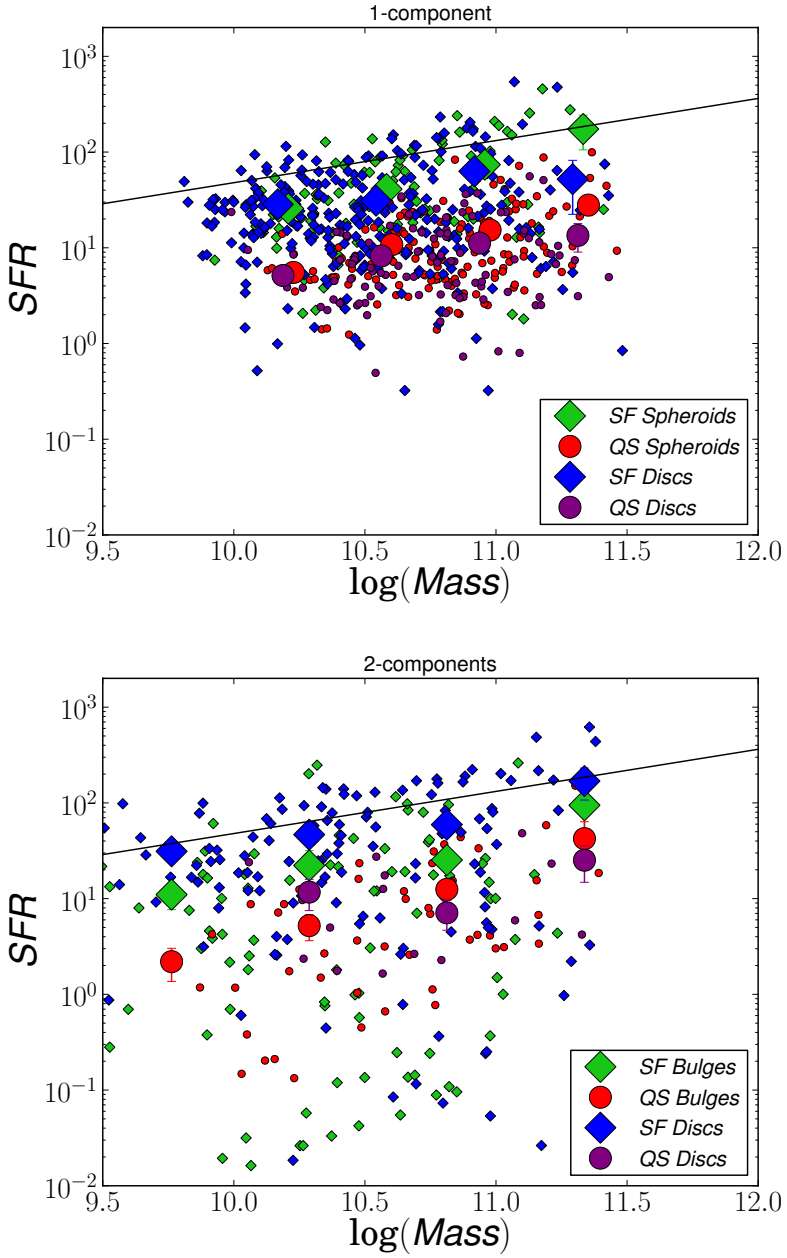


Figure 3.8: SFR as a function of stellar mass for 1-component galaxies (top) and 2-component galaxies (bottom), separated by their position on the UVJ diagram (i.e. passive or star forming). The black lines are the SFR-mass sequence for star-forming galaxies found by Whitaker *et al.* (2012) at $z = 2$.

This shows that the production of the main-sequence is driven by the formation of discs, and that the observed correlation between stellar mass and star formation for 2-component systems is driven by the formation of their outer portions, or discs. This is likely because the discs contain most of the gas which is converted into stars through star formation.

We also examine how the ratio of star formation in the inner and outer components changes with redshift and mass. The ratio of SFR of bulges and discs is on average lower than unity at all masses (Figure 3.9). This implies that the majority of galaxies tend to have higher SFRs in their discs than their bulges.

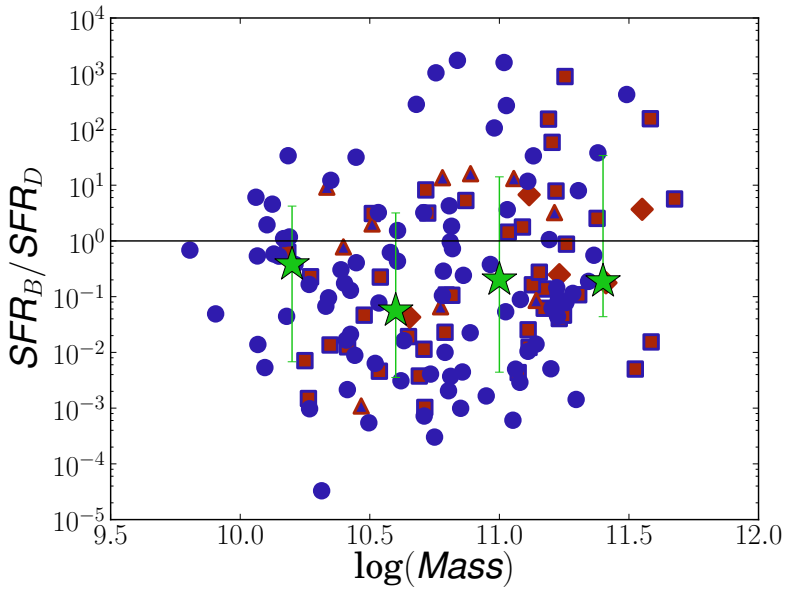


Figure 3.9: Ratio between SFR of bulges and discs, as a function of the stellar mass of the galaxy ($Mass_B + Mass_D$). The inner part of the symbols represents the bulge and the outer disc. Red colour indicates that a certain component is passive while blue indicates that it is star forming. Blue circles are galaxies in which both the bulge and the disc are star forming, red diamond are galaxies that are passive. A square represents a galaxy with a passive bulge and a star-forming disc. Finally, a triangle indicates a star-forming disc and passive bulge. Green stars are the median value in stellar mass bins. The error bars show the dispersion of the data.

Figure 3.10 shows the ratio of SFR of bulges and discs with redshift. High redshift bulges have high SFR but, as redshift decreases, they become more passive while their discs become more star forming. This is seen as well with the ratio of sSFR (Figure 3.11) thus the effect is not one of a differential in mass between the components. Furthermore, the 1-component galaxies show a trend of sSFR (specific SFR) with stellar mass (Figure 3.12, top panels). This trend does not change significantly with morphology. However, we observe a difference with redshift: high redshift objects have a stepper relation of sSFR with stellar mass. In particular the sSFR of the most massive galaxies increases with decreasing redshift between $z = 3$ to $z = 1$. Bulges appear to have a lower sSFR than discs (Figure 3.12, bottom panels). However, this is only seen in low redshift bulges, which have very low sSFR values. High redshift bulges have as high sSFR as high redshift discs. The sSFR of discs does not change with redshift.

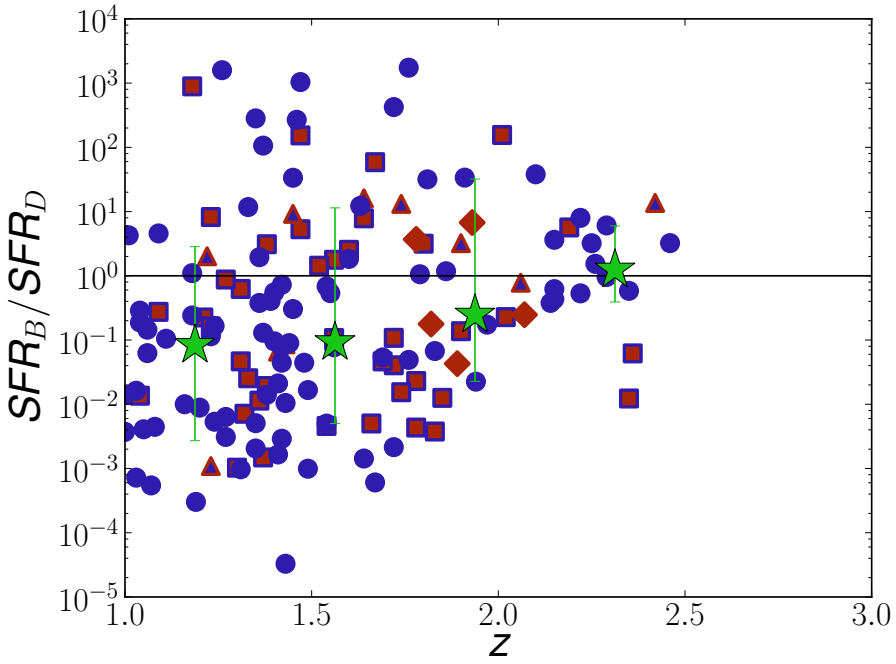


Figure 3.10: Ratio between SFR of bulges and discs, as a function of redshift. Colours as in Figure 3.9. Green stars are the average over redshift bins. The error bars show the dispersion of the data.

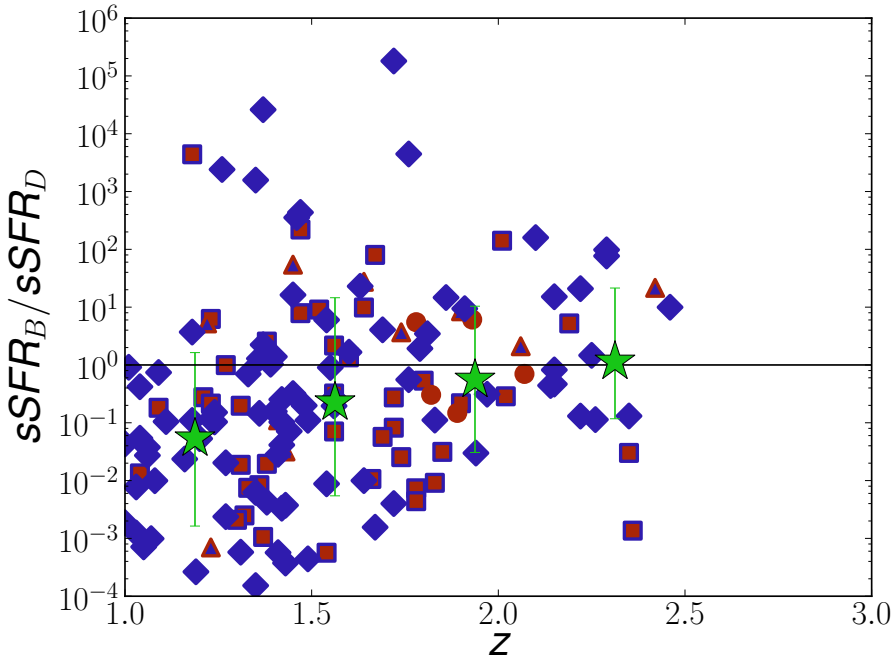


Figure 3.11: Ratio between sSFR of bulges and discs, as a function of redshift. Colours as in Figure 3.9. Green stars are the average over redshift bins. The error bars show the dispersion of the data.

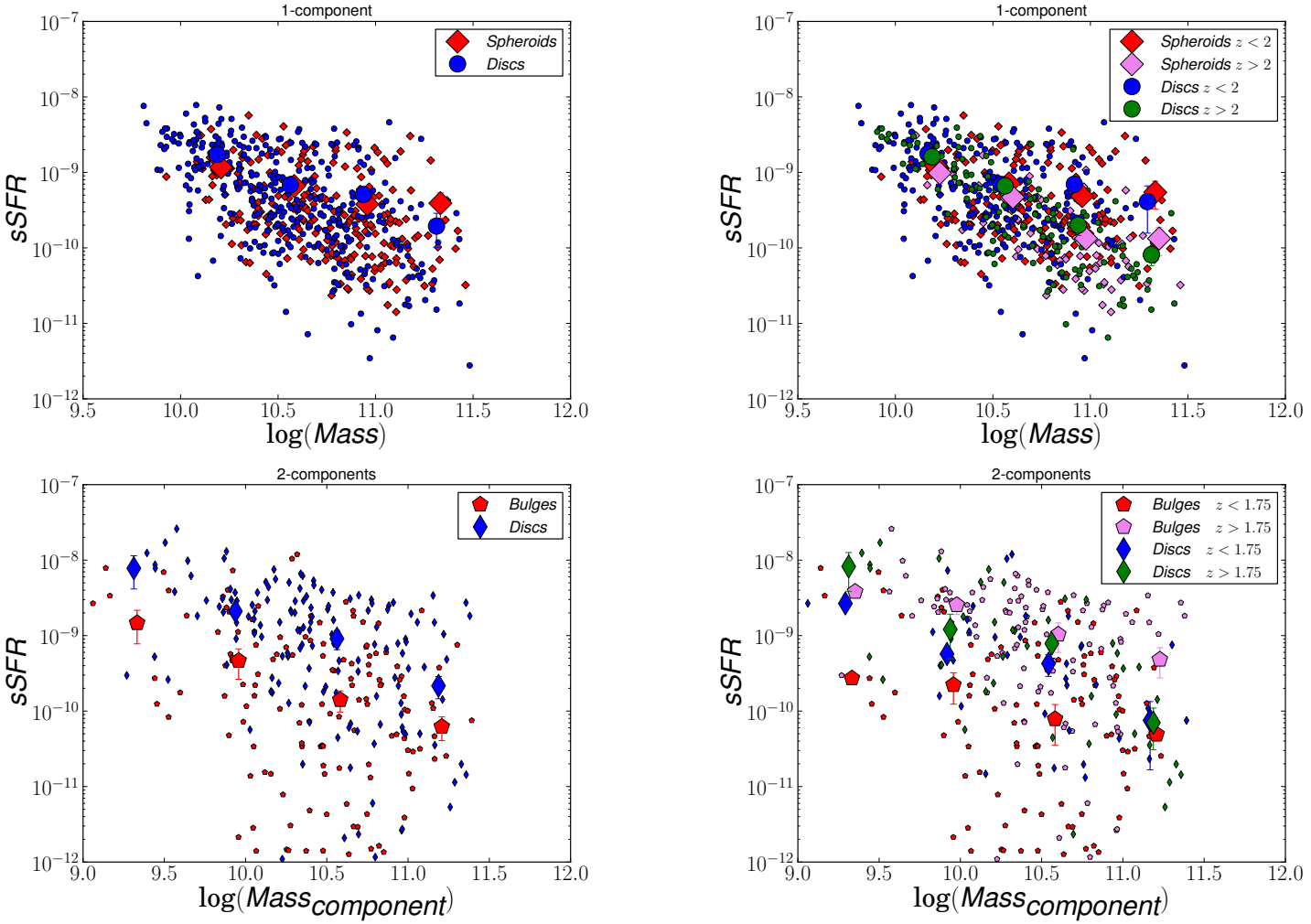


Figure 3.12: sSFR as a function of stellar mass. On the top left panel we represent the 1-component galaxies divided by morphology (disc-like galaxies as blue circles and spheroid-like ones as red diamonds). On the right top panel we further split these two types of galaxies into two redshift bins and, analogously, for the bulges and discs of the 2-component objects in the bottom panels. The large symbols are the average sSFR values in each mass bins.

3.4.3 Stellar masses of components

The ratio of stellar mass between the bulge and the disc is on average constant with time (see Figures 3.13 and 3.14). This shows that whilst the masses of both of these components must be changing with time due to star formation, the growth in both of them goes roughly together. It is easy to see how this occurs for the star-forming outer portions, but the account for the mass assembled in the inner portion, or bulge, is not so direct as it does not have a constant high SFR. We discuss this later in the discussion section about how this process may occur.

As Figure 3.14 shows, there is a relatively good agreement between the masses of the bulges and discs over cosmic time. There is an increase in the average stellar mass, using our selection, between $z = 2.5$ and $z = 2$, and a levelling off of the stellar mass for the two components at later times. If we investigate this as a function of co-moving density using the derivation for our sample from Ownsworth *et al.* (2016), we find that from $z = 2.5$ to $z = 1$ the stellar mass of the bulges increases slightly on average, while there is some decrease in the stellar mass of the bulge. This may however be due to other morphological transformations.

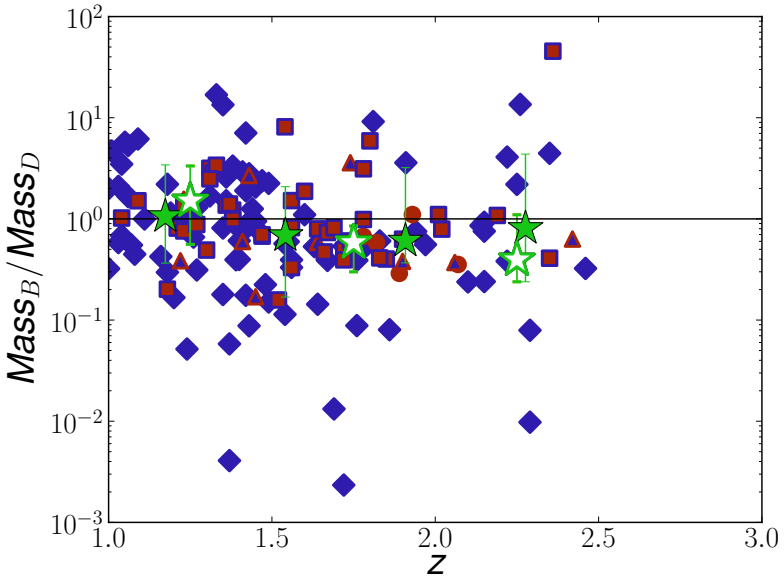


Figure 3.13: Ratio between stellar mass of the bulges and discs as a function of redshift. The green stars indicate the mean values in redshift bins for all 2-component galaxies. The open star symbols represent the average values for a constant number density selection. Colours are as in Figure 3.9. The error bars show the dispersion of the data.

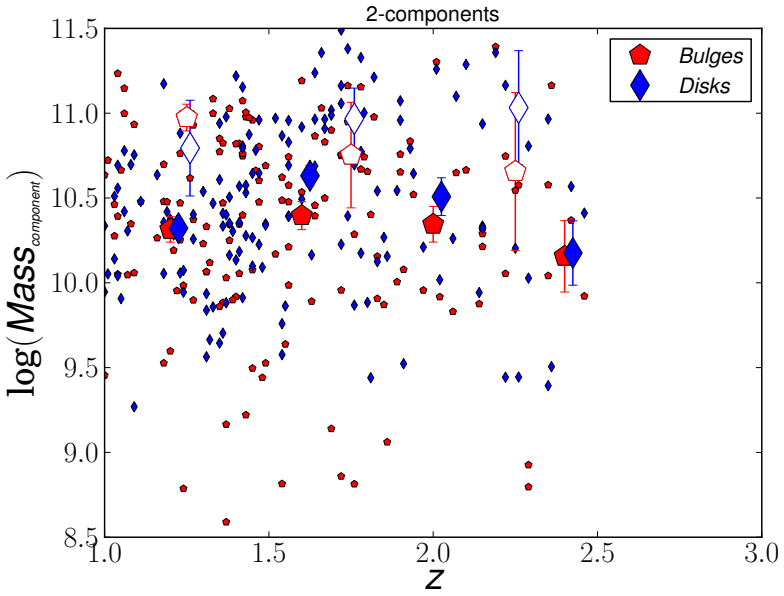


Figure 3.14: Stellar mass of bulges (red pentagons) and discs (blue diamonds) as a function of redshift. The big filled symbols are the average stellar mass in redshift bins for all the 2-component galaxies. The big open symbols are the average for a constant number density selection (see text).

3.4.4 Presence of AGN

To identify active galaxies we cross match our galaxy sample with the Chandra X-ray catalogue from Kocevski et al. (2017 in prep.). We find that AGNs are more common in spheroid-like galaxies, or 2-component galaxies, with $11 \pm 2\%$ of spheroid-like galaxies and $13 \pm 3\%$ of 2-component galaxies having an AGN, while only $3 \pm 1\%$ of disc-like galaxies have an AGN. This shows that the presence of the bulge is correlated with the presence of an AGN, even at high redshift.

In Figure 3.15 we compare the SFR of galaxies which have an AGN to those that do not have AGN activity. On the top panel we see that 1-component galaxies with AGN have higher SFR. The difference is stronger for the spheroids. In the bottom panel we show the SFR of the bulge and the disc components for galaxies with and without AGN. We again observe that galaxies with AGN have higher rates of star formation in both components.

Is it possible that the higher SFR observed is due to the AGN contaminating the host galaxy light (Nandra *et al.* 2007; Simmons & Urry 2008), as AGNs are generally bright in the ultraviolet, which could affect the determination of the SFR from the UV slope. However, in the 2-component galaxies we observe that the SFR of AGN is higher both in the inner and outer component, although it is expected that only the inner component would be affected by the AGN contamination.

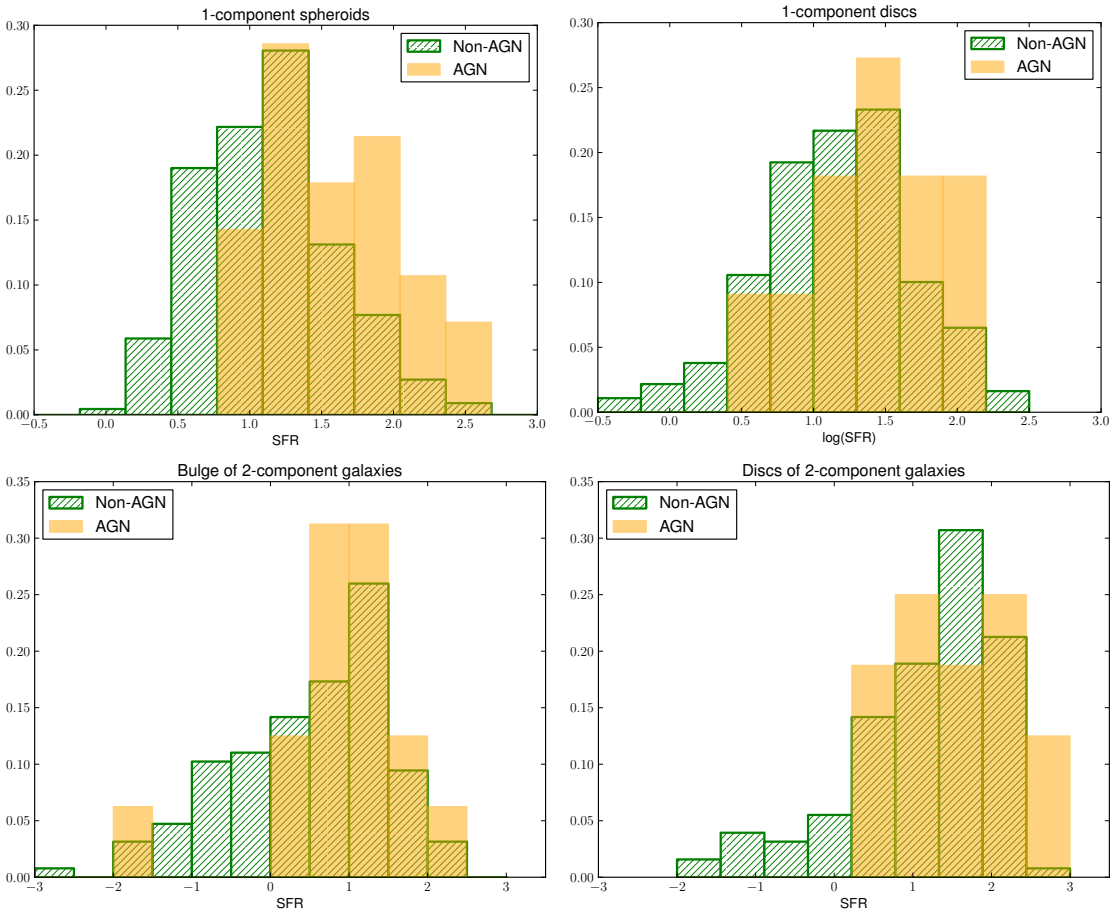


Figure 3.15: Comparison between the SFR of galaxies with and without the presence of AGN. The top panels show the distribution of $\log(SFR)$ for the 1-components spheroids (left) and discs (right), for galaxies with AGN (solid yellow) and without AGN (strip lines green). The analogous for 2-component galaxies is shown in the bottom panels for bulges (left) and discs (right).

3.5 Conclusions

In this Chapter we investigate the properties of the inner and outer portions of galaxies to determine how their formation occurred. To do this we investigate the technical aspects of performing this analysis, using simulations and determining that the SFRs and the stellar masses of both the inner and outer components can be retrieved by assuming that the inner to outer light ratios and properties are similar at the two ends of our ViJH fitting (see Appendix B). We show that, when examining the bulge to disc ratio for nearby galaxies, this approach is valid, i.e. that the bulge to disc ratio does not change significantly with wavelength. This is likely even truer at higher redshifts where the visual morphologies of galaxies and their measured structures do not change as much as for nearby galaxies (e.g., Conselice, Bershady & Jangren 2000; Taylor-Mager *et al.* 2007).

We then decompose our galaxies into inner and outer portions and derive the colours, stellar masses, and SFRs for these components. We show that, when we compare the sum of the SFR and stellar mass for the 2-component systems to the 1-component measurement, we obtain a strong correlation. This shows that our method of decomposition is reliable and consistent (see also Margalef-Bentabol *et al.* 2016).

When we examine the location of our systems in a UVJ diagram we find that the vast majority of discs and around $^2/_3$ of bulges fall into the star-forming region of the UVJ space. Therefore, a higher fraction of the bulges are passive. However, what we do find is that many of these star-forming inner components are found in the UVJ part of the diagram occupied by dusty star-forming systems. Thus, whilst these inner components, or forming bulges, are red, they are not necessarily old because a significant fraction at $z > 1$ are found in the dusty star-forming region of the UVJ space. Nonetheless, the SFR and sSFR of these bulges are not as high as for discs or outer components.

We find also that massive ($\log M_* > 11$) galaxies and galaxy components establish their rest-frame colour by $z = 3$ and are the reddest objects amongst our sample. Besides, these objects do not show evolution in colour with redshift, remaining red and passive.

Moreover, we find a significant difference between the location in the UVJ space of best-fit single profiles (see Margalef-Bentabol *et al.* 2016) for systems that are disc-like and those that are spheroid-like. The disc-like objects have a similar fraction of star-forming galaxies to the 2-component systems, at $78 \pm 6\%$, whereas those systems that are more spheroid-like have a star formation fraction of only $43 \pm 5\%$. This shows that the 2-component galaxies have a similar broad SFH to 1-component disc-like galaxies.

We also find that on average the ratio of stellar mass of the bulge and the disc remains constant with redshift, while the ratio of SFR decreases with decreasing redshift (Figure 3.10). Besides, discs become more star forming than bulges. This supports the idea that galaxies form inside out (Dullo & Graham 2013; Graham, Dullo & Savorgnan 2015; de la Rosa *et al.* 2016), possibly with mass accreting into the disc inducing its star formation. This is consistent with the gas accretion model for how star formation is triggered in these galaxies (Dekel *et al.* 2009; Conselice *et al.* 2013). The majority of the star formation in these galaxies is occurring within the discs, precisely at the location where we would expect it to be.

Finally, since we find that the stellar mass ratio between bulges and discs is similar over cosmic time, there must be a conversion of mass from the disc (or outer component) into the bulge (or inner component). This is due to the fact that if we integrate the SFR, and account for mass loss due to stellar evolution, we find that the mass of the inner components would grow by a factor of 0.3dex, whilst the outer components would decrease in stellar mass by 0.2dex.

Chapter 4

High redshift spirals

4.1 Introduction

Spiral structures are present in many discs with different morphologies, ranging from grand-design, in which prominent and well-defined spiral arms can be traced over large parts of the disc, to flocculent pattern, with fragmented spiral arms that have a more limited spacial extent. Different mechanisms are believed to be responsible for the morphology of spiral galaxies. The formation of grand design spirals can be explained by the density wave theory (Lin & Shu 1964; Bertin *et al.* 1989). This theory suggests that the spiral pattern is a wave that moves through the disc causing its stars and gas to clump up along the wave, moving with a velocity that is independent of the rotation of the disc. The flocculent arms are believed to be produced by local instabilities (Toomre 1990; Sellwood & Kahn 1991). Other studies also suggest that spiral structure can be driven by tidal effects due to an interaction with a companion galaxy or the presence of a central bar (Dobbs & Pringle 2010).

In the local universe, spiral galaxies are relatively common and they comprise one of the main broad categories of the Hubble sequence (Sandage 1961). However, they are very rare at high redshift, and only two grand-design spiral galaxies at $z > 2$ have been confirmed spectroscopically: HDFX 28 at $z = 2.011$ (Dawson *et al.* 2003, which may instead be a major merger resembling a spiral) and Q2343-BX442 at $z = 2.18$ (Law *et al.* 2012), proving that such structures can be detected at high redshift, although Q2343-BX442 is relatively massive ($\log M_* = 10.78$) and bright ($H = 22.04\ AB$). Therefore,

the current limit on instrumentation could be responsible for the low number of spiral galaxies detected at high redshift compared to lower redshifts ($z < 2$). However, the scarcity of spirals galaxies at $z > 2$ could have a physical explanation: at $z > 2$ discs are dynamically hot (Genzel *et al.* 2006; Law *et al.* 2009), which produces more often clumpy structures than spirals arms (Elmegreen *et al.* 2005). Minor mergers could also be responsible for the design of spiral patterns, as suggested by numerical simulations (Bottema 2003; Dobbs *et al.* 2010). This may explain why spiral galaxies are rare, as they need the galaxy to be massive enough to stabilize the disc, and also the presence of a merger whose perturbation induces the formation of a spiral.

In the previous Chapters we show that $1 < z < 3$ is the epoch when 2-component systems start to form and dominate, but there are different types of disc according to their morphology, in particular, discs with or without spiral arms. Another fundamental question in galaxy evolution is therefore when modern spirals appear. These objects are quite common in the local universe, but are difficult to study at high redshift due to redshift effects producing lower resolution and S/N. It has been found that at high redshift ($z \sim 2$) star-forming galaxies become increasingly irregular and clumpy (Elmegreen & Elmegreen 2005; Elmegreen *et al.* 2009). These clumpy galaxies may transition into spirals, after the dispersion of the clumps to form the discs (Elmegreen *et al.* 2009). It is debated the impact that spirals have on the star formation of the disc. Spirals may enhance the star formation, as they are site of high density of gas and young stars, at least in the local universe (Engargiola *et al.* 2003; Calzetti *et al.* 2005). However, there are some studies which suggest that the spiral arms do not affect the overall star formation in the host galaxy (Elmegreen 2002; Moore *et al.* 2012).

In this Chapter we investigate the properties of spiral discs and their evolution through cosmic time. We also compare this with the evolution of smooth discs without spiral arms. The structure of this Chapter is as follow: in Section 4.2 we describe the data used in this work. Section 4.3 is devoted to describing how we select the different types of galaxies for our study. In Section 4.4 the main results of the Chapter are gathered, and in Section 4.5 we discuss and summarize the results.

4.2 Data

Galaxy Zoo is an online citizen science project that started in July 2007, with a data set of around a million galaxies from the Sloan Digital Sky Survey (SDSS), in which volunteers were asked to classify the galaxies into ellipticals, mergers and spirals. In later phases, more detail morphological classification was achieved, by asking volunteers more complex questions such as the number of spiral arms or the size of the galaxies' bulges. For this work we use the classifications collected during the fourth release of Galaxy Zoo (Simmons *et al.* 2017). The 4th phase of Galaxy Zoo includes all detections with $H \leqslant 25.5$ from COSMOS, GOODS-S and UDS in the CANDELS Survey, comprising 49 555 images, and it provides detailed quantitative visual morphologies, including the overall galaxy's appearance and more specific features (such as the presence of spiral arms, a clumpy appearance or strength of the bulge). The images shown for classification are colour composites of ACS-i, WFC3-J and WFC3-H filters for the blue, green and red channels, respectively.

The CANDELS UDS data and image are explained in Chapter 2. For a detailed discussion of the CANDELS UDS region photometry see Galametz *et al.* (2013).

The GOODS-S CANDELS field contains photometry from the following bands (Guo *et al.* 2013)

- U (Blanco/CTIO).
- U (VLT/VIMOS, Nonino *et al.* 2009).
- $F435W$, $F606W$, $F775W$, $F814W$, $F850LP$ (HST/ACS, GOODS and CANDELS; Giavalisco *et al.* 2004 and Koekemoer *et al.* 2011).
- $F098M$ (HST/WFC3, ERS; Windhorst *et al.* 2011).
- $F105W$, $F125W$, $F160W$ (CANDELS+HUDF09; Koekemoer *et al.* 2011).
- Ks (VLT/ISAAC, Retzlaff *et al.* 2010).
- Ks (VLT/Hawk-k, Fontana *et al.* 2014).
- $3.6\mu m$, $4.5\mu m$ (Spitzer/IRAC, GOODS+SDES; Ashby *et al.* 2013).

- $5.8\mu m$, $8.0\mu m$ (Spitzer/IRAC, GOODS).

The COSMOS CANDELS field comprises the following photometry (see Nayyeri *et al.* 2017)

- $u*$, $g*$, $r*$, $i*$, $z*$ (CFHT/Megacam, CFHTLS; Gwyn 2012).
- B, g^+, V, r^+, i^+, z^+ (Subaru/Suprime-cam, COSMOS; Taniguchi *et al.* 2007).
- $F606W$, $F814W$ (HST/ACS, CANDELS; Koekemoer *et al.* 2011).
- $F125W$, $F160W$ (HST/WFC3, CANDELS; Koekemoer *et al.* 2011).
- $IA484$, $IA527$, $IA624$, $IA679$, $IA738$, $IA767$, $IB427$, $IB464$, $IB505$, $IB574$, $IB709$, $IB827$, $NB711$, $NB816$ (Subaru/Suprime-cam, COSMOS; Taniguchi *et al.* 2015).
- Y, J, H, K_s (VLT/VISTA, UltraVISTA; McCracken *et al.* 2012).
- J_1, J_2, J_3, H_1, H_2, K (Mayall/NEWFIRM, NMBS; Whitaker *et al.* 2011).
- $3.6\mu m$, $4.5\mu m$ (Spitzer/IRAC, SEDS; Ashby *et al.* 2013).
- $5.8\mu m$, $8.0\mu m$ (Spitzer/IRAC, S-COSMOS; Sanders *et al.* 2007).

4.2.1 Redshifts and stellar masses

We use the official catalogues of redshifts (spectroscopic redshifts are used when available) and stellar masses from CANDELS in order to have consistent measurements within the different fields. The UDS and GOODS-S photometric redshifts were determined using the method from Dahlen *et al.* (2013), which combines redshift probability distribution from several studies using a Bayesian approach, and thus improving the precision and reducing the number of catastrophic outliers. Stellar masses are drawn from the catalogue presented in Santini *et al.* (2014) using these photometric redshifts. For the COSMOS field, the photometric redshifts and stellar masses used for this work are determined in Nayyeri *et al.* (2017).

In Santini *et al.* (2014) stellar masses are estimated by fitting the photometry with a library of stellar synthetic SEDs from the stellar population of Bruzual & Charlot (2003). Star

formation histories are parametrized as exponentially declining laws, and a Chabier IMF is used. Redshifts are fixed to the photometric or spectroscopic when available, from Dahlen *et al.* (2013).

Photometric redshifts in Nayyeri *et al.* (2017) are calculated following the method from Dahlen *et al.* (2013). The redshift estimate for each galaxy is the median redshift from different methods. The confidence intervals are measured by combining the intervals from such different methods. These methods included various fitting codes using minimum χ^2 and MCMC along with varying SFH. The dispersion of $z_{\rm photo.}$ vs. $z_{\rm spec.}$ is $\delta z/(1+z) = 0.025$ for the photometric redshifts. Stellar masses in Nayyeri *et al.* (2017) are calculated as the median stellar mass reported by different SED fitting methods, with the redshift fixed to the photometric redshifts or spectroscopic when available.

4.3 Method

Galaxy Zoo uses a tree based structure for collecting information on morphological features. The CANDELS decision tree first asks the classifier to choose between the broad categories of smooth and rounded, feature or disc and star or artefact ($T00$ in Figure 4.1). If the classifier has indicated in the first task that the galaxy has features or a disc, then there are follow up questions about more complex features (inclination of the disc, presence of spiral patterns or clumps). In Figure 4.1 we show part of the Galaxy Zoo decision tree (Simmons *et al.* 2017), in particular the branches that lead to the classifications relevant for this work: spiral galaxies, clumpy spirals, smooth discs and edge-on discs.

Selecting a sample of galaxies can be done by choosing quantitative thresholds for different questions. However, for all the tasks below $T00$ in the tree, it is important to consider the responses to the task above it in this analysis. For a particular question, each possible answer has a vote-fraction f assigned to it, and the sum of the vote fraction of all possibles answers to one question adds to one; for example, if we consider $T00$, $f_{smooth} + f_{features} + f_{artifact} = 1$. To reduce the influence of less reliable classifiers, Simmons *et al.* (2017) apply a weighting method to obtain the final vote-fractions f.

After visually inspecting a subsample of galaxies, we choose the following thresholds to select the different types of discs.

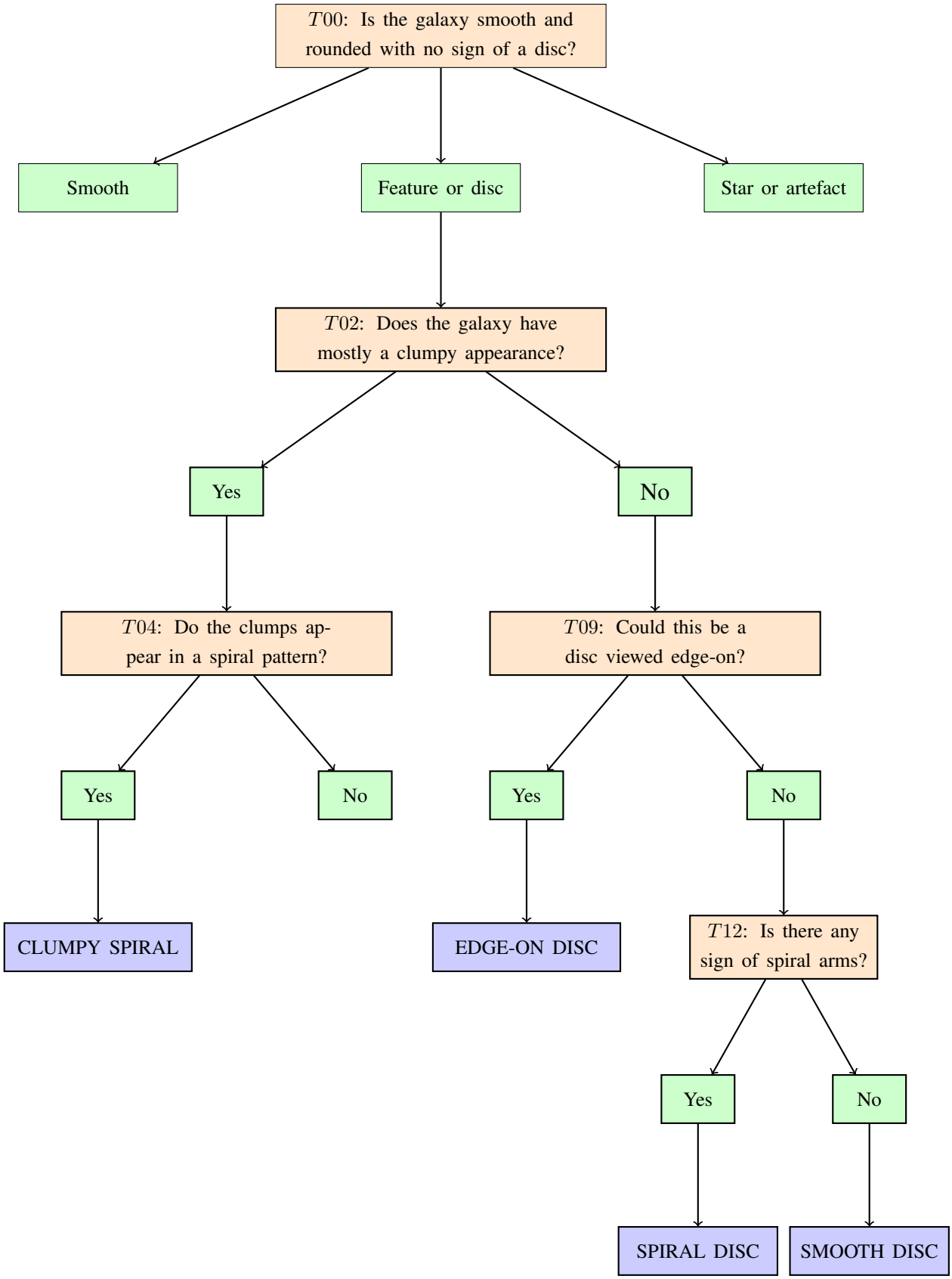


Figure 4.1: Simplified version of the decision tree of Galaxy Zoo CANDELS, which include the questions that leads to one of the classifications of interest for this work (blue boxes): spiral disc, clumpy spirals, smooth discs and edge-on discs.

• Spiral discs:

$$f_{features} > 0.3 \ \wedge \ f_{clumpy} < 0.5 \ \wedge \ f_{Edge-on} < 0.5 \ \wedge \ f_{Spiral-pattern} > 0.5.$$

• Clumpy spirals:

$$f_{features} > 0.3 \ \wedge \ f_{clumpy} > 0.5 \ \wedge \ f_{clumpy-spiral} > 0.5.$$

• Smooth discs:

$$f_{features} > 0.3 \ \wedge \ f_{clumpy} < 0.5 \ \wedge \ f_{Edge-on} < 0.5 \ \wedge \ f_{Spiral-pattern} < 0.5.$$

• Edge-on discs:

$$f_{features} > 0.3 \ \wedge \ f_{clumpy} < 0.5 \ \wedge \ f_{Edge-on} > 0.5.$$

We also require that $f_{artifact} < 0.3$ and that the number of classifiers in the final question for each disc type is at least 10. Finally, we limit our sample to galaxies with $\log M_* > 10$.

Simmons *et al.* (2017) discuss that some of the galaxies classified as smooth in the first question may be in fact discs without any distinctive feature, as visually it can be difficult to distinguish an elliptical galaxy from such types of smooth discs. Simmons *et al.* (2017) propose to select those smooth discs by looking at the relative bulge and disc strength, i.e. using a cut in the bulge to total fraction ($B/T < 0.5$) from a bulge to disc decomposition of the surface brightness. Bulge to disc decomposition has been performed within the UDS and COSMOS CANDELS fields (Häußler *et al.* 2013). By adding these smooth discs to the visually classified smooth discs we will have a more complete sample.

In Figure 4.2 we compare the smooth discs selected visually and by a cut in B/T. Visually smooth discs are larger in size and more compact (higher Sérsic index, n), and they have greater stellar masses.

In Figure 4.3 we compare the B/T of the smooth discs selected visually and by a cut in B/T. As expected, the majority of the visually classified smooth discs also have $B/T < 0.5$, although there is a small fraction (15%) that have $B/T > 0.5$. It is possible that these galaxies are a misclassification from elliptical galaxies.

For comparison to the spirals, in the next section we still use the visually classified smooth discs. However, the main results for the spirals and clumpy spirals remain the same even when including these smooth discs.

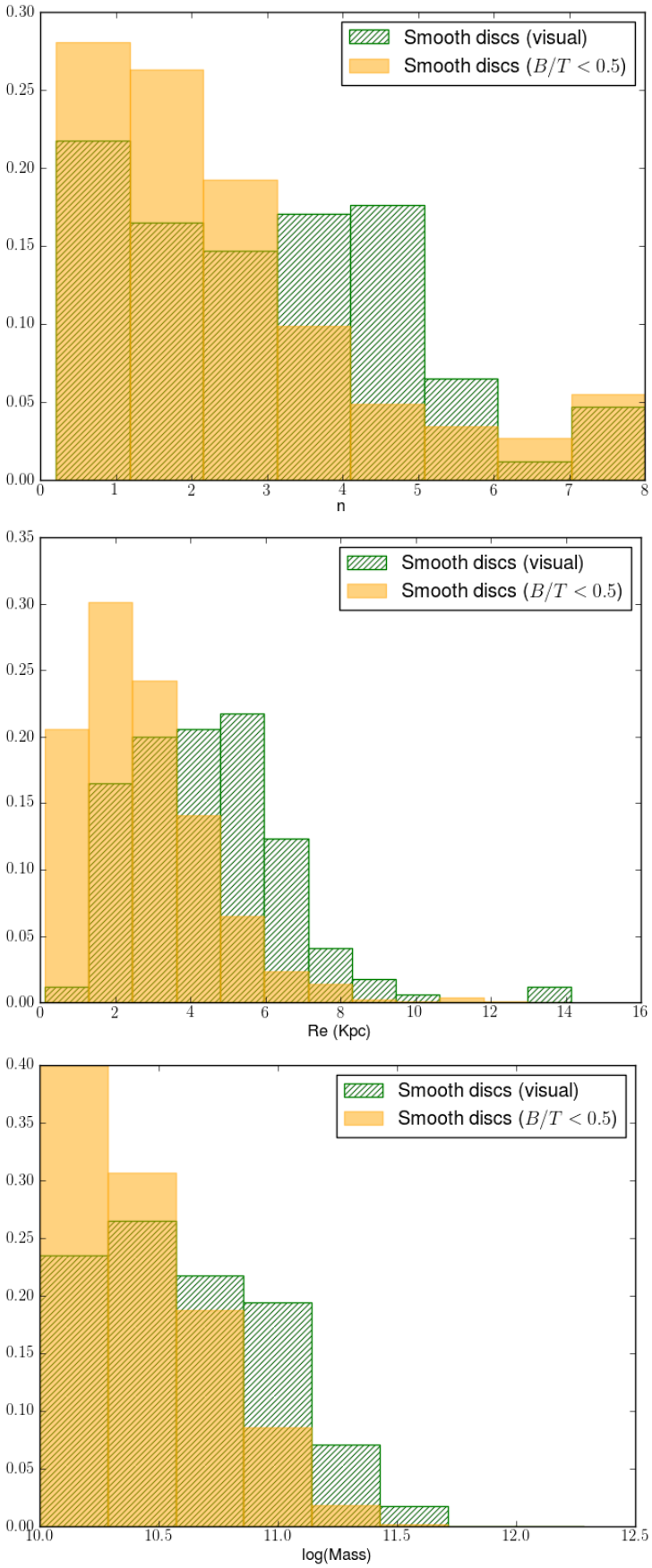


Figure 4.2: Comparison between smooth discs selected visually (strip lines green) and smooth galaxies with $B/T < 0.5$ (solid yellow). The top panels show the distribution of Sérsic index n and effective radius R_e. The bottom panel shows the distribution of stellar mass.

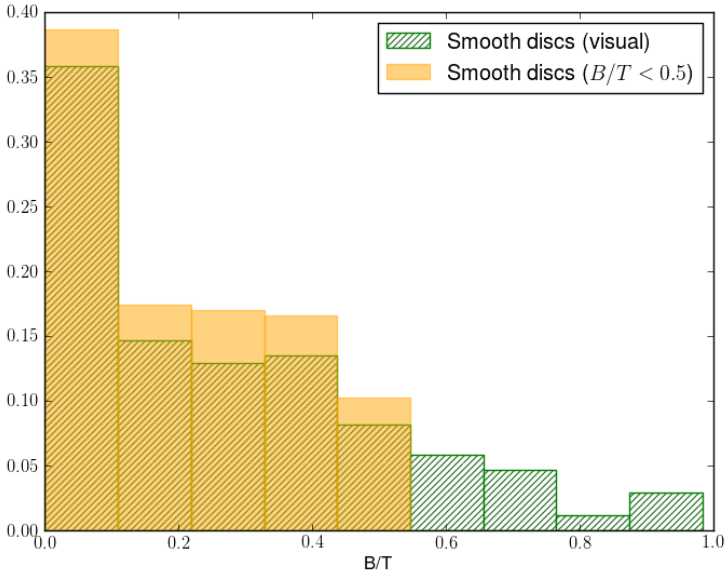


Figure 4.3: Distribution of B/T for smooth discs selected visually (strip lines green) and smooth galaxies with $B/T < 0.5$ (solid yellow).

4.4 Results

4.4.1 Fractions

We first investigate how the fractions of the different types of discs vary as a function of redshift, as shown in Figure 4.4. The fraction of galaxies classified as spiral discs increases with decreasing redshift. However this could be due to redshift effects, which may cause the spiral pattern to be more visible at lower redshifts. Galaxies classified as smooth discs (selected visually) and edge-on disc increase similarly with decreasing redshift, while the fraction of clumpy spirals increases at higher redshift.

To investigate to what extent the trends observed with redshift are due to redshift effects and not due to a real physical evolution, we have artificially redshifted all the galaxies at $z \sim 0.5$ from the UDS region to $z = 1$, and from $z \sim 1$ to higher redshifts ($z = 1.5, 2, 2.5$), using the Ferengi code from Barden, Jahnke & Häußler (2008), in the same way as in Chapter 2. We then simulate how we would observe galaxies if they were at a higher redshift. The procedure, as explained in Appendix A, modifies the angular size and the surface brightness (dimming) due to cosmological effects, and also takes into account the brightness increase of high-redshift objects. In Figure 4.5 we show some examples of galaxies classified as spirals at $z \sim 1$ and their simulated redshifted images at different redshifts. We then visually inspect this sample of galaxies and classify them as spirals (either 'normal' spirals or clumpy spirals) or non spirals at each redshift. In Figure 4.6

we show that the surface brightness of galaxies classified as spirals in the simulations at $z = 2.5$ (high redshift simulated galaxies, HRS) matches the real spirals observed at $z \sim 2.5$ (high redshift original galaxies, HRO), which indicates that our simulated spiral galaxies are comparable to the real spirals at high redshift.

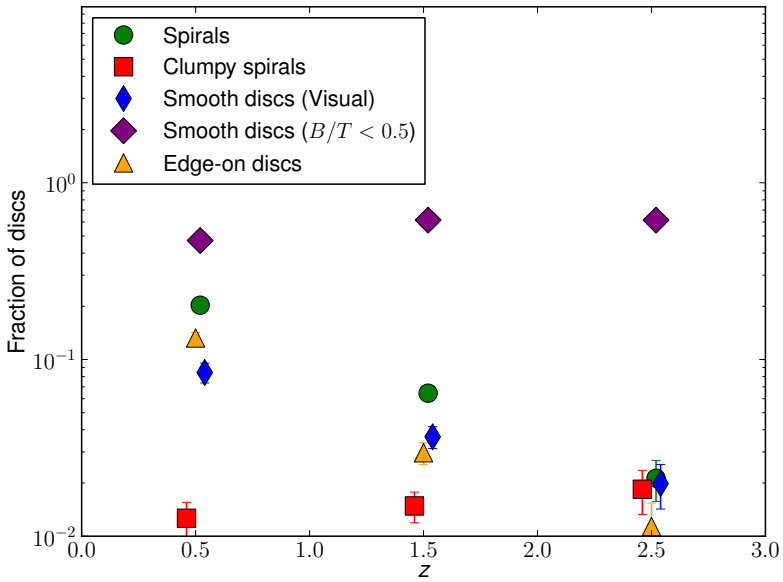


Figure 4.4: Fraction of different types of discs as a function of redshift. Green circles are spiral pattern discs, red squares are discs with a clumpy spiral structure, yellow triangles are edge-on discs, blue diamonds are discs with no spiral pattern and purple diamonds are smooth galaxies with $B/T < 0.5$.

In Figure 4.7 we show the fraction of spirals that is still classified as such in the simulations at different redshifts. It is clear that the ability to classify spirals decreases with increasing redshift and, in fact, it does so rapidly from $z = 1$ to higher z. It is thus possible that we are missing some spirals at high redshift because current instrumentation is not able to resolve spiral structures, meaning that some spirals may have been classified as smooth discs.

The observed evolution of the spiral fraction (Figure 4.4) is caused partially by redshift effects. In Figure 4.8, after taking into account these effects, we observe that there is an increase in the number of galaxies classified as spirals or clumpy spirals from $z = 1.5$ to $z = 0.5$. And at $z \sim 2.5$ there may be at least twice as many spiral galaxies than what we observe. In Figure 4.9 we show the evolution of the number densities for the different types of galaxies. Galaxies classified as either spirals or clumpy spirals increase in number density by a factor of 14 ± 2, from $z = 2.5$ to $z = 0.5$ with the majority of the increase happening from $z = 1.5$ to $z = 0.5$.

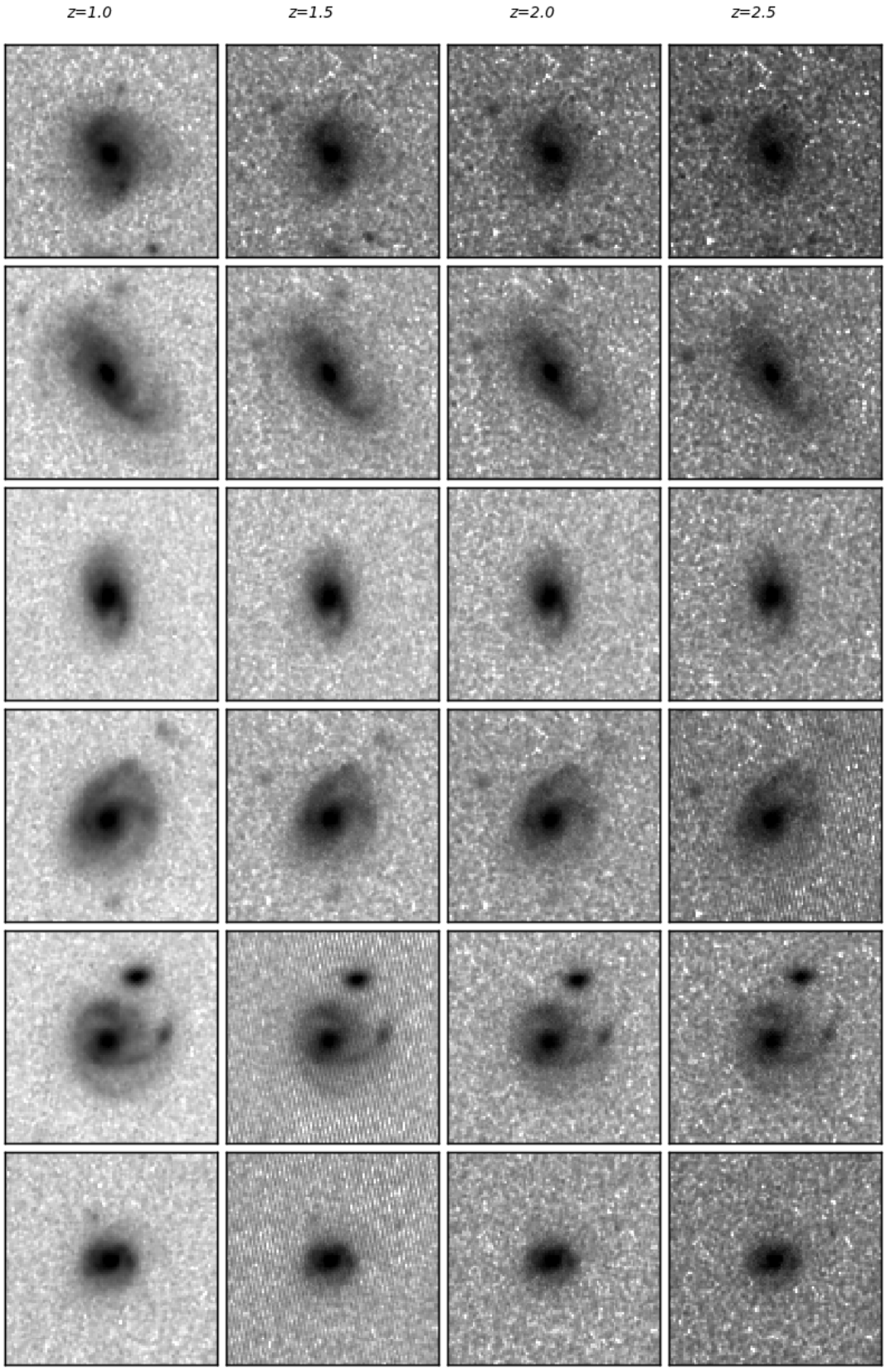


Figure 4.5: Redshifted spiral galaxies. Left panels show the original galaxies at redshift $z \sim 1$. The next panels show the galaxies after being artificially redshifted at $z = 1.5, 2, 2.5$, respectively.

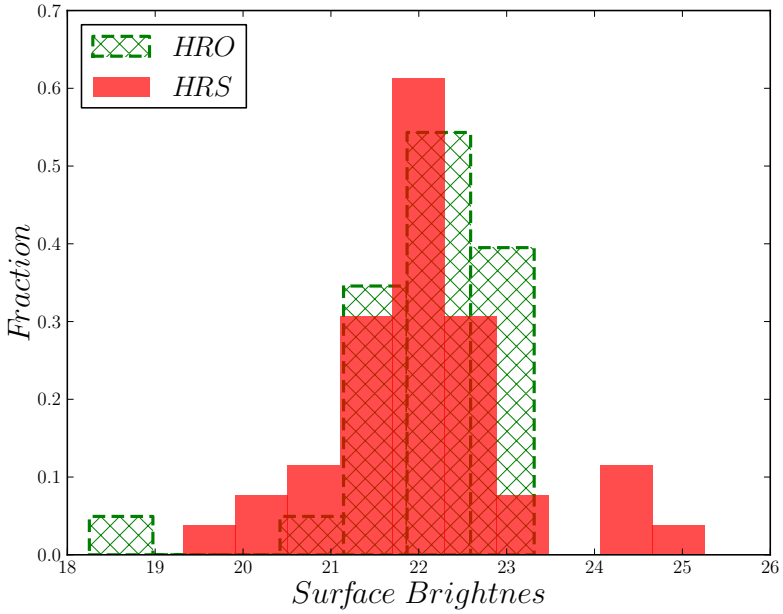


Figure 4.6: Surface brightness comparison between simulated galaxies at $z = 2.5$ classified as spirals (*HRS*), and observed spiral galaxies at $z \sim 2.5$ (*HRO*).

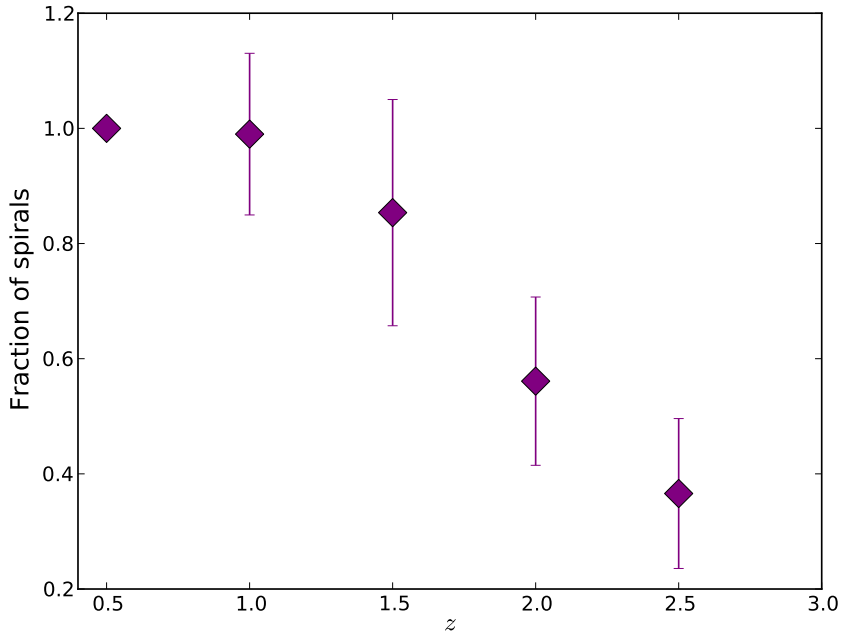


Figure 4.7: Fraction of recovered spiral galaxies. Fraction of spiral galaxies that, after being artificially redshifted at different redshifts, are still classified as spirals. We select the spiral galaxies at $z = 0.5$ and artificially redshifted them to $z = 1$, and calculate the fraction of these galaxies that still are classified as spirals. Then we select the spiral galaxies at $z = 1$ and after being artificially redshifted to $z = 1.5, 2, 2.5$, we calculate the fraction at each redshift that still shows spiral patterns.

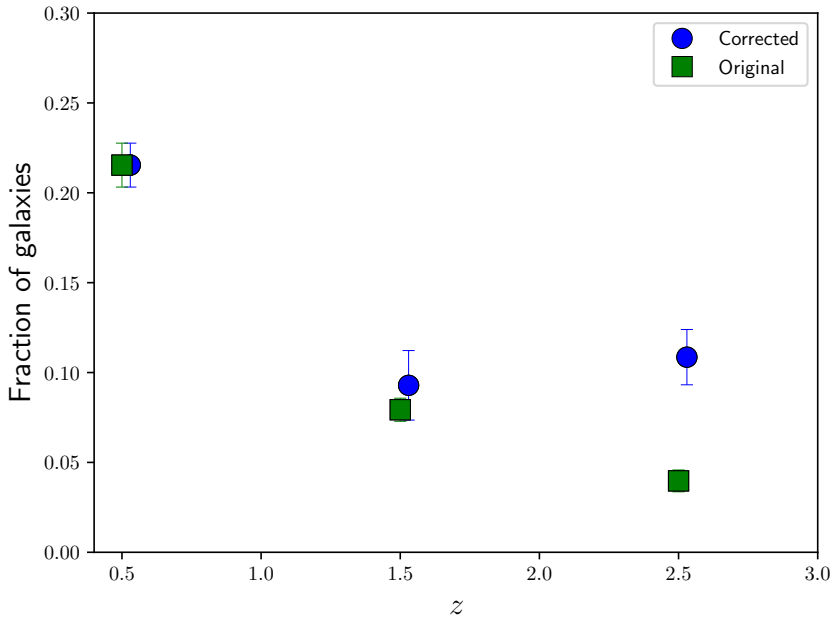


Figure 4.8: Fraction of spirals and clumpy spirals (blue circles) that changes after taking into account the redshift effects (green squares).

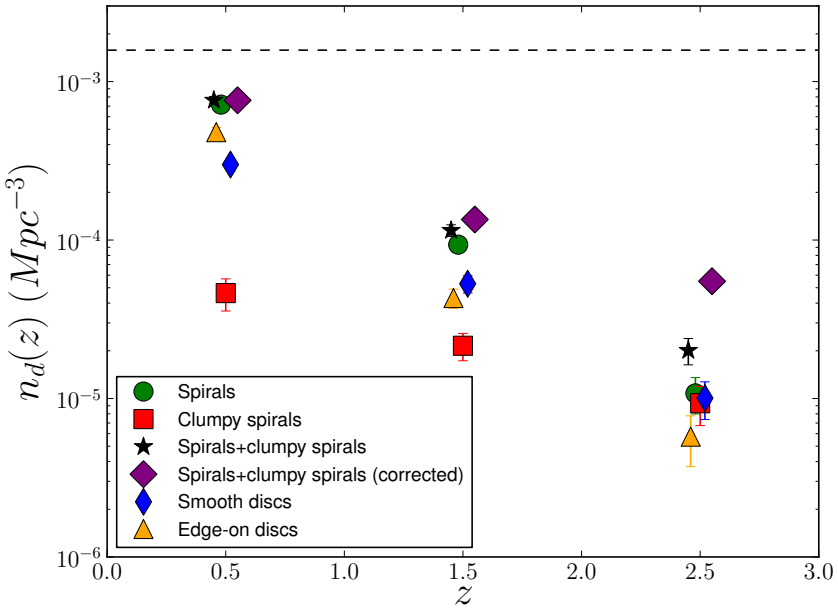


Figure 4.9: Number density evolution for different types of discs (for galaxies with $\log M_* > 10$). Green circles are spiral discs, red squares are discs with a clumpy spiral structure, yellow triangles are edge-on discs, blue diamonds are discs with no spiral pattern, black stars show spirals and clumpy spirals together, and purple diamonds show the number density of spirals and clumpy spirals after correcting for redshift effects. The dashed black line is the number density of disc-dominated galaxies in the local universe. It is inferred from the fitted Schechter function for disc-dominated galaxies done by Kelvin *et al.* (2014) in the GAMA survey.

In Figures 4.10 and 4.11 we show some of the galaxies at $2 < z < 3$ that are classified by Galaxy Zoo as spirals and clumpy spirals respectively.

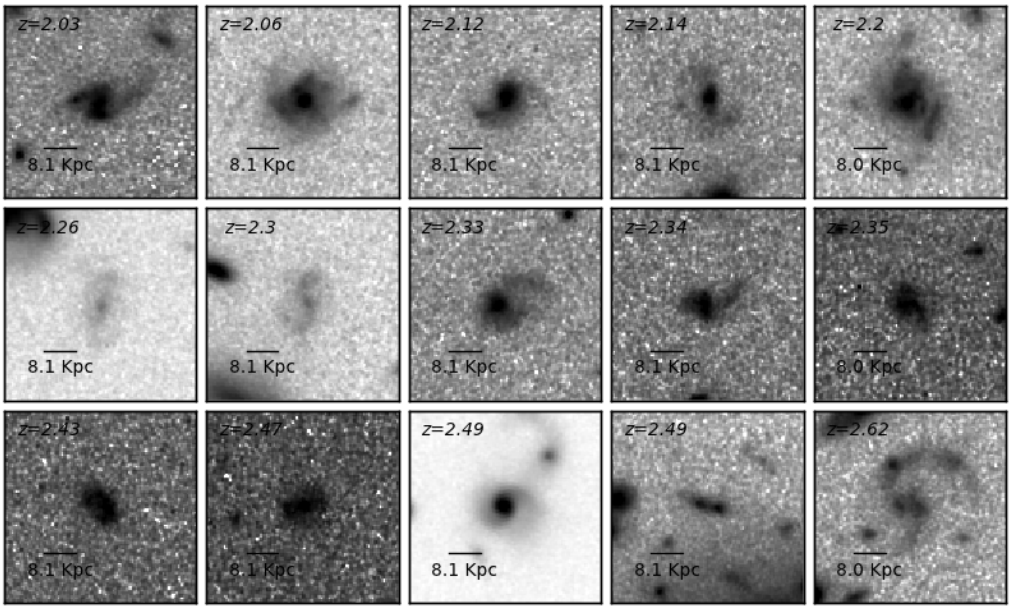


Figure 4.10: Examples of galaxies classified as spiral discs at $2 < z < 3$. The postage stamps are 6×6 arcseconds in size.

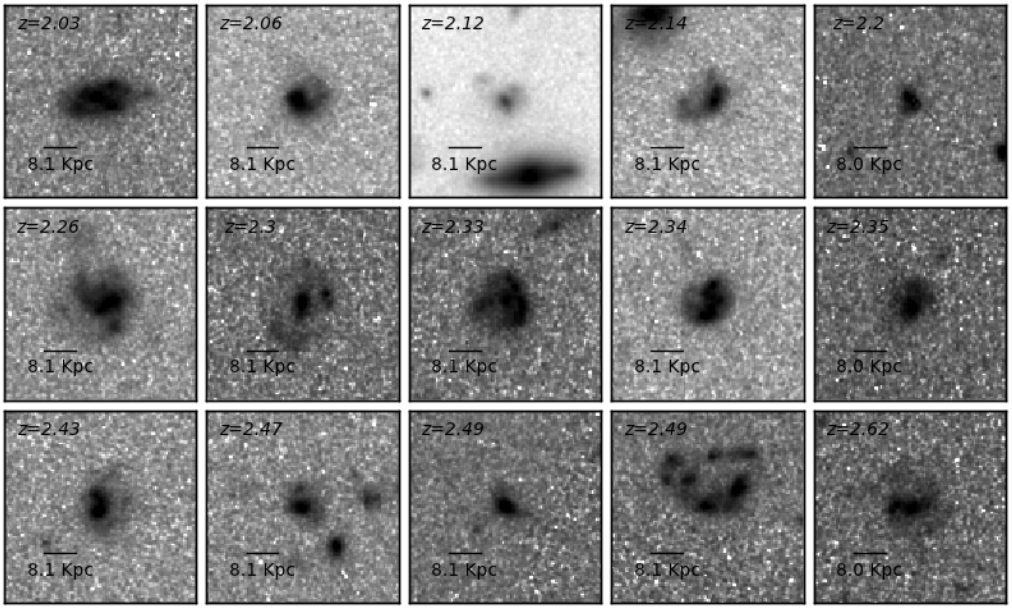


Figure 4.11: Examples of galaxies classified as clumpy spirals at $2 < z < 3$. The postage stamps are 6×6 arcseconds in size.

4.4.2 Stellar mass comparison

In Figure 4.12 we show the stellar mass of the different types of discs as a function of redshift. On average, the smooth discs visually classified have the highest stellar masses, however, this may be due to a bias selection (the smooth discs visually classified are the most massive among the smooth discs). In fact, the average stellar mass of the smooth discs classified according to their B/T is significantly lower. Taking that into consideration, the stellar masses of all kind of discs do not seem to differ much, on average, from each other.

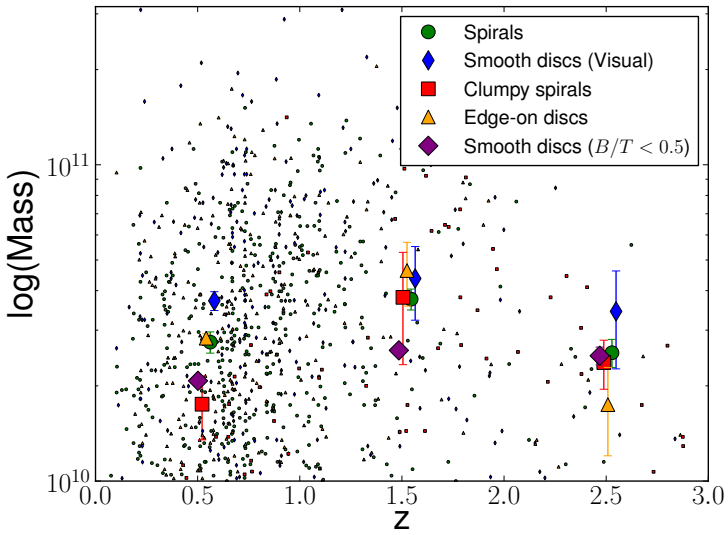


Figure 4.12: Stellar mass as a function of redshift for the different types of discs. Points are coloured as in Figure 4.4. Purple diamonds are the average stellar mass for smooth galaxies with $B/T < 0.5$.

4.4.3 *UVJ* diagram

Using the CANDELS photometry explained in Section 4.2 and the SMPY code (Duncan *et al.* 2014), we compute the rest-frame U, V and J Bessel magnitudes (see Chapter 3 for more details on the SED fitting templates). We use the rest-frame UVJ colours to divide our sample in to red/passive and blue/star-forming systems. As in Chapter 3, a galaxy is classified as red/passive if it satisfies the following criteria

$$\begin{cases} (U-V) > 1.3 \\ (V-J) > 1.6 \end{cases} \tag{4.1}$$

and the redshift dependent criteria

$$\begin{cases} (U-V) > 0.88 \times (V-J) + 0.69 & z < 0.5 \\ (U-V) > 0.88 \times (V-J) + 0.59 & 0.5 < z < 1.0 \\ (U-V) > 0.88 \times (V-J) + 0.49 & z > 1.0 \end{cases} \tag{4.2}$$

and blue/star-forming otherwise.

Figure 4.13 shows where our sample of galaxies lie in the UVJ diagram. The majority of the galaxies are in the star-forming region of the diagram. About $1/3$ of smooth discs and edge-one galaxies are in the passive region, but hardly any clumpy or spiral galaxies are found there. However, some of the galaxies classified as passive may be dusty star-forming galaxies. In Table 4.1 we summarize the fraction of passive and star-forming galaxies.

	Star-forming	Passive
Spiral discs	$92 \pm 5\%$	$8 \pm 1\%$
Clumpy spirals	$97 \pm 13\%$	$3 \pm 2\%$
Smooth discs	$65 \pm 6\%$	$35 \pm 2\%$
Edge-on discs	$63 \pm 5\%$	$37 \pm 4\%$

Table 4.1: Fraction of galaxies with different disc classifications that are passive and star forming at all redshifts, according to the UVJ selection from equation (4.2).

We study the rest-frame colour $U-V$ as a function of redshift in Figure 4.14, which shows that spiral discs and clumpy spirals are bluer, and smooth discs and edge-on galaxies become redder than spiral galaxies by $z \sim 0.5$.

4.4.4 Structure

To study the structural parameters of the three Galaxy Zoo CANDLES fields, we utilize the Sérsic indices and effective radius measured by van der Wel *et al.* (2012), in which the structural parameters are obtained from the H-band CANDELS image using GALFIT (Peng *et al.* 2002). Figure 4.15 (top panel) shows that the Sérsic index of spiral discs and clumpy spirals is lower at all redshifts than for smooth discs (this is still the case when including the smooth discs as selected by $B/T < 0.5$). The spiral discs and clumpy spirals have on average $n < 2.5$ although there is a slight increase in n with decreasing

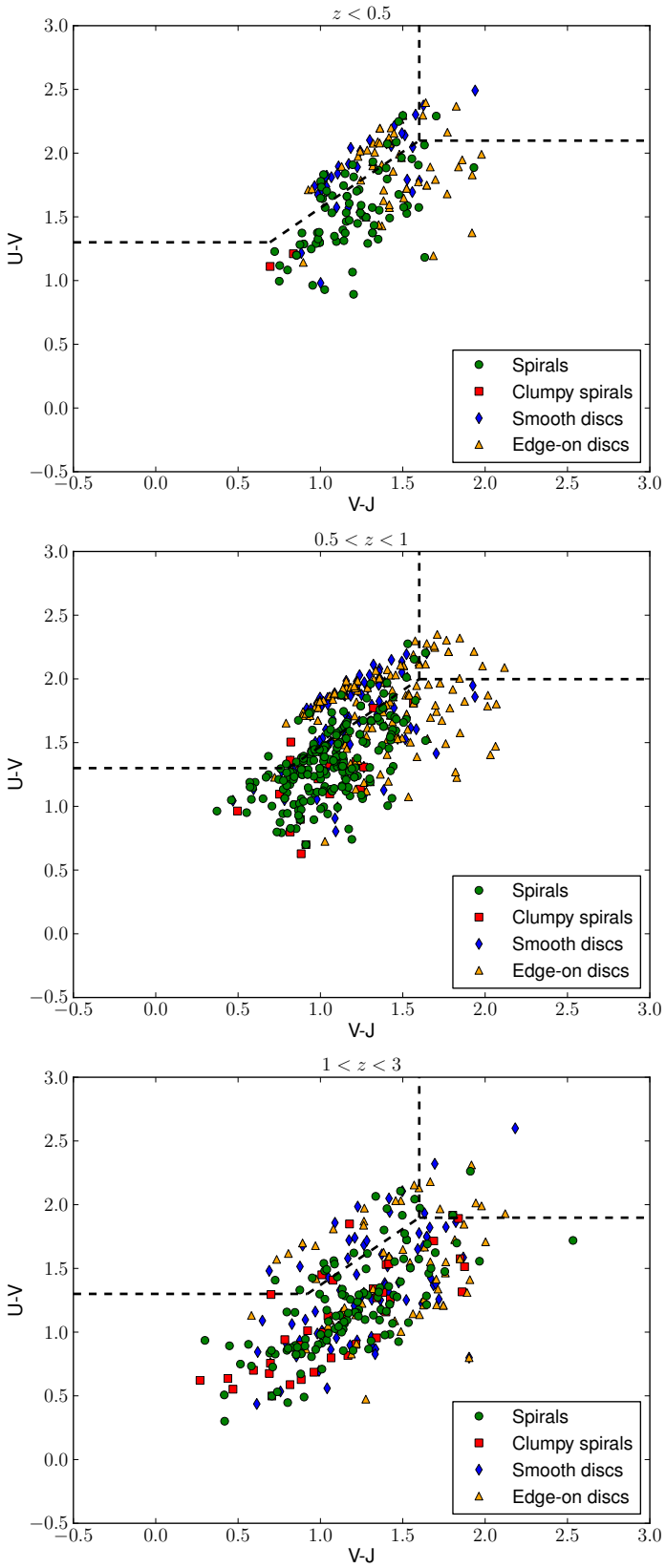


Figure 4.13: Rest-frame $U - V$ versus $V - J$ diagram in redshif bins. The top panel shows galaxies at $z < 0.5$, the middle one galaxies at $0.5 < z < 1$, and the bottom panel at $z > 1$. Green circles shows spiral discs; red squares, clumpy spirals; blue diamonds, smooth discs and yellow triangles, edge-on discs. The black dashed line shows the separation between passive and star-forming galaxies according to equation (4.2).

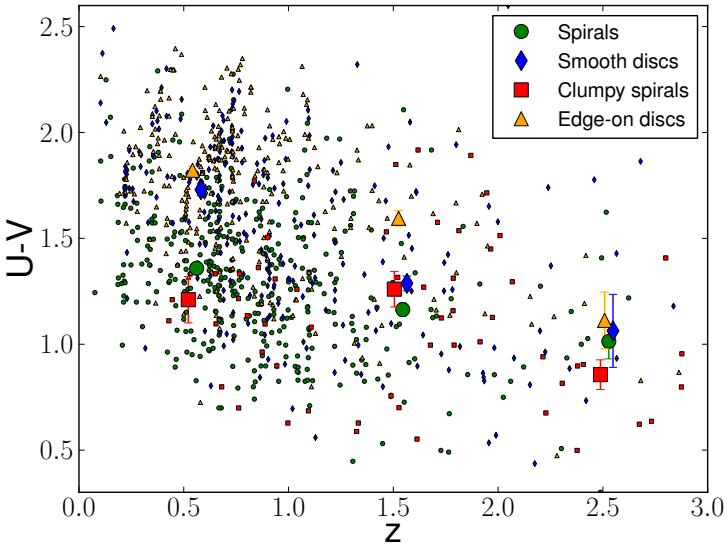


Figure 4.14: Rest-frame $U - V$ as a function of redshift. The points are coloured as in Figure 4.13.

redshift. The Sérsic index of the smooth discs also increases at lower redshift and by $z = 0.5$ they have on average $n > 2.5$ ($n > 2$ when including also the smooth discs selected by $B/T < 0.5$).

The effective radius does not change significantly over cosmic time (bottom panel of Figure 4.15). All types of disc have on average similar sizes (although if we include the smooth discs selected by $B/T < 0.5$, then the smooth discs are smaller than spiral objects at all redshifts). However, it is established that galaxies grow in size with decreasing redshift, the absence of size evolution observed here is probably due to redshift selection effects, as at high redshift, the spirals classified by visual inspection will most likely be the biggest, while the spiral pattern of smaller galaxies may not be distinguishable at high redshift.

The analysis of the concentrations C, asymmetries A and clumpiness S is also useful to investigate the structure of galaxies. Those parameters, known as CAS parameters, are computed in Mortlock *et al.* (2015) using the H-band image in the CANDELS UDS field.

The **asymmetry** is found by subtracting a 180 degrees rotated image from its centre of the galaxy to the original image plus a background subtraction:

$$A = \min\left(\frac{\sum |I_0 - I_{180}|}{\sum I_0}\right) - \min\left(\frac{\sum |B_0 - B_{180}|}{\sum I_0}\right), \tag{4.3}$$

where I_0 is the original image and I_{180} is the image after rotating it 180 degrees. B_0 is the original background image and B_{180} is the background image rotated it 180 degrees. The sum is performed over all the pixels within a matching region of the original and rotated

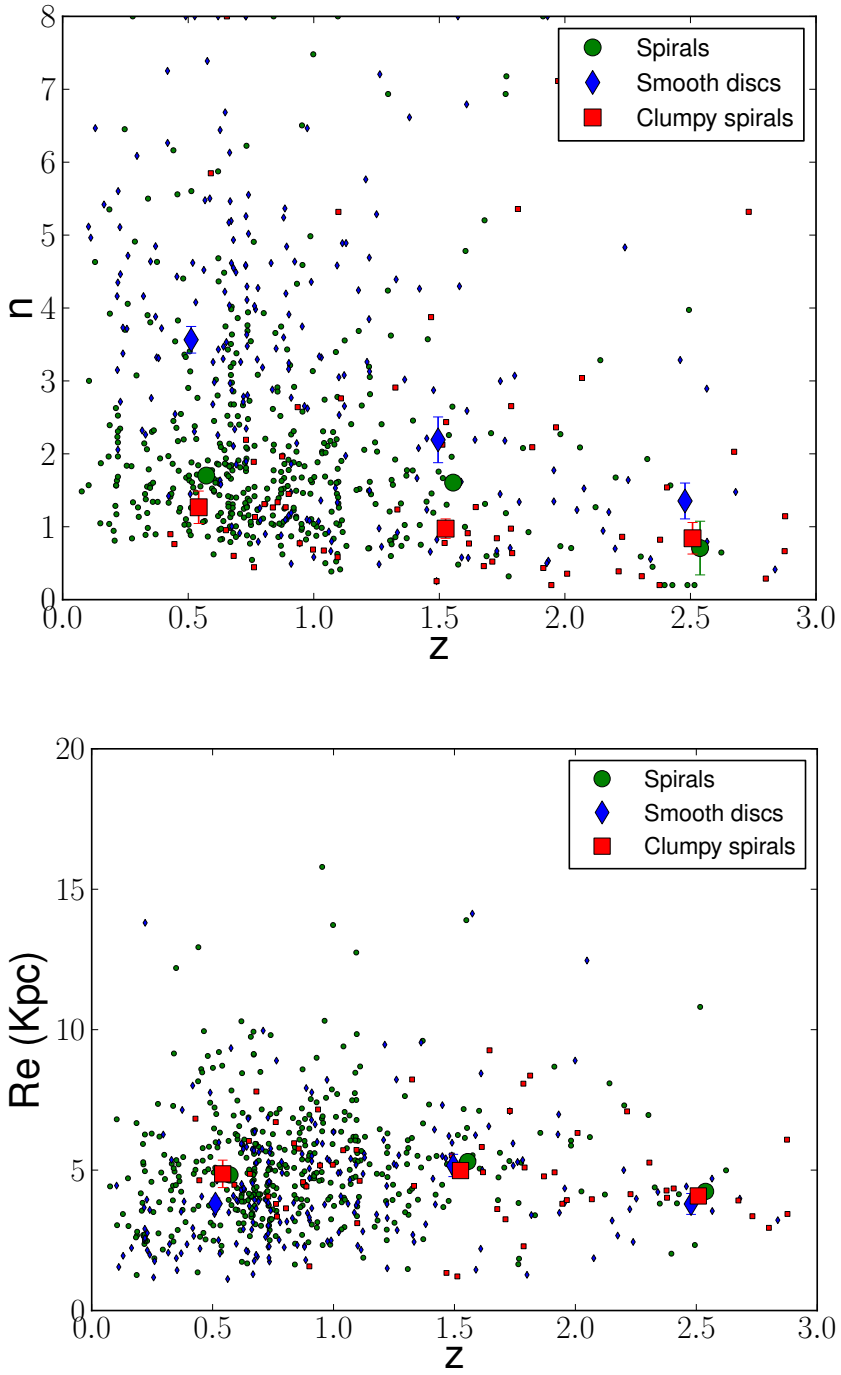


Figure 4.15: Evolution of the structural parameters, Sérsic index and effective radius, for the different types of discs. Points are coloured as in Figure 4.13. The big symbols are the median values at different redshift bins, and the error bars are the error on the median values. Note that we do not show the edge-on discs, as the Sérsic index and effective radius will not describe them accurately.

images. The minimization on each term is done to locate the centre of the galaxy that minimize the asymmetry.

The **concentration** parameter measures how concentrated the light is in a central region compared to a larger, less concentrated region. It strongly correlates with the Sérsic index

n, which is also a measure of the light concentration in a galaxy:

$$C = 5 \times \log \frac{r_{80}}{r_{20}}, \tag{4.4}$$

where r_{80} and r_{20} are the radii containing 80% and 20% of the galaxy's total light respectively (Bershady, Jangren & Conselice 2000). Elliptical galaxies are the most concentrated systems and the concentration of stellar light decreases for later Hubble types (Bershady, Jangren & Conselice 2000). The quantitative values of C range roughly from 2 to 5 with most systems having $C > 4$ being ellipticals, while disc galaxies have values between 3 and 4. The lowest values correspond to objects with low central surface brightness and low internal velocity dispersion (Graham, Trujillo & Caon 2001; Conselice, Gallagher & Wyse 2002).

The **clumpiness** (or smoothness) describes the fraction of light in a galaxy that is contained in clumpy distributions. It is measured as follow:

$$S = 10 \times \sum \frac{(I_0 - I_0^\sigma) - B_0}{I_0}, \tag{4.5}$$

where I_0^σ is the original image after reducing the resolution by a smoothing filter (Bershady, Jangren & Conselice 2000; Conselice *et al.* 2003). The sum is performed over the whole pixels of the image.

The clumpiness parameter S correlates with the star formation activity, as star-forming galaxies tend to have clumpy structures and, thus, high values of S.

In Figure 4.16 we show the evolution of the CAS parameters for the different types of discs. Clumpy spirals have the highest asymmetry indices A, although spiral discs also have very high A at the highest redshifts. Smooth discs have slightly lower asymmetry values. However, they have the highest values of concentration indices C. Overall the concentration increases with decreasing redshift. The clumpiness decreases with decreasing redshift for all types of discs.

We study the relation between CAS parameters in Figure 4.17 (relation between clumpiness and asymmetry) and Figure 4.18 (relation between asymmetry and concentration). The CAS parameters can be used to determine morphological types of galaxies. In Figure 4.18 the blue and red lines classify galaxies into late types (above the red line), intermediate types (between the red and blue lines), and early types (below the blue line). We find

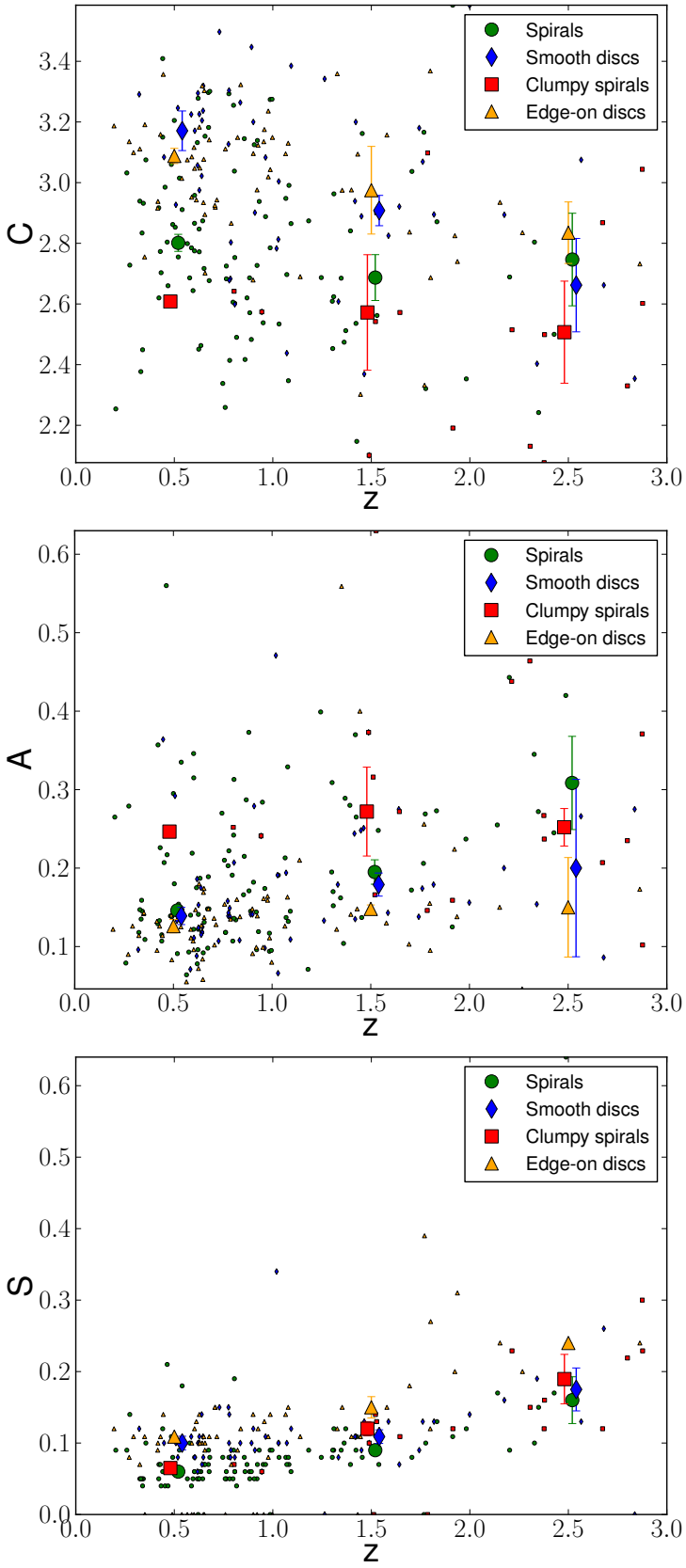


Figure 4.16: Evolution of the concentration C (top), asymmetry A (middle) and clumpiness S (bottom) for our sample of disc galaxies. Points are coloured as in Figure 4.13. The big symbols are the median values at different redshift bins.

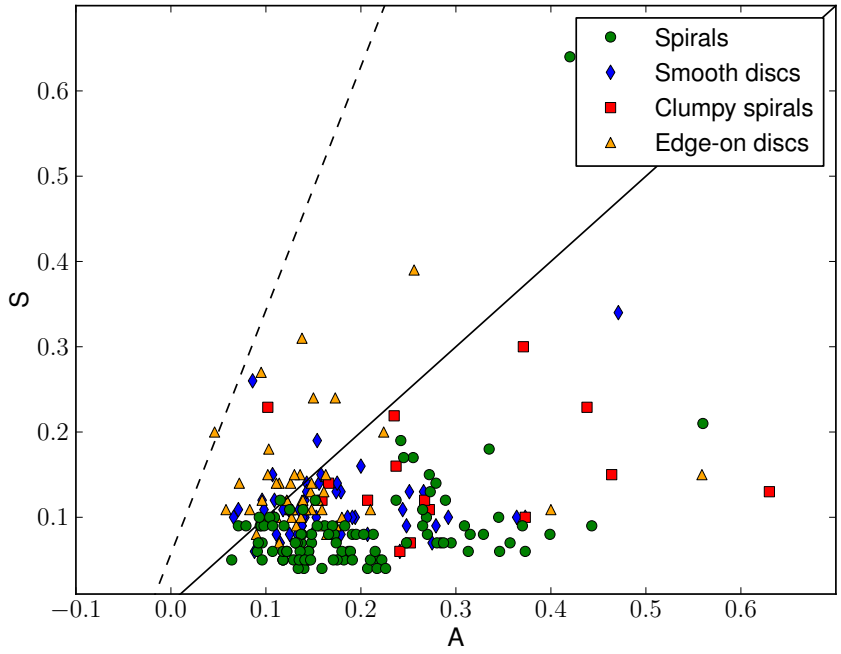


Figure 4.17: Asymmetry (A) versus clumpiness (S). The dotted line represents the relationship between A and S found for the normal Frei galaxies in Conselice (2003). Points are coloured as in Figure 4.13.

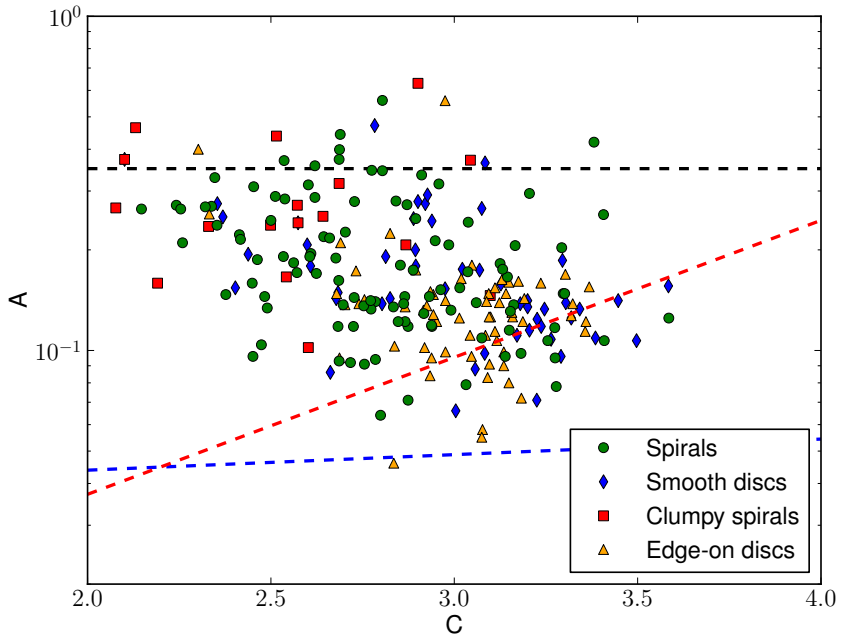


Figure 4.18: Concentration (C) versus asymmetry (A). The blue and red dotted lines are the cuts derived from local galaxies from Bershady, Jangren & Conselice (2000). The blue line separates early and intermediate types and the red line, intermediate and late types. Galaxies above the black line ($A > 0.35$) are considered to be mergers. Points are coloured as in Figure 4.13.

that according to this selection the majority of spirals and clumpy spirals are late type, with some galaxies above the black line ($A > 0.35$) which indicates that they are likely to be mergers (Conselice, Chapman & Windhorst 2003).

4.4.5 Star formation activity

SFRs are calculated using the photometry from CANDELS explained in Section 4.2 and using the same method as in Chapter 3 (by applying the Kennicutt (1998) conversion from the rest-frame UV luminosity to SFR, and then correcting for dust using the UV slope).

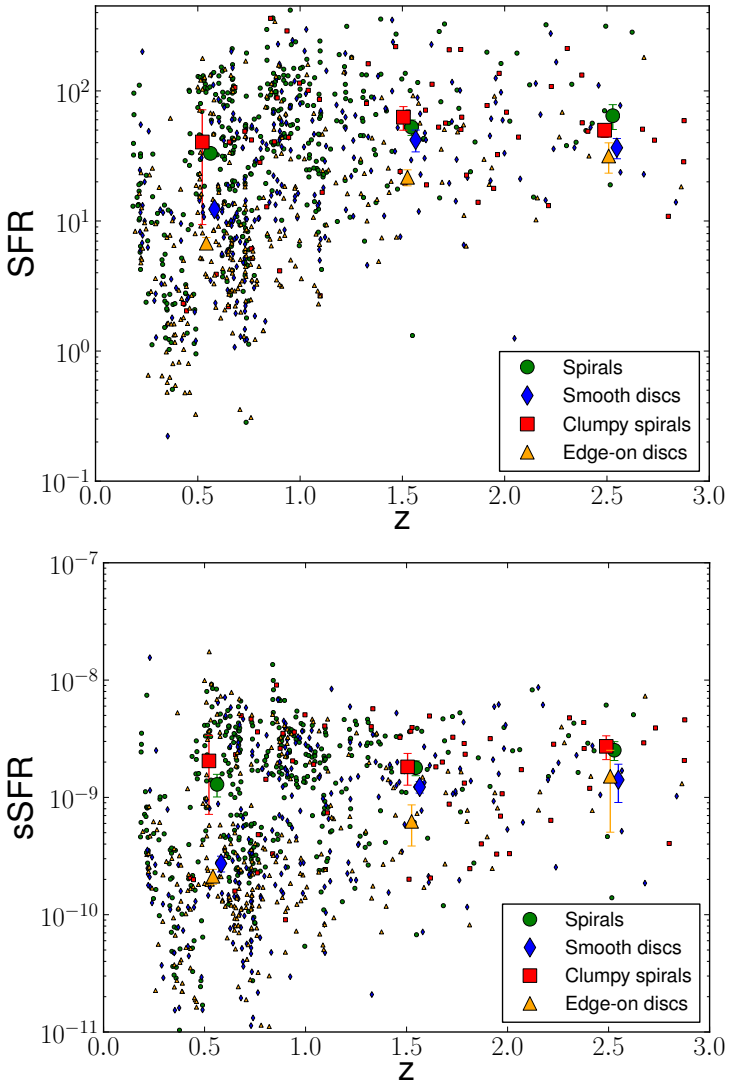


Figure 4.19: SFR and sSFR (in log scale) as a function of redshift for the different types of discs. Points are coloured as in Figure 4.13. The big symbols are the median values at different redshift bins, and the error bars show the error on the median values.

From Figure 4.19 we observe that the spirals and clumpy spirals have the highest SFRs and sSFRs at all redshifts. The median value of SFR for these galaxies remains mostly constant with redshift at about $SFR = 40 \pm 3\ M_{\odot}\mathrm{yr}^{-1}$ for spirals and $SFR = 50 \pm 7\ M_{\odot}\mathrm{yr}^{-1}$ for clumpy spirals. At $z > 1.5$ the SFR of smooth discs is as high as for the spirals, however this could be caused by that fact that some of these galaxies could be

spirals but, due to redshift resolution effects, they are classified as smooth discs. The average SFR for smooth discs is $SFR = 19 \pm 43\ M_{\odot}\mathrm{yr}^{-1}$.

A main-sequence of star-forming galaxies is observed at $z < 1.5$ (top panel of Figure 4.20), and it appears to be formed mostly by spirals and clumpy spirals, and low mass smooth discs. At $z > 1.5$ the majority of the disc galaxies are consistent with the main-sequence of star-forming galaxies (bottom panel of Figure 4.20). Clumpy spirals have the highest SFR at all masses. High mass spirals have lower SFR at lower redshifts, although they are still more star forming than smooth discs.

We notice that edge-on discs have the lowest SFRs. However, this is probably an underestimation in the SFR due to dust, which makes particularly difficult to obtain reliable SFRs in these edge-on galaxies.

4.5 Conclusions

We have used the CANDELS Galaxy Zoo classification to look for spirals at different redshifts in the UDS, GOODS-S and COSMOS fields. Within this classification scheme, spirals have been visually classified up to redshift $z \sim 2.5$. It is however possible that some spiral galaxies at $z > 2$ are instead misclassified as smooth discs due to redshift effects, as lower resolution at high redshift causes the spiral pattern to blend with the rest of the galaxy. In terms of number densities, spirals increase by a factor of 14 ± 2 from the highest redshifts to the lowest, after correcting for redshift effects. The greatest increase occurs at $z \sim 1.5$.

Spirals and clumpy spirals have low Sérsic index at all redshifts ($n < 2.5$), which indicates a flatter surface brightness profile, linked with disky morphologies. Smooth discs (without spiral arms) become more compact (with higher Sérsic index) as redshift decreases. On average both have similar sizes that do not seem to evolve with redshift. This however could be the result of redshift effects. Spiral patterns are more visible in larger galaxies and, therefore, at the highest redshifts the galaxies classified as spirals may be the largest in size. The difference in structure between spirals and smooth discs is also observed in the CAS parameters. Spirals and clumpy spirals have lower concentration parameters than smooth discs, which may be an indication that smooth discs are more evolved. Spirals and clumpy spirals have higher asymmetry values. In particular, clumpy

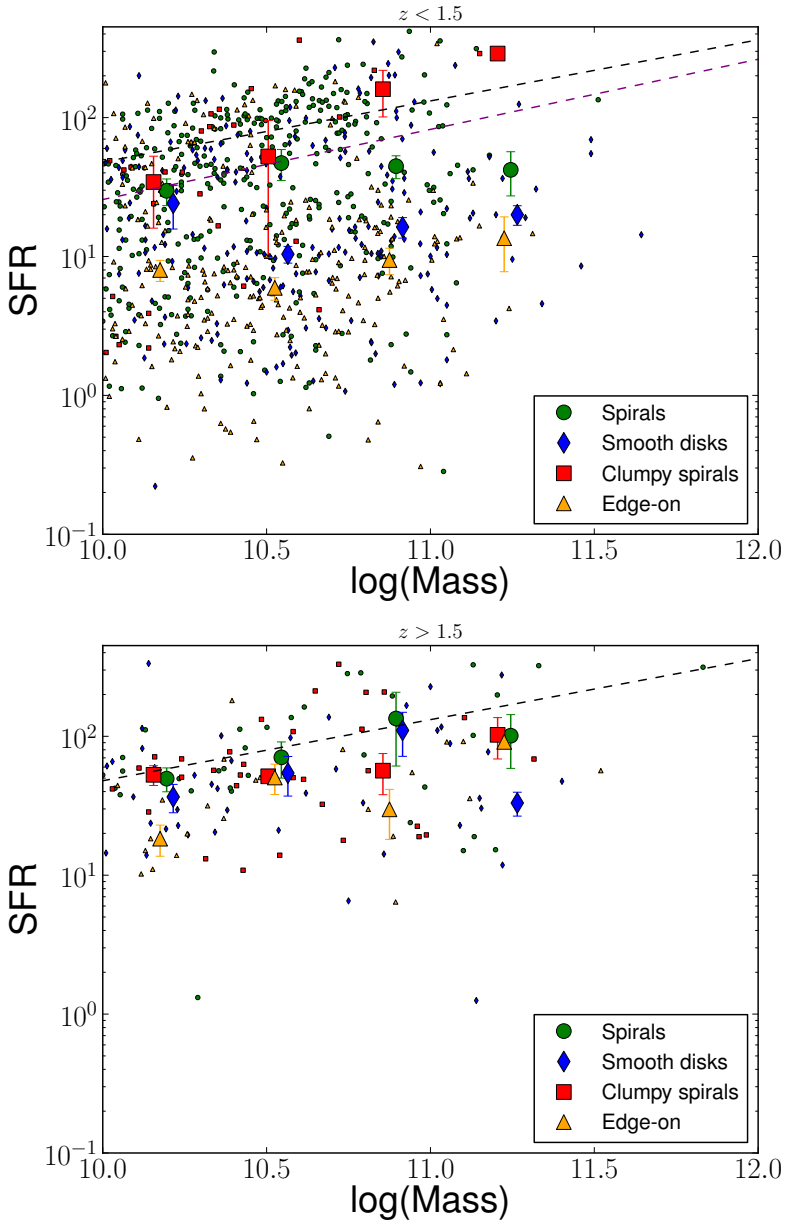


Figure 4.20: SFR (in log scale) as a function of stellar mass for the different types of discs. The top panel shows galaxies at $z < 1.5$ and the bottom panel at $z > 1.5$. Points are coloured as in Figure 4.13. The big symbols are the median values at different stellar mass bins, and the error bars show the error on the median values. The dashed black line and purple line are the SFR-mass relation at $z = 2$ and $z = 1.5$, respectively, found by Whitaker *et al.* (2012).

spirals have on average the highest asymmetries and remain constant with redshift, while the asymmetry for spirals and smooth discs tend to be lower with decreasing redshift. The high values of asymmetry at high redshift can be explained on one hand by the more clumpy and irregular morphologies of spirals as opposed to those in the local Universe, and, on the other hand because, as redshift decreases, spirals become more symmetric and less clumpy. The trends found for the concentration and asymmetry (Figure 4.16) are

consistent with Bluck *et al.* (2012), that report a rise of asymmetry with redshift while the concentration decreases.

The SFR of spirals and clumpy spirals is the highest at all redshifts among discs galaxies, and does not change significantly with redshift. Yet, there is a decrease in the star formation of spirals with redshift for the most massive galaxies ($\log M_* > 11$). This trend with mass is also observed for the smooth discs. Massive galaxies shut down their star formation before lower mass galaxies for smooth discs and spiral galaxies. This is not the case however for clumpy spirals, that have the highest SFR at all masses. At high redshift ($z > 1.5$) the main-sequence of star-forming galaxies is formed by all types of discs, while at lower redshift it is formed mostly by spirals and clumpy spirals. This is in agreement with the position these galaxies occupy in the UVJ diagram. Spirals and clumpy spirals lie in the star-forming region of the diagram at all redshifts. Smooth discs are preferentially in the star-forming region as well, but about 32% of these galaxies are in the passive region, especially at $z < 1$.

Although it could be expected that spirals and clumpy spirals have the highest stellar masses, we find that on average all kind of discs have similar stellar masses. Therefore, there is no benefit of having a large mass to produce spiral structure.

Chapter 5

Summary and future work

Bulges and discs

One of the main goals of this thesis is to investigate the formation and evolution of discs and bulges. To that end we have studied massive galaxies ($\log M_* > 10$) in the epoch when most of the morphological transformation in galaxies happens ($1 < z < 3$), and when galaxies start transitioning into Hubble types (Mortlock *et al.* 2015). To study the bulge and disc components we have performed bulge to disc decomposition at different wavelengths, which allow us to study in detail the properties of these components separately. In Chapter 2 we find that the 2-component systems (with a bulge and a disc) form during this epoch ($1 < z < 3$), and start to dominate in terms of number density. Furthermore,the most massive galaxies are the ones that will become these 2-component systems at lower redshifts. Galaxies with relatively lower mass appear to remain 1-component systems (either disk-like or spheroid-like galaxies).

In Chapters 2 and 3 we find evidence that supports the idea that these galaxies form inside-out, with the bulge being in place earlier and the disc growing in size around it, possibly due to mass accretion. This process increases the size of the disc at the same time as it induces star formation in these outer parts of the galaxy.

In Chapter 3 we show that bulges and discs must have different SFHs, with bulges being consistent with a single star formation burst at $z = 2.5$, while discs show evidence of a more continuous star formation activity. We find that the majority of discs in the 2-component galaxies lie in the star-forming region of the UVJ diagram. A higher fraction

of bulges are in the passive region, but still around $^2/_3$ are in the star-forming region. However, some of the star-forming bulges lie in the dusty region of the diagram which indicates that they may be red due to dust instead of being passive. Overall, the fraction of the 2-component galaxies that lie in the star-forming region of the diagram is similar to that of the 1-component disc-like galaxies. This may be an indication of a similar SFH for these disc-dominated galaxies, and different to the spheroid-like ones.

The majority of star formation within these galaxies is occurring in the disc. Although at $z > 2$ bulges are as star forming as discs (with both SFR and sSFR as high as discs), the disc components become more star forming in comparison to the bulges as redshift decreases. This difference is mostly due to bulges becoming redder at lower redshift. This is also observed in the spheroid-like population: at $z > 2.5$ the majority of spheroids are blue, but as redshift decreases, the number of red spheroid rapidly increases.

We observe that stellar mass plays an important role in the formation of galaxies. In Chapter 3 we show that the most massive ($\log M_* > 11$) bulges, discs and 1-component systems established their final colours earlier in the Universe than lower mass systems. They are already the reddest objects at the highest redshifts, and remain red and passive. Finally, we find that the formation of a central inner component likely triggers the formation of the central massive black holes in 2-component galaxies.

Spiral galaxies

Another main goal of this thesis is to study the role of spiral features in the properties of discs and, in particular, at high redshift. In Chapter 4 we study the differences between spiral galaxies (either 'normal' spirals or clumpy spirals) and discs that show no signs of spiral features (smooth discs). We show that these two types of galaxies show different morphological properties in terms of Sérsic index and CAS parameters. Spiral galaxies have lower Sérsic index and lower concentrations than smooth discs. This suggests that smooth discs may be more evolved than spirals. Spiral galaxies have higher asymmetry values than smooth discs, however their values decrease at lower redshift. This highlights that at high redshift spirals have more clumpy and irregular morphologies and, as redshift decreases, they become more symmetric and less clumpy.

In Chapter 4 we find a connection between the spiral structure and star formation activity, with spiral galaxies being more star forming than smooth discs at any given mass. In particular, the most star-forming objects at all redshifts and stellar masses are the clumpy spiral galaxies, with an average SFR of $SFR = 50 \pm 7\ M_{\odot}\mathrm{yr}^{-1}$. However, we also observe a decrease in SFR with redshift for the most massive spirals ($\log M_* > 11$), while lower mass spirals at $z < 1.5$ have similar SFR than equal mass spirals at $z > 1.5$.

Future Work

To advance in this field and understand the formation of bulges and discs we need high resolution data at higher redshifts ($z > 3$). Higher resolution will allow us to better discern the redshift effects observed in this thesis, and also to probe the first epoch of disc and bulge formation within the Universe. This would be possible thanks to space based telescopes, such as the James Webb Space Telescope (JWST), or the use of Adaptive Optics (AO) in the next generation of ground telescopes, like the E-ELT.

A different approach would be taking advantage of Integral Field Units (IFUs). Thanks to IFUs and AO on large ground based telescopes it is possible to observe the kinematics of galaxies at high redshift on large samples of galaxies. Studying the kinematics of the different types of galaxies (e.g., spirals galaxies and smooth discs) will give further insight into how structurally distinct these galaxies are.

Appendix A

Simulations of high redshift galaxies

A.1 Details of the simulations

Many of the results presented in Chapter 2 originate from some mixture of redshift effects as well as real changes to the 1- and 2-dimensional structure of massive galaxies. It is important to separate these two effects to determine the real evolution of galaxies. As such, we artificially simulate redshifted galaxies using the Ferengi code from Barden, Jahnke & Häußler (2008). From our whole galaxy sample, we take a subsample of 357 objects with redshifts $z < 1.4$ that we denote LRO (low-redshift original galaxies). For those LRO galaxies, we create new images of how we would observe the same galaxies if they were at redshift $z = 2.75$ in the same CANDELS field, to determine the maximal effects of redshift. We denote this new sample HRS (high-redshift simulated galaxies). This procedure modifies the angular size and the surface brightness (dimming) due to cosmological effects, but also takes into account the brightness increase of high-redshift objects. We now compare the structures of the HRS galaxies with their corresponding LRO ones, as well as with the actual galaxies we examine in the main work of Chapter 2 in the redshift range of $2.5 < z < 3$, that we denote HRO (high-redshift original galaxies).

To demonstrate that our simulated galaxies are a fair comparison to the actual high redshift galaxies we first compare the surface brightness distribution for both samples. In Figure A.1 we show the surface brightness of the HRS sample compared with the HRO sample,

which shows that there is a good overlap between the two and therefore that, at least in the respect of magnitude and size distributions, these two samples can be compared.

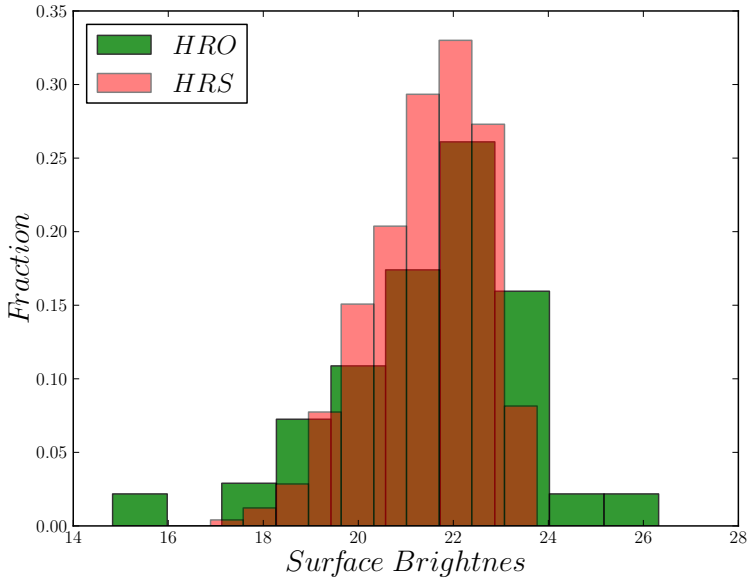


Figure A.1: Comparison of the surface brightness of the HRS (high-redshift simulated) galaxies (red) with the HRO (high-redshift original) galaxies at redshift $2.5 < z < 3$ (green).

A.2 Results

Once we have our simulated subsample of HRS galaxies we apply the same method described through Chapter 2 to determine whether each galaxy should be classified as 1- or 2-component system. The process for this can be summarized as:

- We fit the surface brightness with a Sérsic function with a free n for a 1-component fit.
- We fit the surface brightness with a Sérsic + Exponential function as a 2-component fit.
- We use our three methods to classify the galaxies as 1- or 2-components: the visual classification, F-test and RFF method.

A comparison of Sérsic index n, magnitude Mag and effective radii R_e between the HRS and LRO for 1-component galaxies is shown in Figure A.2. These quantities behave as expected after the simulation recovering, on average, their values. Notice for instance that although the Sérsic index is not as well preserved for high values, the classification due to such an index is preserved, namely 80% of galaxies with $n > 2.5$ for LRO still have $n > 2.5$ after the simulation.

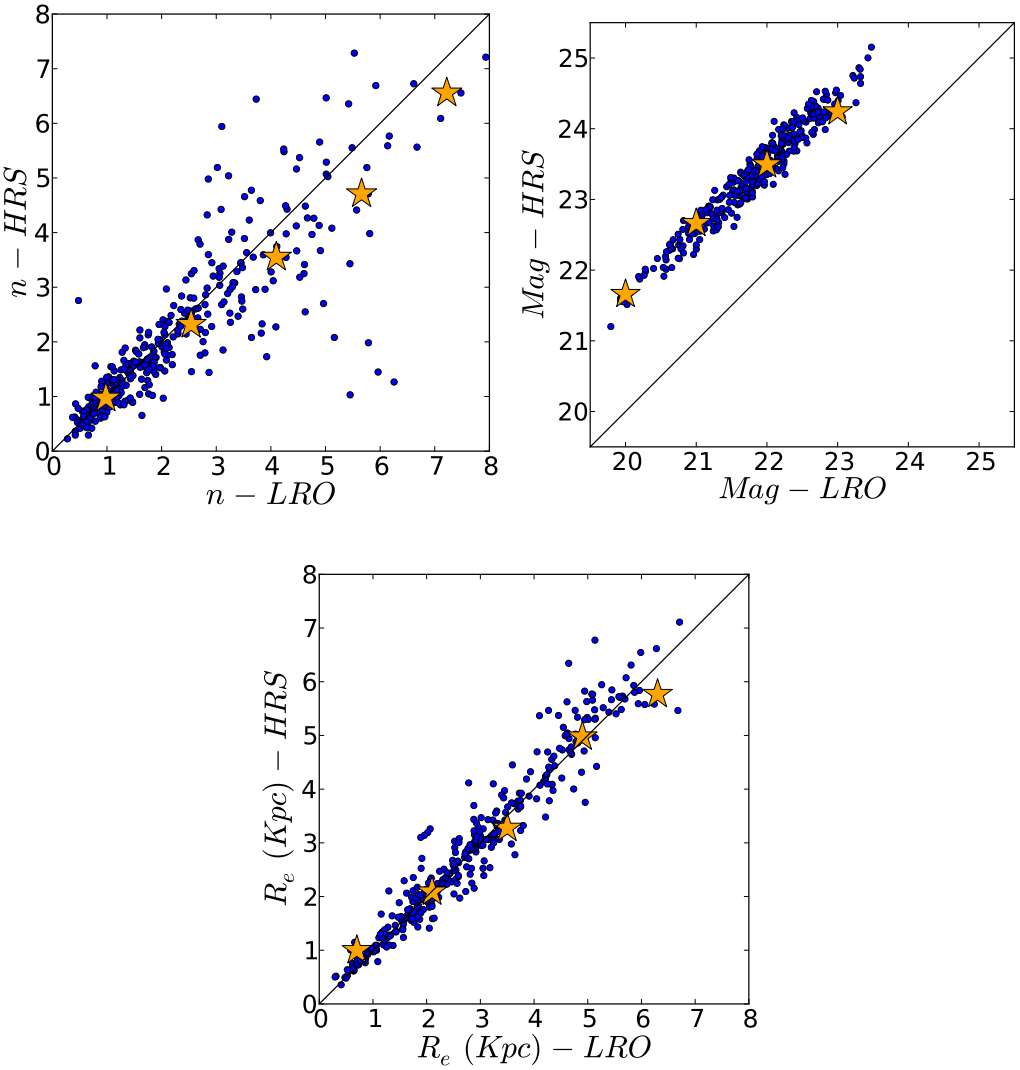


Figure A.2: Comparison between the results from the fitting for the *HRS* galaxies versus the *LRO* sample, for the Sérsic index (top left), magnitude (top right), and effective radii (bottom). The effect on the *HRS* magnitudes due to luminosity evolution and surface brightness dimming, introduced in the simulations, is removed to better compare with the *LRO*. The yellow stars represent the mean values for the *HRS* galaxies.

After applying the three methods to classify the galaxies as 1- or 2-components, in Table A.1 we summarize the difference in the fraction of 2-component galaxies in the *HRS* with respect to the *LRO* and the *HRO*.

	LRO galaxies	*HRS* galaxies	*HRO* galaxies
Visual	0.38	0.17	0.00
F-test	0.50	0.04	0.21
RFF	0.36	0.10	0.31

Table A.1: Fraction of 2-component galaxies selected by the three methods for different subsample of galaxies.

An analogous comparison of the magnitude and effective radii between the HRS and LRO for 2-component galaxies is shown in Figures A.3 and A.4. Notice however that while in Figure A.2 we considered the whole sample LRO vs. HRS, now only the ones of LRO classified as 2-component (together with the corresponding ones of HRS) are taken into account. Thus we obtain for each method two symbols for the magnitude (one for each of the two components), and two for the effective radii.

Even though there is some scatter in the plots of Figure A.4, and the errors are in some cases large, the mean values of the effective radii in HRS galaxies, for both components, are generally in agreement with the measures obtained for the LRO ones. For smaller values of the outer component in the LRO, the simulations show that we would measure larger effective radii at hight redshift, which suggests that the small values of sizes we obtain for the HRO must be real.

Figure A.5 also shows that the fraction of HRS 2-component galaxies (yellow diamond) is similar (although slightly higher) to that of the HRO (black star at $z \sim 2.75$), which might imply that most of the evolution we see in that fraction with redshift may not be real but due to resolution and depth issues at high redshift. This shows the difficulty of carrying out a study of structure at high redshift. However, if we consider only the visual method, we observe that the evolution could be real. It is interesting to notice that while for the HRO the visual classification fails to select any 2-component galaxies, it selects almost 20% in the HRS.

In Figure A.6 we plot the fraction of 2-component HRS galaxies as a function of mass. As in Figure 2.7 we observe that the fraction increases with higher masses in a similar manner, but is about 2 times lower than for the original galaxies (notice that in the HRO we detect about half of the galaxies selected as 2-components in the LRO sample). As we detect a larger fraction of 2-component galaxies in the original sample than in the HRS galaxies, this implies that the high fraction we have found at higher masses must be real.

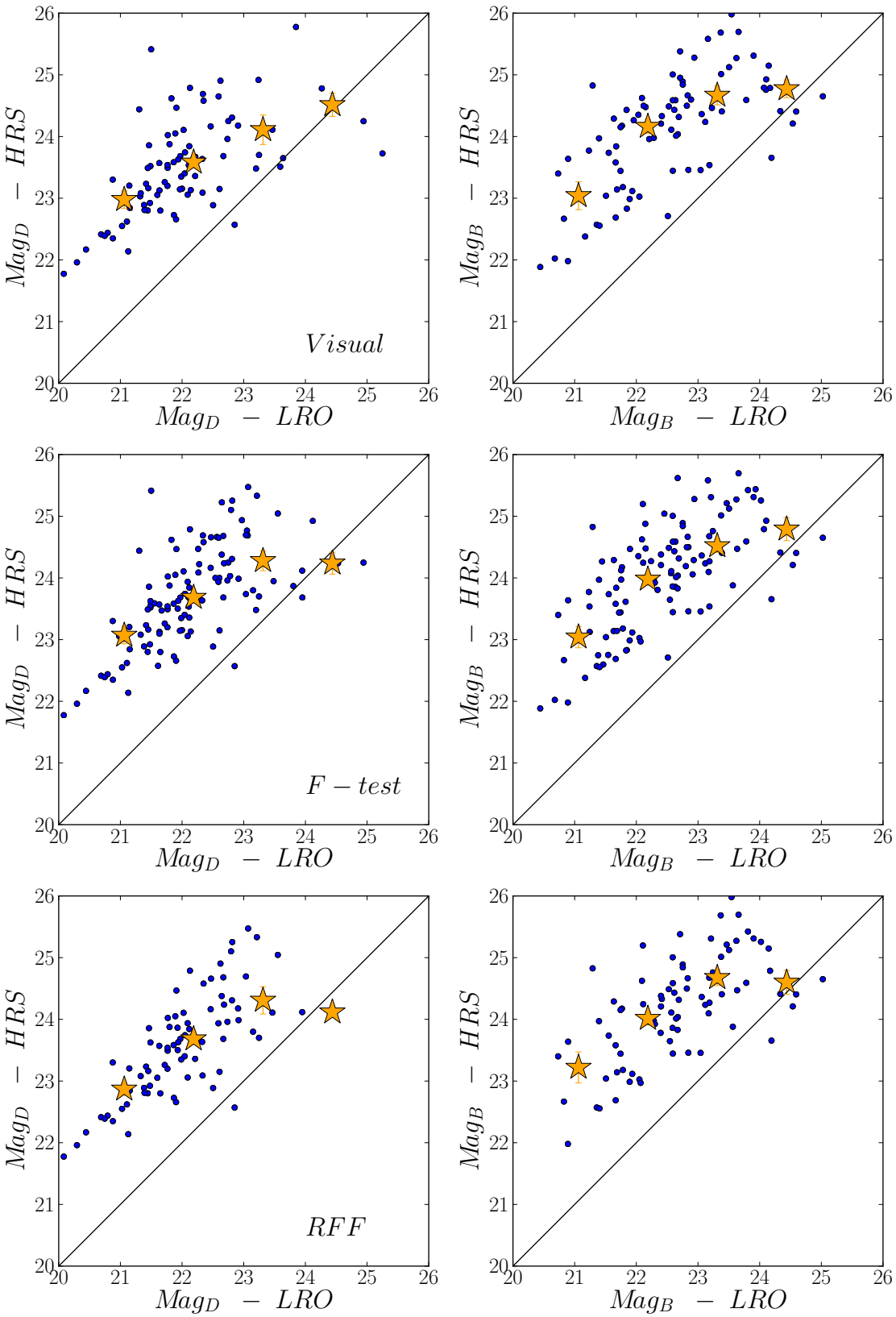


Figure A.3: Magnitude of the disc-like outer (left) and bulge-like inner (right) component of high-redshift simulated versus low-redshift original galaxies for each method (top panel: visual classification, middle panel: F-test and bottom panel: RFF method). The effect on the HRS magnitudes due to luminosity evolution and surface brightness dimming, introduced in the simulations, is removed to better compare with the LRO. The yellow stars represent the mean value of the magnitudes for the HRS galaxies.

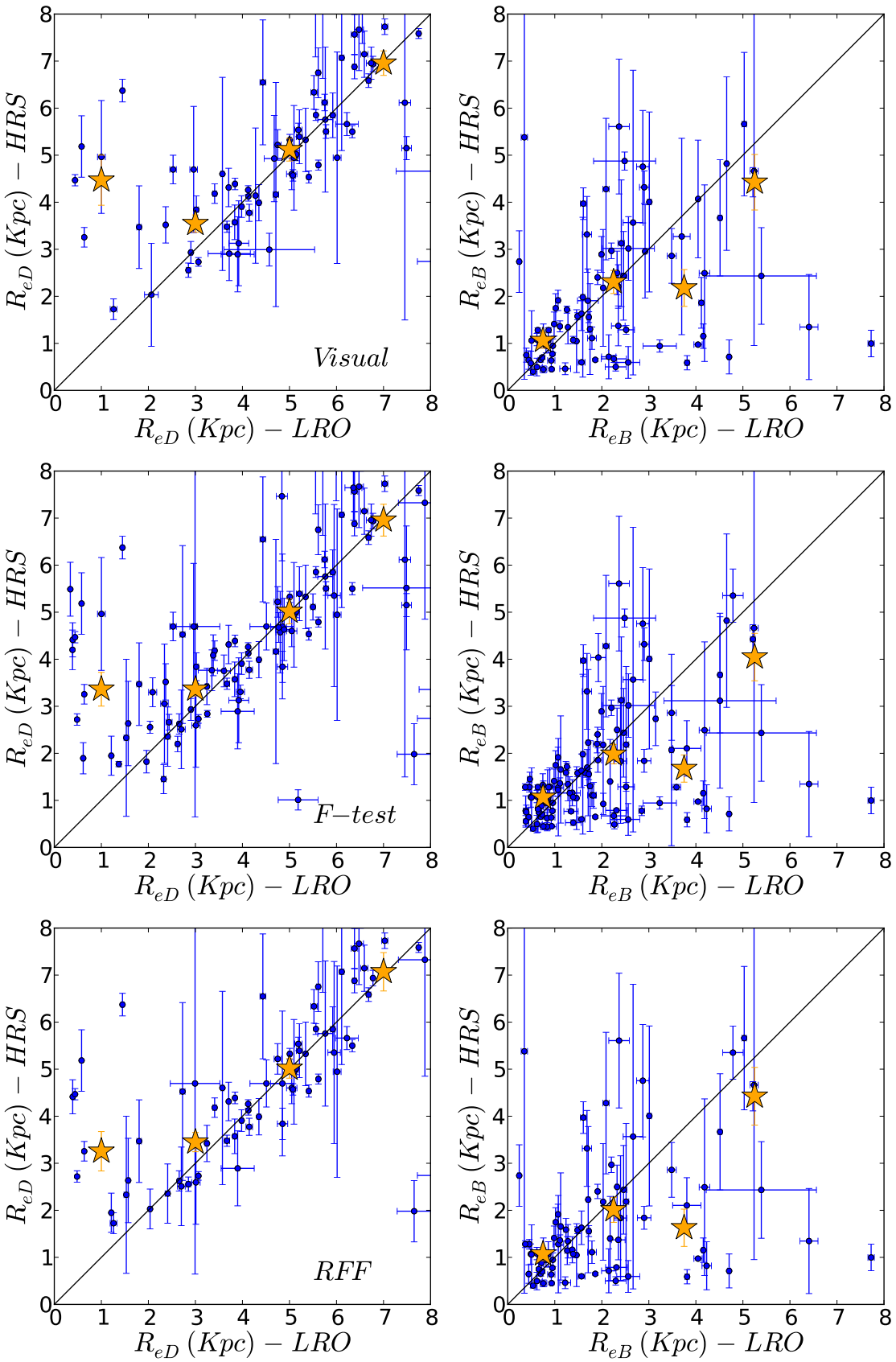


Figure A.4: Effective radii of the disc-like outer (right) and bulge-like inner (left) component of high-redshift simulated versus low-redshift original galaxies for each method (top panel: visual classification, middle panel: F-test and bottom panel: RFF method). The yellow stars represent the mean value of the effective radii for the HRS galaxies.

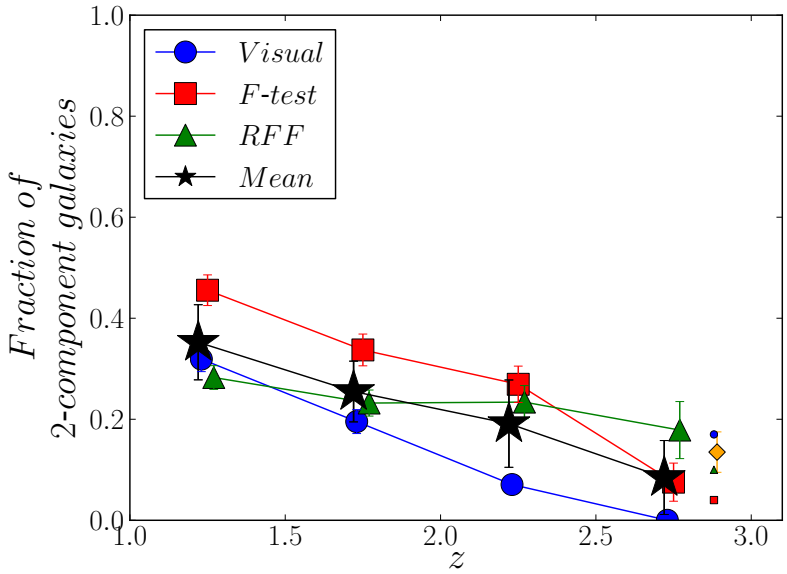


Figure A.5: Comparison of the fraction of 2-component galaxies between observations and simulations. The bigger blue circles, red squares and green triangles represent the fractions of 2-component galaxies, from the whole sample, as function of redshift. The black stars show the mean values of the three methods (same as Figure 2.8). The smaller blue circle, red square and green triangle represent the fractions of 2-component *HRS* galaxies for each method, and the yellow diamond is the mean between the Visual and *RFF* method.

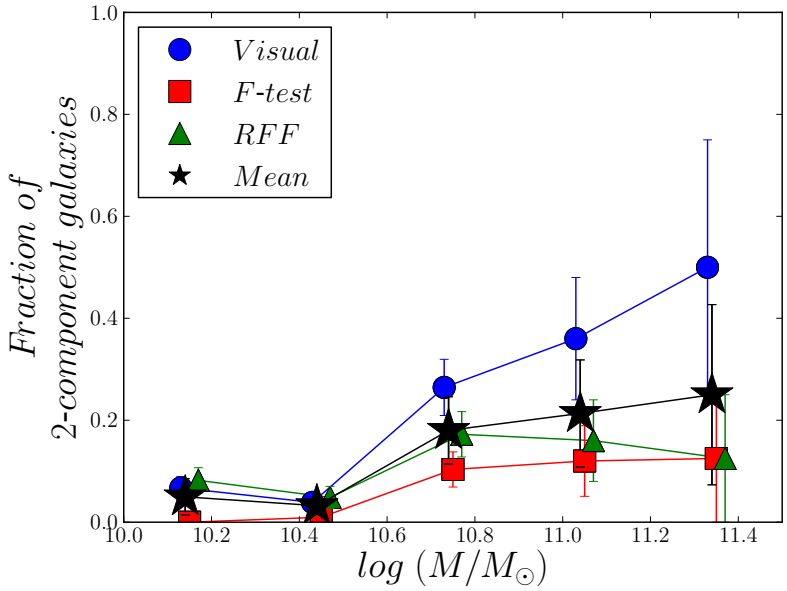


Figure A.6: Fraction of 2-component galaxies as a function of mass for the *HRS* simulated galaxies. The points are coloured as in Figure 2.7.

Appendix B

Extended photometry

The photometry obtained for Chapter 3 consists of the four *HST* bands (two visible bands, denoted V and i, and two near-infrared ones, denoted J and H). We investigate the effects that using only these four bands have in the results of the SED fitting. To this end, we use the galaxy photometry from Galametz *et al.* (2013) for the same galaxies in our sample.

The 17 bands used for this photometry are described in Section 3.2, and include the 4 *HST* bands used in Chapter 3. We discuss the comparison in derived properties between using the 4 *HST* bands, and using the photometric catalogue from Galametz *et al.* (2013). We show the results of this comparison on the left side of Figure B.1, where we observe that, due to not having rest-frame IR fluxes from Spitzer, the J rest-frame magnitude is not well recovered, however, U and V are. We then show, on the right panels of Figure B.1, that by adding only K and $ch1$ bands, we are able to recover the rest-frame magnitude J as well as when using the 17 photometric bands.

In Figure B.2 we show that using just the 4 *HST* bands, we obtain systematically lower SFRs than using all 17 bands. This is due to not having photometry in the ultraviolet, which makes it more difficult to constrain the UV slope in the SED fitting. We find that adding the U band to the 4 *HST* bands we recover the same SFR as with 17 bands. We also note that by adding K and $ch1$, apart from U, does not change the recovered SFR rates.

Finally we show in Figure B.3 that including U, K and $ch1$ to the 4 *HST* bands, we also obtain results of the stellar mass consistent with those obtained using 17 bands. We

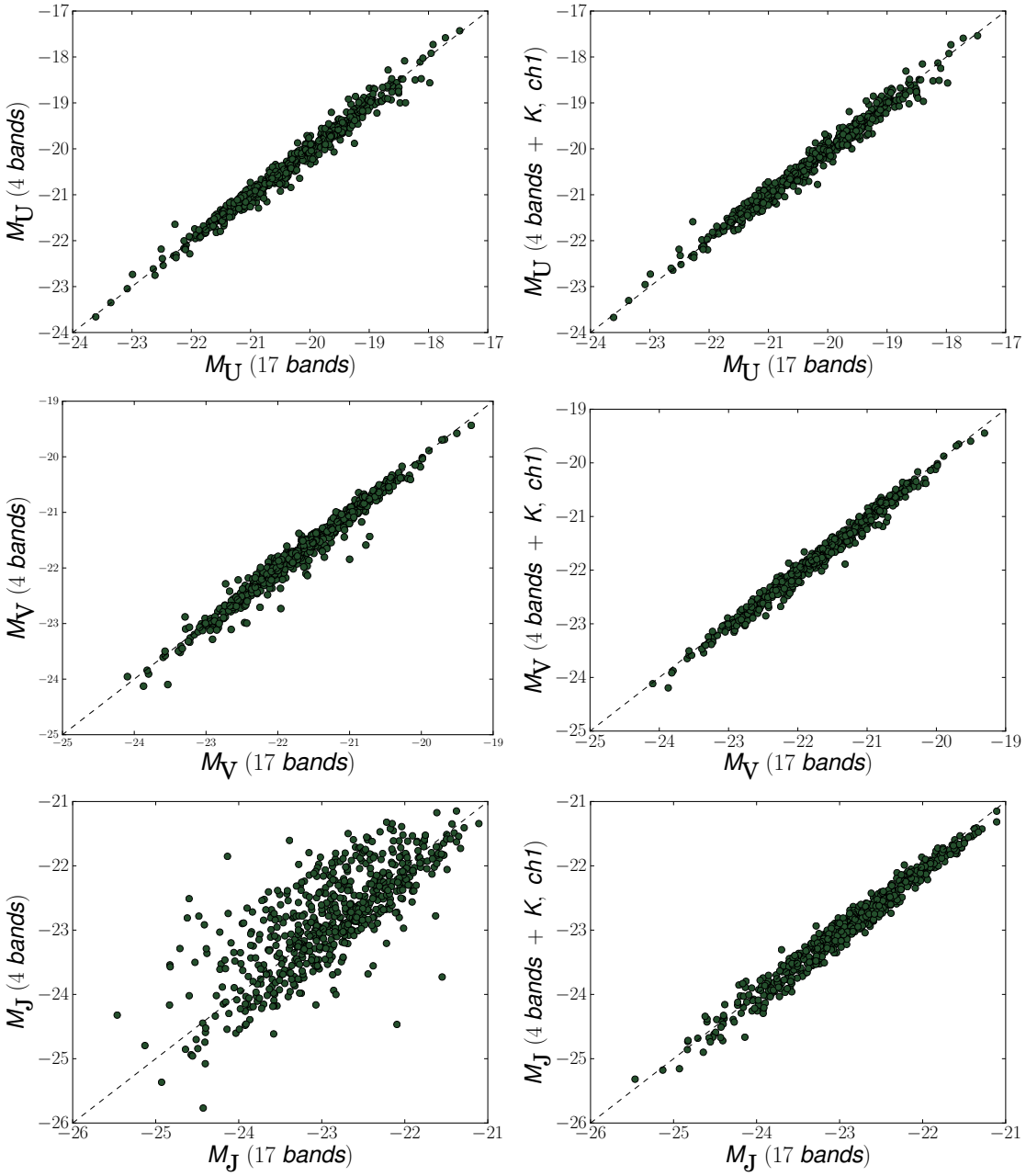


Figure B.1: On the left panels, we compare the computed rest-frame magnitudes obtained using 4 *HST* bands (H, J, i, V) and 17 bands from Galametz *et al.* (2013). On the right panels we show how the rest-frame magnitudes change by adding K and $ch1$ band to the 4 *HST* bands (H, J, i, V), in comparison with those obtained from the 17 bands photometry.

conclude that using $UViJHK$ and the Spitzer $ch1$ bands are sufficient to obtain reliable results in terms of rest-frame colours, stellar masses and SFRs from SED fitting. We thus derive what these colours are from the assumptions we make in §3.3.3.

In order to estimate the flux of the components (bulge and disc) in the K, U and $ch1$ bands, we first examine a volume limited sample of nearby galaxies ($z < 0.3$, $M_r < -21.2$) from GAMA (Liske *et al.* 2015) for which a bulge to disc decomposition is available. These sample if formed by the blue galaxies containing a bulge and a disc component (Vulcani

et al. 2014; Kennedy *et al.* 2016). Figure B.4 shows how the B/T change as a function of rest-frame wavelength for this sample of nearby galaxies.

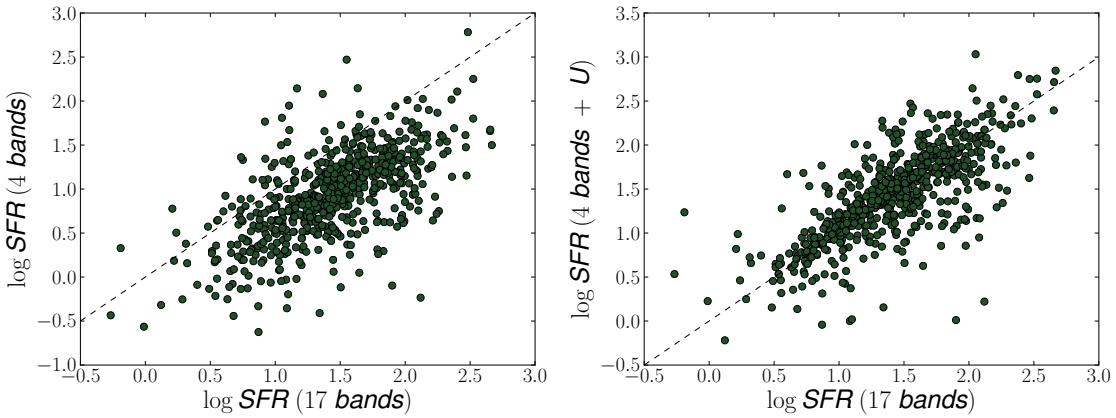


Figure B.2: On the left panels, we compare the SFR obtained using 4 *HST* bands (H, J, i, V) and 17 bands from Galametz *et al.* (2013). On the right panels we show how the SFR changes by adding the U band to the 4 *HST* bands (H, J, i, V), in comparison the those obtained from the 17 bands photometry.

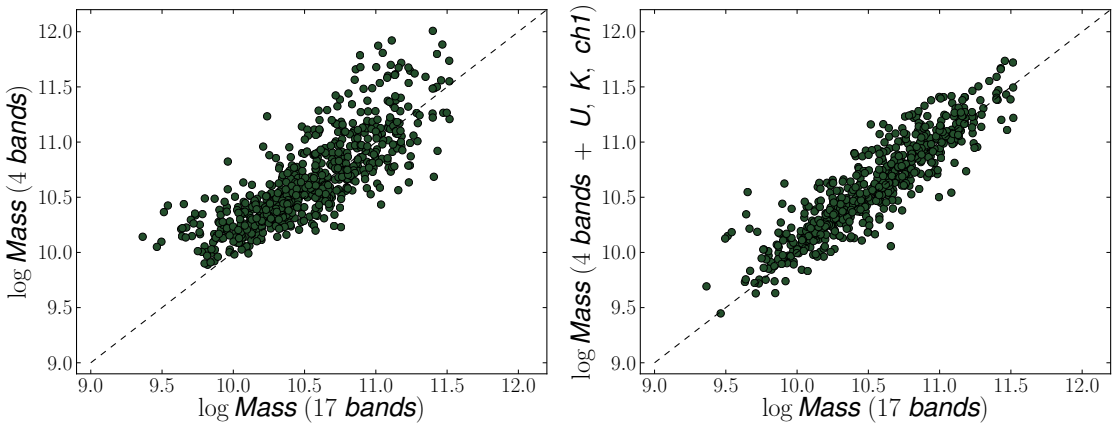


Figure B.3: On the left panels, we compare the stellar mass obtained using 4 *HST* bands (H, J, i, V) and 17 bands from Galametz *et al.* (2013). On the right panels we show how the stellar mass changes when the U, K and $ch1$ bands are added to the 4 *HST* bands (H, J, i, V), in comparison to those obtained from the 17 bands photometry.

For each 2-component galaxy in our high redshift sample we calculate the rest-frame magnitudes that correspond to the observed H and K bands, which will be different for galaxies at different redshifts. We then determine the ratio of B/T between these two rest-frame wavelengths by interpolating from the relation observed in Figure B.4. We plot these results in Figure B.5 (red circles) and find that this ratio is about 0.85 for all our

galaxies. We can compute the B/T in the K band as follows:

$$(B/T)_K = 0.85(B/T)_H.$$

We can therefore calculate the flux of the bulge and disc component in the K-band. Analogously, for $ch1$ we obtain:

$$(B/T)_{ch1} = 0.65(B/T)_H.$$

To confirm whether the relation of B/T with wavelength from nearby galaxies can be applied to high redshift ones, we compare the ratio of (B/T) between H and J bands from our surface brightness fittings to those obtained from the low redshift sample from Figure B.4. We find that in both cases

$$(B/T)_J \sim 0.9(B/T)_H$$

(blue diamonds and purple stars in Figure B.5).

Figure B.4 shows that the relation of B/T with wavelength flattens towards the ultraviolet and, therefore, we assume that the B/T in the U band will be the same as in the V band for all redshifts:

$$(B/T)_U = (B/T)_V.$$

We use these corrections to obtain photometry for the disc and bulge components in the U, K and $ch1$, and use them in addition to the photometry from our 4 ***HST*** bands (V, i, J, H) to perform SED fittings.

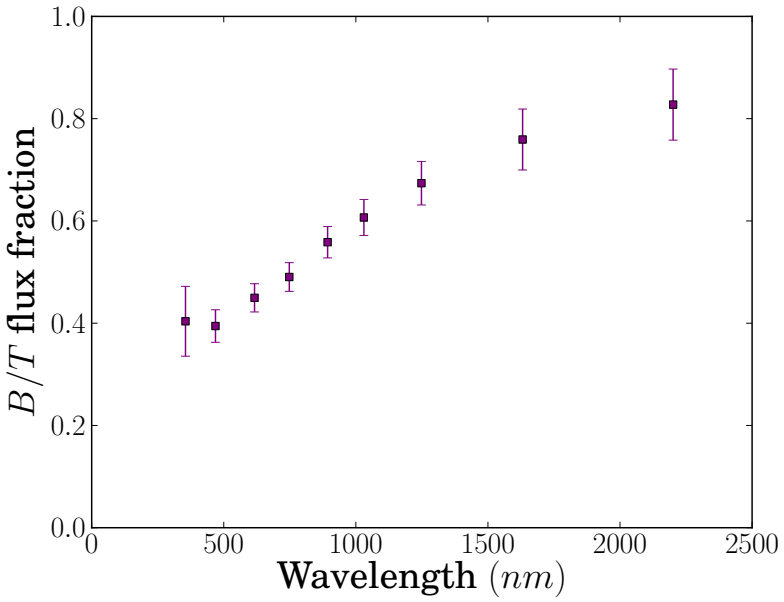


Figure B.4: B/T flux ratio as a function of wavelength for a sample of blue nearby galaxies from the GAMA survey.

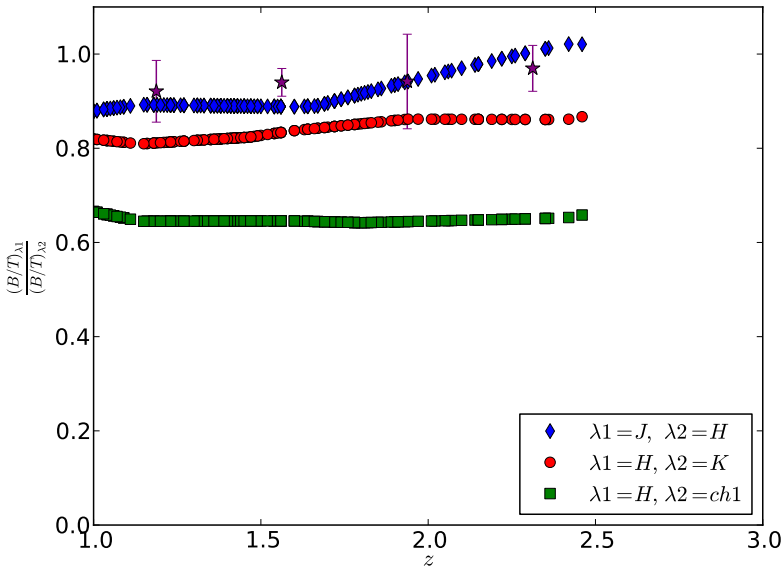


Figure B.5: B/T ratio between the rest-frame magnitudes of our 2-component galaxies corresponding to H and K (red circles), H and $ch1$ (green squares) and J and H (blue diamonds). The B/T ratio is calculated by interpolation of Figure B.4 for the corresponding rest-frame magnitudes in each case. The purple stars are the average ratio between the B/T obtained in the H and J bands from our surface brightness fitting.

Bibliography

Ade P. A. R., Aghanim N., Arnaud M., Ashdown M., Aumont J., Baccigalupi C., Banday A. J., Barreiro R. B., Bartlett J. G., Bartolo N., et al., 2016. A&A, **594**, A13. *Planck 2015 results. XIII. Cosmological parameters*.

Andredakis Y. C., Sanders R. H., 1994. MNRAS, **267**, 283. *Exponential bulges in late-type spirals: an improved description of the light distribution*.

Ashby M. L. N., Willner S. P., Fazio G. G., Huang J.-S., Arendt R., Barmby P., Barro G., Bell E. F., Bouwens R., Cattaneo A., Croton D., Davé R., Dunlop J. S., Egami E., Faber S., Finlator K., Grogin N. A., Guhathakurta P., Hernquist L., Hora J. L., Illingworth G., Kashlinsky A., Koekemoer A. M., Koo D. C., Labbé I., Li Y., Lin L., Moseley H., Nandra K., Newman J., Noeske K., Ouchi M., Peth M., Rigopoulou D., Robertson B., Sarajedini V., Simard L., Smith H. A., Wang Z., Wechsler R., Weiner B., Wilson G., Wuyts S., Yamada T., Yan H., 2013. *ApJ*, **769**, 80. *SEDS: The Spitzer Extended Deep Survey. Survey Design, Photometry, and Deep IRAC Source Counts*.

Baldry I. K., Glazebrook K., Brinkmann J., Ivezić Ž., Lupton R. H., Nichol R. C., Szalay A. S., 2004. ApJ, **600**, 681. *Quantifying the Bimodal Color-Magnitude Distribution of Galaxies*.

Balogh M. L., Baldry I. K., Nichol R., Miller C., Bower R., Glazebrook K., 2004. ApJ, **615**, L101. *The Bimodal Galaxy Color Distribution: Dependence on Luminosity and Environment*.

Bamford S. P., Nichol R. C., Baldry I. K., Land K., Lintott C. J., Schawinski K., Slosar A., Szalay A. S., Thomas D., Torki M., Andreescu D., Edmondson E. M., Miller C. J., Murray P., Raddick M. J., Vandenberg J., 2009. MNRAS, **393**, 1324. *Galaxy Zoo: the dependence of morphology and colour on environment*.

Barden M., Häußler B., Peng C. Y., McIntosh D. H., Guo Y., 2012. *MNRAS*, **422**, 449. *GALAPAGOS: from pixels to parameters*.

Barden M., Jahnke K., Häußler B., 2008. *ApJS*, **175**, 105. *FERENGI: Redshifting Galaxies from SDSS to GEMS, STAGES, and COSMOS*.

Barro G., Faber S. M., Pérez-González P. G., Koo D. C., Williams C. C., Kocevski D. D., Trump J. R., Mozena M., McGrath E., van der Wel A., Wuyts S., Bell E. F., Croton D. J., Ceverino D., Dekel A., Ashby M. L. N., Cheung E., Ferguson H. C., Fontana A., Fang J., Giavalisco M., Grogin N. A., Guo Y., Hathi N. P., Hopkins P. F., Huang K.-H., Koekemoer A. M., Kartaltepe J. S., Lee K.-S., Newman J. A., Porter L. A., Primack J. R., Ryan R. E., Rosario D., Somerville R. S., Salvato M., Hsu L.-T., 2013. *ApJ*, **765**, 104. *CANDELS: The Progenitors of Compact Quiescent Galaxies at* $z \sim 2$.

Bell E. F., McIntosh D. H., Barden M., Wolf C., Caldwell J. A. R., Rix H.-W., Beckwith S. V. W., Borch A., Häussler B., Jahnke K., Jogee S., Meisenheimer K., Peng C., Sanchez S. F., Somerville R. S., Wisotzki L., 2004. ApJ, **600**, L11. *GEMS Imaging of Red-Sequence Galaxies at $z \sim 0.7$: Dusty or Old?*

Bershady M. A., Jangren A., Conselice C. J., 2000. AJ, **119**, 2645. *Structural and Photometric Classification of Galaxies. I. Calibration Based on a Nearby Galaxy Sample*.

Bertin E., Arnouts S., 1996. *A&AS*, **117**, 393. *SExtractor: Software for source extraction.*

Bertin G., Lin C. C., Lowe S. A., Thurstans R. P., 1989. ApJ, **338**, 78. *Modal approach to the morphology of spiral galaxies. I - Basic structure and astrophysical viability.*

Blanton M. R., Hogg D. W., Bahcall N. A., Baldry I. K., Brinkmann J., Csabai I., Eisenstein D., Fukugita M., Gunn J. E., Ivezić Ž., Lamb D. Q., Lupton R. H., Loveday J., Munn J. A., Nichol R. C., Okamura S., Schlegel D. J., Shimasaku K., Strauss M. A., Vogeley M. S., Weinberg D. H., 2003. ApJ, **594**, 186. *The Broadband Optical Properties of Galaxies with Redshifts $0.02 < z < 0.22$.*

Bluck A. F. L., Conselice C. J., Almaini O., Laird E. S., Nandra K., Grützbauch R., 2011. MNRAS, **410**, 1174. *On the co-evolution of supermassive black holes and their host galaxies since z= 3*.

Bluck A. F. L., Conselice C. J., Buitrago F., Grützbauch R., Hoyos C., Mortlock A., Bauer A. E., 2012. ApJ, **747**, 34. *The Structures and Total (Minor + Major) Merger Histories of Massive Galaxies up to $z \sim 3$ in the HST GOODS NICMOS Survey: A Possible Solution to the Size Evolution Problem*.

Bottema R., 2003. MNRAS, **344**, 358. *Simulations of normal spiral galaxies*.

Bourne N., Maddox S. J., Dunne L., Auld R., Baes M., Baldry I. K., Bonfield D. G., Cooray A., Croom S. M., Dariush A., de Zotti G., Driver S. P., Dye S., Eales S., Gomez H. L., González-Nuevo J., Hopkins A. M., Ibar E., Jarvis M. J., Lapi A., Madore B., Michałowski M. J., Pohlen M., Popescu C. C., Rigby E. E., Seibert M., Smith D. J. B., Tuffs R. J., van der Werf P., Brough S., Buttiglione S., Cava A., Clements D. L., Conselice C. J., Fritz J., Hopwood R., Ivison R. J., Jones D. H., Kelvin L. S., Liske J., Loveday J., Norberg P., Robotham A. S. G., Rodighiero G., Temi P., 2012. MNRAS, **421**, 3027. *Herschel-ATLAS/GAMA: a census of dust in optically selected galaxies from stacking at submillimetre wavelengths*.

Brammer G. B., Whitaker K. E., van Dokkum P. G., Marchesini D., Labbé I., Franx M., Kriek M., Quadri R. F., Illingworth G., Lee K.-S., Muzzin A., Rudnick G., 2009. ApJ, **706**, L173. *The Dead Sequence: A Clear Bimodality in Galaxy Colors from $z = 0$ to $z = 2.5$.*

Brammer G. B., van Dokkum P. G., Coppi P., 2008. *ApJ*, **686**, 1503. *EAZY: A Fast, Public Photometric Redshift Code*.

Bridge C. R., Carlberg R. G., Sullivan M., 2010. ApJ, **709**, 1067. *The CFHTLS-Deep Catalog of Interacting Galaxies. I. Merger Rate Evolution to $z = 1.2$.*

Bruce V. A., Dunlop J. S., Cirasuolo M., McLure R. J., Targett T. A., Bell E. F., Croton D. J., Dekel A., Faber S. M., Ferguson H. C., Grogin N. A., Kocevski D. D., Koekemoer A. M., Koo D. C., Lai K., Lotz J. M., McGrath E. J., Newman J. A., van der Wel A., 2012. *MNRAS*, **427**, 1666. *The morphologies of massive galaxies at* $1 < z < 3$ *in the CANDELS-UDS field: compact bulges, and the rise and fall of massive discs*.

Bruce V. A., Dunlop J. S., McLure R. J., Cirasuolo M., Buitrago F., Bowler R. A. A., Targett T. A., Bell E. F., McIntosh D. H., Dekel A., Faber S. M., Ferguson H. C., Grogin N. A., Hartley W., Kocevski D. D., Koekemoer A. M., Koo D. C., McGrath E. J., 2014a. *MNRAS*, **444**, 1001. *The bulge-disc decomposed evolution of massive galaxies at* $1 < z < 3$ *in CANDELS*.

Bruce V. A., Dunlop J. S., McLure R. J., Cirasuolo M., Buitrago F., Bowler R. A. A., Targett T. A., Bell E. F., McIntosh D. H., Dekel A., Faber S. M., Ferguson H. C., Grogin N. A., Hartley W., Kocevski D. D., Koekemoer A. M., Koo D. C., McGrath E. J., 2014b. *MNRAS*, **444**, 1660. *The decomposed bulge and disc size-mass relations of massive galaxies at* $1 < z < 3$ *in CANDELS*.

Bruzual G., Charlot S., 2003. *MNRAS*, **344**, 1000. *Stellar population synthesis at the resolution of 2003*.

Buitrago F., Trujillo I., Conselice C. J., Bouwens R. J., Dickinson M., Yan H., 2008. *ApJ*, **687**, L61. *Size Evolution of the Most Massive Galaxies at* $1.7 < z < 3$ *from GOODS NICMOS Survey Imaging*.

Buitrago F., Trujillo I., Conselice C. J., Häußler B., 2013. MNRAS, **428**, 1460. *Early-type galaxies have been the predominant morphological class for massive galaxies since only* $z \sim 1$.

Calzetti D., Armus L., Bohlin R. C., Kinney A. L., Koornneef J., Storchi-Bergmann T., 2000. *ApJ*, **533**, 682. *The Dust Content and Opacity of Actively Star-forming Galaxies*.

Calzetti D., Kennicutt, Jr. R. C., Bianchi L., Thilker D. A., Dale D. A., Engelbracht C. W., Leitherer C., Meyer M. J., Sosey M. L., Mutchler M., Regan M. W., Thornley M. D., Armus L., Bendo G. J., Boissier S., Boselli A., Draine B. T., Gordon K. D., Helou G., Hollenbach D. J., Kewley L., Madore B. F., Martin D. C., Murphy E. J., Rieke G. H., Rieke M. J., Roussel H., Sheth K., Smith J. D., Walter F., White B. A., Yi S., Scoville N. Z., Polletta M., Lindler D., 2005. ApJ, **633**, 871. *Star Formation in NGC 5194 (M51a): The Panchromatic View from GALEX to Spitzer*.

Calzetti D., Kinney A. L., Storchi-Bergmann T., 1994. *ApJ*, **429**, 582. *Dust extinction of the stellar continua in starburst galaxies: The ultraviolet and optical extinction law*.

Carrasco E. R., Conselice C. J., Trujillo I., 2010. *MNRAS*, **405**, 2253. *Gemini K-band NIRI Adaptive Optics Observations of massive galaxies at* $1 < z < 2$.

Cassata P., Giavalisco M., Guo Y., Renzini A., Ferguson H., Koekemoer A. M., Salimbeni S., Scarlata C., Grogin N. A., Conselice C. J., Dahlen T., Lotz J. M., Dickinson M., Lin L., 2011. *ApJ*, **743**, 96. *The Relative Abundance of Compact and Normal Massive Early-type Galaxies and Its Evolution from Redshift* $z \sim 2$ *to the Present*.

Chabrier G., 2003. *PASP*, **115**, 763. *Galactic Stellar and Substellar Initial Mass Function*.

Charlot S., Fall S. M., 2000. ApJ, **539**, 718. *A Simple Model for the Absorption of Starlight by Dust in Galaxies*.

Conselice C. J., Bershady M. A., Jangren A., 2000. ApJ, **529**, 886. *The Asymmetry of Galaxies: Physical Morphology for Nearby and High-Redshift Galaxies*.

Conselice C. J., Blackburne J. A., Papovich C., 2005. *ApJ*, **620**, 564. *The Luminosity, Stellar Mass, and Number Density Evolution of Field Galaxies of Known Morphology from* $z = 0.5$ *to* 3.

Conselice C. J., Chapman S. C., Windhorst R. A., 2003. ApJ, **596**, L5. *Evidence for a Major Merger Origin of High-Redshift Submillimeter Galaxies*.

Conselice C. J., Bershady M. A., Dickinson M., Papovich C., 2003. *AJ*, **126**, 1183. *A Direct Measurement of Major Galaxy Mergers at* $z \lesssim 3$.

Conselice C. J., Bluck A. F. L., Buitrago F., Bauer A. E., Grützbauch R., Bouwens R. J., Bevan S., Mortlock A., Dickinson M., Daddi E., Yan H., Scott D., Chapman S. C., Chary R.-R., Ferguson H. C., Giavalisco M., Grogin N., Illingworth G., Jogee S., Koekemoer A. M., Lucas R. A., Mobasher B., Moustakas L., Papovich C., Ravindranath S., Siana B., Teplitz H., Trujillo I., Urry M., Weinzirl T., 2011. *MNRAS*, **413**, 80. *The Hubble Space Telescope GOODS NICMOS Survey: overview and the evolution of massive galaxies at* $1.5 < z < 3$.

Conselice C. J., Mortlock A., Bluck A. F. L., Grützbauch R., Duncan K., 2013. MNRAS, **430**, 1051. *Gas accretion as a dominant formation mode in massive galaxies from the GOODS NICMOS Survey*.

Conselice C. J., Wilkinson A., Duncan K., Mortlock A., 2016. ApJ, **830**, 83. *The Evolution of Galaxy Number Density at* $z < 8$ *and Its Implications*.

Conselice C. J., Gallagher, III J. S., Wyse R. F. G., 2002. AJ, **123**, 2246. *Galaxy Populations and Evolution in Clusters. II. Defining Cluster Populations*.

Conselice C. J., Rajgor S., Myers R., 2008. *MNRAS*, **386**, 909. *The structures of distant galaxies - I. Galaxy structures and the merger rate to* $z \sim 3$ *in the Hubble Ultra-Deep Field*.

Conselice C. J., 2003. ApJS, **147**, 1. *The Relationship between Stellar Light Distributions of Galaxies and Their Formation Histories*.

Conselice C. J., 2006. MNRAS, **373**, 1389. *The fundamental properties of galaxies and a new galaxy classification system*.

Croton D. J., Springel V., White S. D. M., De Lucia G., Frenk C. S., Gao L., Jenkins A., Kauffmann G., Navarro J. F., Yoshida N., 2006. MNRAS, **365**, 11. *The many lives of active galactic nuclei: cooling flows, black holes and the luminosities and colours of galaxies*.

Daddi E., Renzini A., Pirzkal N., Cimatti A., Malhotra S., Stiavelli M., Xu C., Pasquali A., Rhoads J. E., Brusa M., di Serego Alighieri S., Ferguson H. C., Koekemoer A. M., Moustakas L. A., Panagia N., Windhorst R. A., 2005. ApJ, **626**, 680. *Passively Evolving Early-Type Galaxies at* $1.4 \lesssim z \lesssim 2.5$ *in the Hubble Ultra Deep Field*.

Daddi E., Dickinson M., Morrison G., Chary R., Cimatti A., Elbaz D., Frayer D., Renzini A., Pope A., Alexander D. M., Bauer F. E., Giavalisco M., Huynh M., Kurk J., Mignoli M., 2007. ApJ, **670**, 156. *Multiwavelength Study of Massive Galaxies at* $z \sim 2$*. I. Star Formation and Galaxy Growth*.

Dahlen T., Mobasher B., Faber S. M., Ferguson H. C., Barro G., Finkelstein S. L., Finlator K., Fontana A., Gruetzbauch R., Johnson S., Pforr J., Salvato M., Wiklind T., Wuyts S., Acquaviva V., Dickinson M. E., Guo Y., Huang J., Huang K.-H., Newman J. A., Bell E. F., Conselice C. J., Galametz A., Gawiser E., Giavalisco M., Grogin N. A., Hathi N., Kocevski D., Koekemoer A. M., Koo D. C., Lee K.-S., McGrath E. J., Papovich C., Peth M., Ryan R., Somerville R., Weiner B., Wilson G., 2013. ApJ, **775**, 93. *A Critical Assessment of Photometric Redshift Methods: A CANDELS Investigation*.

Dawson S., McCrady N., Stern D., Eckart M. E., Spinrad H., Liu M. C., Graham J. R., 2003. AJ, **125**, 1236. *Optical and Near-Infrared Spectroscopy of a High-Redshift Hard X-Ray-emitting Spiral Galaxy*.

de la Rosa I. G., La Barbera F., Ferreras I., Sánchez Almeida J., Dalla Vecchia C., Martínez-Valpuesta I., Stringer M., 2016. MNRAS, **457**, 1916. *The fate of high-redshift massive compact galaxies*.

de Vaucouleurs G., 1959. *Handbuch der Physik*, **53**, 275. *Classification and Morphology of External Galaxies.*

de Vaucouleurs G., 1961. ApJS, **5**, 233. *Integrated Colors of Bright Galaxies in the u, b, V System.*

Dekel A., Birnboim Y., Engel G., Freundlich J., Goerdt T., Mumcuoglu M., Neistein E., Pichon C., Teyssier R., Zinger E., 2009. Nature, **457**, 451. *Cold streams in early massive hot haloes as the main mode of galaxy formation*.

Dekel A., Sari R., Ceverino D., 2009. ApJ, **703**, 785. *Formation of Massive Galaxies at High Redshift: Cold Streams, Clumpy Disks, and Compact Spheroids*.

Dicke R. H., Peebles P. J. E., Roll P. G., Wilkinson D. T., 1965. ApJ, **142**, 414. *Cosmic Black-Body Radiation.*

Dobbs C. L., Pringle J. E., 2010. MNRAS, **409**, 396. *Age distributions of star clusters in spiral and barred galaxies as a test for theories of spiral structure*.

Dobbs C. L., Theis C., Pringle J. E., Bate M. R., 2010. MNRAS, **403**, 625. *Simulations of the grand design galaxy M51: a case study for analysing tidally induced spiral structure*.

Dullo B. T., Graham A. W., 2013. ApJ, **768**, 36. *Central Stellar Mass Deficits in the Bulges of Local Lenticular Galaxies, and the Connection with Compact* $z \sim 1.5$ *Galaxies*.

Duncan K., Conselice C. J., Mortlock A., Hartley W. G., Guo Y., Ferguson H. C., Davé R., Lu Y., Ownsworth J., Ashby M. L. N., Dekel A., Dickinson M., Faber S., Giavalisco M., Grogin N., Kocevski D., Koekemoer A., Somerville R. S., White C. E., 2014. *MNRAS*, **444**, 2960. *The mass evolution of the first galaxies: stellar mass functions and star formation rates at* $4 < z < 7$ *in the CANDELS GOODS-South field*.

Dunlop J. S., Rogers A. B., McLure R. J., Ellis R. S., Robertson B. E., Koekemoer A., Dayal P., Curtis-Lake E., Wild V., Charlot S., Bowler R. A. A., Schenker M. A., Ouchi M., Ono Y., Cirasuolo M., Furlanetto S. R., Stark D. P., Targett T. A., Schneider E., 2013. MNRAS, **432**, 3520. *The UV continua and inferred stellar populations of galaxies at* $z \sim 7 - 9$ *revealed by the Hubble Ultra-Deep Field 2012 campaign*.

Einstein A., 1916. *Annalen der Physik*, **354**, 769. *Die Grundlage der allgemeinen Relativitätstheorie*.

Elmegreen B. G., Elmegreen D. M., 2005. ApJ, **627**, 632. *Stellar Populations in 10 Clump-Cluster Galaxies of the Hubble Ultra Deep Field*.

Elmegreen D. M., Elmegreen B. G., Rubin D. S., Schaffer M. A., 2005. ApJ, **631**, 85. *Galaxy Morphologies in the Hubble Ultra Deep Field: Dominance of Linear Structures at the Detection Limit*.

Elmegreen D. M., Elmegreen B. G., Marcus M. T., Shahinyan K., Yau A., Petersen M., 2009. ApJ, **701**, 306. *Clumpy Galaxies in Goods and Gems: Massive Analogs of Local Dwarf Irregulars*.

Elmegreen B. G., 2002. ApJ, **577**, 206. *Star Formation from Galaxies to Globules*.

Engargiola G., Plambeck R. L., Rosolowsky E., Blitz L., 2003. ApJS, **149**, 343. *Giant Molecular Clouds in M33. I. BIMA All-Disk Survey*.

Fall S. M., Efstathiou G., 1980. MNRAS, **193**, 189. *Formation and rotation of disc galaxies with haloes*.

Fantin D. S. M., Merrifield M. R., Green A. M., 2008. MNRAS, **390**, 1055. *Modelling ultrafine structure in dark matter haloes*.

Ferguson H. C., Dickinson M., Giavalisco M., Kretchmer C., Ravindranath S., Idzi R., Taylor E., Conselice C. J., Fall S. M., Gardner J. P., Livio M., Madau P., Moustakas L. A., Papovich C. M., Somerville R. S., Spinrad H., Stern D., 2004. *ApJ*, **600**, L107. *The Size Evolution of High-Redshift Galaxies*.

Fischera J., Dopita M., 2005. ApJ, **619**, 340. *Attenuation Caused by a Distant Isothermal Turbulent Screen*.

Fontana A., Dunlop J. S., Paris D., Targett T. A., Boutsia K., Castellano M., Galametz A., Grazian A., McLure R., Merlin E., Pentericci L., Wuyts S., Almaini O., Caputi K., Chary R.-R., Cirasuolo M., Conselice C. J., Cooray A., Daddi E., Dickinson M., Faber S. M., Fazio G., Ferguson H. C., Giallongo E., Giavalisco M., Grogin N. A., Hathi N., Koekemoer A. M., Koo D. C., Lucas R. A., Nonino M., Rix H. W., Renzini A., Rosario D., Santini P., Scarlata C., Sommariva V., Stark D. P., van der Wel A., Vanzella E., Wild V., Yan H., Zibetti S., 2014. *A&A*, **570**, A11. *The Hawk-I UDS and GOODS Survey (HUGS): Survey design and deep K-band number counts*.

Freeman K. C., 1970. ApJ, **160**, 811. *On the Disks of Spiral and S0 Galaxies*.

Friedmann A., 1922. *Zeitschrift fur Physik*, **10**, 377. *Über die Krümmung des Raumes*.

Galametz A., Grazian A., Fontana A., Ferguson H. C., Ashby M. L. N., Barro G., Castellano M., Dahlen T., Donley J. L., Faber S. M., Grogin N., Guo Y., Huang K.-H., Kocevski D. D., Koekemoer A. M., Lee K.-S., McGrath E. J., Peth M., Willner S. P., Almaini O., Cooper M., Cooray A., Conselice C. J., Dickinson M., Dunlop J. S., Fazio G. G., Foucaud S., Gardner J. P., Giavalisco M., Hathi N. P., Hartley W. G., Koo D. C., Lai K., de Mello D. F., McLure R. J., Lucas R. A., Paris D., Pentericci L., Santini P., Simpson C., Sommariva V., Targett T., Weiner B. J., Wuyts S., the CANDELS Team, 2013. *ApJs*, **206**, 10. *CANDELS Multiwavelength Catalogs: Source Identification and Photometry in the CANDELS UKIDSS Ultra-deep Survey Field*.

Genzel R., Tacconi L. J., Eisenhauer F., Förster Schreiber N. M., Cimatti A., Daddi E., Bouché N., Davies R., Lehnert M. D., Lutz D., Nesvadba N., Verma A., Abuter R., Shapiro K., Sternberg A., Renzini A., Kong X., Arimoto N., Mignoli M., 2006. Nature, **442**, 786. *The rapid formation of a large rotating disk galaxy three billion years after the Big Bang*.

Giavalisco M., Ferguson H. C., Koekemoer A. M., Dickinson M., Alexander D. M., Bauer F. E., Bergeron J., Biagetti C., Brandt W. N., Casertano S., Cesarsky C., Chatzichristou E., Conselice C., Cristiani S., Da Costa L., Dahlen T., de Mello D., Eisenhardt P., Erben T., Fall S. M., Fassnacht C., Fosbury R., Fruchter A., Gardner J. P., Grogin N., Hook R. N., Hornschemeier A. E., Idzi R., Jogee S., Kretchmer C., Laidler V., Lee K. S., Livio M., Lucas R., Madau P., Mobasher B., Moustakas L. A., Nonino M., Padovani P., Papovich C., Park Y., Ravindranath S., Renzini A., Richardson M., Riess A., Rosati P., Schirmer M., Schreier E., Somerville R. S., Spinrad H., Stern D., Stiavelli M., Strolger L., Urry C. M., Vandame B., Williams R., Wolf C., 2004. ApJ, **600**, L93. *The Great Observatories Origins Deep Survey: Initial Results from Optical and Near-Infrared Imaging*.

Graham A. W., Driver S. P., 2005. *PASA*, **22**, 118. *A Concise Reference to (Projected) Sérsic $R^{1/n}$ Quantities, Including Concentration, Profile Slopes, Petrosian Indices, and Kron Magnitudes*.

Graham A. W., Dullo B. T., Savorgnan G. A. D., 2015. ApJ, **804**, 32. *Hiding in Plain Sight: An Abundance of Compact Massive Spheroids in the Local Universe*.

Graham A. W., Trujillo I., Caon N., 2001. AJ, **122**, 1707. *Galaxy Light Concentration. I. Index Stability and the Connection with Galaxy Structure, Dynamics, and Supermassive Black Holes*.

Grogin N. A., Kocevski D. D., Faber S. M., Ferguson H. C., Koekemoer A. M., Riess A. G., Acquaviva V., Alexander D. M., Almaini O., Ashby M. L. N., Barden M., Bell E. F., Bournaud F., Brown T. M., Caputi K. I., Casertano S., Cassata P., Castellano M., Challis P., Chary R.-R., Cheung E., Cirasuolo M., Conselice C. J., Roshan Cooray A., Croton D. J., Daddi E., Dahlen T., Davé R., de Mello D. F., Dekel A., Dickinson M., Dolch T., Donley J. L., Dunlop J. S., Dutton A. A., Elbaz D., Fazio G. G., Filippenko A. V., Finkelstein S. L., Fontana A., Gardner J. P., Garnavich P. M., Gawiser E., Giavalisco M., Grazian A., Guo Y., Hathi N. P., Häussler B., Hopkins P. F., Huang J.-S.,

Huang K.-H., Jha S. W., Kartaltepe J. S., Kirshner R. P., Koo D. C., Lai K., Lee K.-S., Li W., Lotz J. M., Lucas R. A., Madau P., McCarthy P. J., McGrath E. J., McIntosh D. H., McLure R. J., Mobasher B., Moustakas L. A., Mozena M., Nandra K., Newman J. A., Niemi S.-M., Noeske K. G., Papovich C. J., Pentericci L., Pope A., Primack J. R., Rajan A., Ravindranath S., Reddy N. A., Renzini A., Rix H.-W., Robaina A. R., Rodney S. A., Rosario D. J., Rosati P., Salimbeni S., Scarlata C., Siana B., Simard L., Smidt J., Somerville R. S., Spinrad H., Straughn A. N., Strolger L.-G., Telford O., Teplitz H. I., Trump J. R., van der Wel A., Villforth C., Wechsler R. H., Weiner B. J., Wiklind T., Wild V., Wilson G., Wuyts S., Yan H.-J., Yun M. S., 2011. *ApJs*, **197**, 35. *CANDELS: The Cosmic Assembly Near-infrared Deep Extragalactic Legacy Survey*.

Guo Y., Ferguson H. C., Giavalisco M., Barro G., Willner S. P., Ashby M. L. N., Dahlen T., Donley J. L., Faber S. M., Fontana A., Galametz A., Grazian A., Huang K.-H., Kocevski D. D., Koekemoer A. M., Koo D. C., McGrath E. J., Peth M., Salvato M., Wuyts S., Castellano M., Cooray A. R., Dickinson M. E., Dunlop J. S., Fazio G. G., Gardner J. P., Gawiser E., Grogin N. A., Hathi N. P., Hsu L.-T., Lee K.-S., Lucas R. A., Mobasher B., Nandra K., Newman J. A., van der Wel A., 2013. ApJS, **207**, 24. *CANDELS Multi-wavelength Catalogs: Source Detection and Photometry in the GOODS-South Field*.

Guth A. H., 1981. Phys. Rev. D, **23**, 347. *Inflationary universe: A possible solution to the horizon and flatness problems*.

Gwyn S. D. J., 2012. AJ, **143**, 38. *The Canada-France-Hawaii Telescope Legacy Survey: Stacked Images and Catalogs*.

Hartley W. G., Almaini O., Mortlock A., Conselice C. J., Grützbauch R., Simpson C., Bradshaw E. J., Chuter R. W., Foucaud S., Cirasuolo M., Dunlop J. S., McLure R. J., Pearce H. J., 2013. *MNRAS*, **431**, 3045. *Studying the emergence of the red sequence through galaxy clustering: host halo masses at* $z > 2$.

Häußler B., Bamford S. P., Vika M., Rojas A. L., Barden M., Kelvin L. S., Alpaslan M., Robotham A. S. G., Driver S. P., Baldry I. K., Brough S., Hopkins A. M., Liske J., Nichol R. C., Popescu C. C., Tuffs R. J., 2013. *MNRAS*, **430**, 330. *MegaMorph - multiwavelength measurement of galaxy structure: complete Sérsic profile information from modern surveys*.

Hopkins A. M., Beacom J. F., 2006. ApJ, **651**, 142. *On the Normalization of the Cosmic Star Formation History*.

Hopkins P. F., Bundy K., Hernquist L., Wuyts S., Cox T. J., 2010. MNRAS, **401**, 1099. *Discriminating between the physical processes that drive spheroid size evolution*.

Hoyos C., den Brok M., Verdoes Kleijn G., Carter D., Balcells M., Guzmán R., Peletier R., Ferguson H. C., Goudfrooij P., Graham A. W., Hammer D., Karick A. M., Lucey J. R., Matković A., Merritt D., Mouhcine M., Valentijn E., 2011. *MNRAS*, **411**, 2439. *The HST/ACS Coma Cluster Survey - III. Structural parameters of galaxies using single Sérsic fits*.

Hoyos C., Aragón-Salamanca A., Gray M. E., Maltby D. T., Bell E. F., Barazza F. D., Böhm A., Häußler B., Jahnke K., Jogee S., Lane K. P., McIntosh D. H., Wolf C., 2012. *MNRAS*, **419**, 2703. *A new automatic method to identify galaxy mergers - I. Description and application to the Space Telescope A901/902 Galaxy Evolution Survey*.

Hubble E., Humason M. L., 1931. ApJ, **74**, 43. *The Velocity-Distance Relation among Extra-Galactic Nebulae*.

Hubble E. P., 1925. *Popular Astronomy*, **33**. *Cepheids in Spiral Nebulae*.

Hubble E. P., 1926. ApJ, **64**. *Extragalactic nebulae.*

Hubble E., 1929. *Proceedings of the National Academy of Science*, **15**, 168. *A Relation between Distance and Radial Velocity among Extra-Galactic Nebulae*.

Hubble E. P., 1936. *Realm of the Nebulae*.

Huertas-Company M., Bernardi M., Pérez-González P. G., Ashby M. L. N., Barro G., Conselice C., Daddi E., Dekel A., Dimauro P., Faber S. M., Grogin N. A., Kartaltepe J. S., Kocevski D. D., Koekemoer A. M., Koo D. C., Mei S., Shankar F., 2016. MNRAS, **462**, 4495. *Mass assembly and morphological transformations since $z \sim 3$ from CANDELS*.

Ilbert O., McCracken H. J., Le Fèvre O., Capak P., Dunlop J., Karim A., Renzini M. A., Caputi K., Boissier S., Arnouts S., Aussel H., Comparat J., Guo Q., Hudelot P., Kartaltepe J., Kneib J. P., Krogager J. K., Le Floc'h E., Lilly S., Mellier Y., Milvang-Jensen B., Moutard T., Onodera M., Richard J., Salvato M., Sanders D. B., Scoville N., Silverman J. D., Taniguchi Y., Tasca L., Thomas R., Toft S., Tresse L., Vergani D., Wolk M., Zirm A., 2013. A&A, **556**, A55. *Mass assembly in quiescent and star-forming galaxies since $z \simeq 4$ from UltraVISTA*.

Kartaltepe J. S., Mozena M., Kocevski D., McIntosh D. H., Lotz J., Bell E. F., Faber S., Ferguson H., Koo D., Bassett R., Bernyk M., Blancato K., Bournaud F., Cassata P., Castellano M., Cheung E., Conselice C. J., Croton D., Dahlen T., de Mello D. F., DeGroot L., Donley J., Guedes J., Grogin N., Hathi N., Hilton M., Hollon B., Koekemoer A., Liu N., Lucas R. A., Martig M., McGrath E., McPartland C., Mobasher B., Morlock A., O'Leary E., Peth M., Pforr J., Pillepich A., Rosario D., Soto E., Straughn A., Telford O., Sunnquist B., Trump J., Weiner B., Wuyts S., 2015. *ApJs*, **221**, 11. *CANDELS Visual Classifications: Scheme, Data Release, and First Results*.

Kauffmann G., Heckman T. M., White S. D. M., Charlot S., Tremonti C., Peng E. W., Seibert M., Brinkmann J., Nichol R. C., SubbaRao M., York D., 2003. MNRAS, **341**, 54. *The dependence of star formation history and internal structure on stellar mass for 10^5 low-redshift galaxies*.

Kelvin L. S., Driver S. P., Robotham A. S. G., Taylor E. N., Graham A. W., Alpaslan M., Baldry I., Bamford S. P., Bauer A. E., Bland-Hawthorn J., Brown M. J. I., Colless M., Conselice C. J., Holwerda B. W., Hopkins A. M., Lara-López M. A., Liske J., López-Sánchez Á. R., Loveday J., Norberg P., Phillipps S., Popescu C. C., Prescott M., Sansom A. E., Tuffs R. J., 2014. MNRAS, **444**, 1647. *Galaxy And Mass Assembly (GAMA): stellar mass functions by Hubble type*.

Kennedy R., Bamford S. P., Häußler B., Baldry I., Bremer M., Brough S., Brown M. J. I., Driver S., Duncan K., Graham A. W., Holwerda B. W., Hopkins A. M., Kelvin L. S., Lange R., Phillipps S., Vika M., Vulcani B., 2016. MNRAS, **460**, 3458. *Galaxy And Mass Assembly (GAMA): understanding the wavelength dependence of galaxy structure with bulge-disc decompositions*.

Kennicutt, Jr. R. C., 1983. *ApJ*, **272**, 54. *The rate of star formation in normal disk galaxies*.

Kennicutt, Jr. R. C., 1998. *ARA&A*, **36**, 189. *Star Formation in Galaxies Along the Hubble Sequence*.

Khochfar S., Silk J., 2006. ApJ, **648**, L21. *A Simple Model for the Size Evolution of Elliptical Galaxies*.

Koekemoer A. M., Faber S. M., Ferguson H. C., Grogin N. A., Kocevski D. D., Koo D. C., Lai K., Lotz J. M., Lucas R. A., McGrath E. J., Ogaz S., Rajan A., Riess A. G., Rodney S. A., Strolger L., Casertano S., Castellano M., Dahlen T., Dickinson M., Dolch T., Fontana A., Giavalisco M., Grazian A., Guo Y., Hathi N. P., Huang K.-H., van der Wel A., Yan H.-J., Acquaviva V., Alexander D. M., Almaini O., Ashby M. L. N., Barden M., Bell E. F., Bournaud F., Brown T. M., Caputi K. I., Cassata P., Challis P. J., Chary R.-R., Cheung E., Cirasuolo M., Conselice C. J., Roshan Cooray A., Croton D. J., Daddi E., Davé R., de Mello D. F., de Ravel L., Dekel A., Donley J. L., Dunlop J. S., Dutton A. A., Elbaz D., Fazio G. G., Filippenko A. V., Finkelstein S. L., Frazer C., Gardner J. P., Garnavich P. M., Gawiser E., Gruetzbauch R., Hartley W. G., Häussler B., Herrington J., Hopkins P. F., Huang J.-S., Jha S. W., Johnson A., Kartaltepe J. S., Khostovan A. A., Kirshner R. P., Lani C., Lee K.-S., Li W., Madau P., McCarthy P. J., McIntosh D. H., McLure R. J., McPartland C., Mobasher B., Moreira H., Mortlock A., Moustakas L. A., Mozena M., Nandra K., Newman J. A., Nielsen J. L., Niemi S., Noeske K. G., Papovich C. J., Pentericci L., Pope A., Primack J. R., Ravindranath S., Reddy N. A., Renzini A., Rix H.-W., Robaina A. R., Rosario D. J., Rosati P., Salimbeni S., Scarlata C., Siana B., Simard L., Smidt J., Snyder D., Somerville R. S., Spinrad H., Straughn A. N., Telford O., Teplitz H. I., Trump J. R., Vargas C., Villforth C., Wagner C. R., Wandro P., Wechsler R. H., Weiner B. J., Wiklind T., Wild V., Wilson G., Wuyts S., Yun M. S., 2011. *ApJs*, **197**, 36. *CANDELS: The Cosmic Assembly Near-infrared Deep Extragalactic Legacy Survey–The Hubble Space Telescope Observations, Imaging Data Products, and Mosaics*.

Kormendy J., Kennicutt, Jr. R. C., 2004. ARA&A, **42**, 603. *Secular Evolution and the Formation of Pseudobulges in Disk Galaxies*.

Lacey C., Cole S., 1993. *Merger Rates in Hierarchical Models of Galaxy Formation*, In: *Observational Cosmology*, 192, eds Chincarini G. L., Iovino A., Maccacaro T., Maccagni D.

Lang P., Wuyts S., Somerville R. S., Förster Schreiber N. M., Genzel R., Bell E. F., Brammer G., Dekel A., Faber S. M., Ferguson H. C., Grogin N. A., Kocevski D. D., Koekemoer A. M., Lutz D., McGrath E. J., Momcheva I., Nelson E. J., Primack J. R., Rosario D. J., Skelton R. E., Tacconi L. J., van Dokkum P. G., Whitaker K. E., 2014. *ApJ*, **788**, 11. *Bulge Growth and Quenching since* $z = 2.5$ *in CANDELS/3D-HST*.

Lange R., Driver S. P., Robotham A. S. G., Kelvin L. S., Graham A. W., Alpaslan M., Andrews S. K., Baldry I. K., Bamford S., Bland-Hawthorn J., Brough S., Cluver M. E., Conselice C. J., Davies L. J. M., Haeussler B., Konstantopoulos I. S., Loveday J., Moffett A. J., Norberg P., Phillipps S., Taylor E. N., López-Sánchez Á. R., Wilkins S. M., 2015. *MNRAS*, **447**, 2603. *Galaxy And Mass Assembly (GAMA): mass-size relations of* $z < 0.1$ *galaxies subdivided by Sérsic index, colour and morphology*.

Law D. R., Steidel C. C., Erb D. K., Larkin J. E., Pettini M., Shapley A. E., Wright S. A., 2009. ApJ, **697**, 2057. *The Kiloparsec-scale Kinematics of High-redshift Star-forming Galaxies*.

Law D. R., Shapley A. E., Steidel C. C., Reddy N. A., Christensen C. R., Erb D. K., 2012. Nature, **487**, 338. *High velocity dispersion in a rare grand-design spiral galaxy at redshift* $z = 2.18$.

Lemaître G., 1927. *Annales de la Société Scientifique de Bruxelles*, **47**, 49. *Un Univers homogène de masse constante et de rayon croissant rendant compte de la vitesse radiale des nébuleuses extra-galactiques*.

Liddle A., 2003. *An Introduction to Modern Cosmology, Second Edition*.

Lilly S. J., Le Fevre O., Hammer F., Crampton D., 1996. ApJ, **460**, L1. *The Canada-France Redshift Survey: The Luminosity Density and Star Formation History of the Universe to* z *approximately* 1.

Lin C. C., Shu F. H., 1964. ApJ, **140**, 646. *On the Spiral Structure of Disk Galaxies.*

Liske J., Baldry I. K., Driver S. P., Tuffs R. J., Alpaslan M., Andrae E., Brough S., Cluver M. E., Grootes M. W., Gunawardhana M. L. P., Kelvin L. S., Loveday J., Robotham A. S. G., Taylor E. N., Bamford S. P., Bland-Hawthorn J., Brown M. J. I., Drinkwater M. J., Hopkins A. M., Meyer M. J., Norberg P., Peacock J. A., Agius N. K., Andrews S. K., Bauer A. E., Ching J. H. Y., Colless M., Conselice C. J., Croom S. M., Davies L. J. M., De Propris R., Dunne L., Eardley E. M., Ellis S., Foster C., Frenk C. S., Häußler B., Holwerda B. W., Howlett C., Ibarra H., Jarvis M. J., Jones D. H., Kafle P. R., Lacey C. G., Lange R., Lara-López M. A., López-Sánchez Á. R., Maddox S., Madore B. F., McNaught-Roberts T., Moffett A. J., Nichol R. C., Owers M. S., Palamara D., Penny S. J., Phillipps S., Pimbblet K. A., Popescu C. C., Prescott M., Proctor R., Sadler E. M., Sansom A. E., Seibert M., Sharp R., Sutherland W., Vázquez-Mata J. A., van Kampen E., Wilkins S. M., Williams R., Wright A. H., 2015. MNRAS, **452**, 2087. *Galaxy And Mass Assembly (GAMA): end of survey report and data release 2*.

Madau P., Dickinson M., 2014. ARA&A, **52**, 415. *Cosmic Star-Formation History*.

Madau P., Ferguson H. C., Dickinson M. E., Giavalisco M., Steidel C. C., Fruchter A., 1996. MNRAS, **283**, 1388. *High-redshift galaxies in the Hubble Deep Field: colour selection and star formation history to* $z \sim 4$.

Madau P., Pozzetti L., Dickinson M., 1998. ApJ, **498**, 106. *The Star Formation History of Field Galaxies*.

Madau P., 1995. ApJ, **441**, 18. *Radiative transfer in a clumpy universe: The colors of high-redshift galaxies*.

Margalef-Bentabol B., Conselice C. J., Mortlock A., Hartley W., Duncan K., Ferguson H. C., Dekel A., Primack J. R., 2016. *MNRAS*, **461**, 2728. *The formation of bulges, discs and two-component galaxies in the CANDELS Survey at* $z < 3$.

Margalef-Bentabol B., Margalef-Bentabol J., Cepa J., 2012. *JCAP*, **12**, 035. *Evolution of the cosmological horizons in a concordance universe*.

Martig M., Bournaud F., Teyssier R., Dekel A., 2009. ApJ, **707**, 250. *Morphological Quenching of Star Formation: Making Early-Type Galaxies Red*.

McCracken H. J., Milvang-Jensen B., Dunlop J., Franx M., Fynbo J. P. U., Le Fèvre O., Holt J., Caputi K. I., Goranova Y., Buitrago F., Emerson J. P., Freudling W., Hudelot P., López-Sanjuan C., Magnard F., Mellier Y., Møller P., Nilsson K. K., Sutherland W., Tasca L., Zabl J., 2012. A&A, **544**, A156. *UltraVISTA: a new ultra-deep near-infrared survey in COSMOS*.

Meurer G. R., Heckman T. M., Calzetti D., 1999. *ApJ*, **521**, 64. *Dust Absorption and the Ultraviolet Luminosity Density at $z \sim 3$ as Calibrated by Local Starburst Galaxies*.

Mo H., van den Bosch F. C., White S., 2010. *Galaxy Formation and Evolution*.

Mobasher B., Dahlen T., Ferguson H. C., Acquaviva V., Barro G., Finkelstein S. L., Fontana A., Gruetzbauch R., Johnson S., Lu Y., Papovich C. J., Pforr J., Salvato M., Somerville R. S., Wiklind T., Wuyts S., Ashby M. L. N., Bell E., Conselice C. J., Dickinson M. E., Faber S. M., Fazio G., Finlator K., Galametz A., Gawiser E., Giavalisco M., Grazian A., Grogin N. A., Guo Y., Hathi N., Kocevski D., Koekemoer A. M., Koo D. C., Newman J. A., Reddy N., Santini P., Wechsler R. H., 2015. ApJ, **808**, 101. *A Critical Assessment of Stellar Mass Measurement Methods*.

Moore T. J. T., Urquhart J. S., Morgan L. K., Thompson M. A., 2012. MNRAS, **426**, 701. *The effect of spiral arms on star formation in the Galaxy*.

Mortlock A., Conselice C. J., Hartley W. G., Ownsworth J. R., Lani C., Bluck A. F. L., Almaini O., Duncan K., van der Wel A., Koekemoer A. M., Dekel A., Davé R., Ferguson H. C., de Mello D. F., Newman J. A., Faber S. M., Grogin N. A., Kocevski D. D., Lai K., 2013. *MNRAS*, **433**, 1185. *The redshift and mass dependence on the formation of the Hubble sequence at $z > 1$ from CANDELS/UDS*.

Mortlock A., Conselice C. J., Hartley W. G., Duncan K., Lani C., Ownsworth J. R., Almaini O., Wel A. v. d., Huang K.-H., Ashby M. L. N., Willner S. P., Fontana A., Dekel A., Koekemoer A. M., Ferguson H. C., Faber S. M., Grogin N. A., Kocevski D. D., 2015. *MNRAS*, **447**, 2. *Deconstructing the galaxy stellar mass function with UKIDSS and CANDELS: the impact of colour, structure and environment*.

Naab T., Johansson P. H., Ostriker J. P., 2009. ApJ, **699**, L178. *Minor Mergers and the Size Evolution of Elliptical Galaxies*.

Nair P. B., Abraham R. G., 2010. ApJS, **186**, 427. *A Catalog of Detailed Visual Morphological Classifications for 14,034 Galaxies in the Sloan Digital Sky Survey*.

Nandra K., Georgakakis A., Willmer C. N. A., Cooper M. C., Croton D. J., Davis M., Faber S. M., Koo D. C., Laird E. S., Newman J. A., 2007. ApJ, **660**, L11. *AEGIS: The Color-Magnitude Relation for X-Ray-selected Active Galactic Nuclei*.

Nayyeri H., Hemmati S., Mobasher B., Ferguson H. C., Cooray A., Barro G., Faber S. M., Dickinson M., Koekemoer A. M., Peth M., Salvato M., Ashby M. L. N., Darvish B., Donley J., Durbin M., Finkelstein S., Fontana A., Grogin N. A., Gruetzbauch R., Huang K., Khostovan A. A., Kocevski D., Kodra D., Lee B., Newman J., Pacifici C., Pforr J., Stefanon M., Wiklind T., Willner S. P., Wuyts S., Castellano M., Conselice C.,

Dolch T., Dunlop J. S., Galametz A., Hathi N. P., Lucas R. A., Yan H., 2017. ApJS, **228**, 7. *CANDELS Multi-wavelength Catalogs: Source Identification and Photometry in the CANDELS COSMOS Survey Field*.

Noeske K. G., Weiner B. J., Faber S. M., Papovich C., Koo D. C., Somerville R. S., Bundy K., Conselice C. J., Newman J. A., Schiminovich D., Le Floc'h E., Coil A. L., Rieke G. H., Lotz J. M., Primack J. R., Barmby P., Cooper M. C., Davis M., Ellis R. S., Fazio G. G., Guhathakurta P., Huang J., Kassin S. A., Martin D. C., Phillips A. C., Rich R. M., Small T. A., Willmer C. N. A., Wilson G., 2007. ApJ, **660**, L43. *Star Formation in AEGIS Field Galaxies since z=1.1: The Dominance of Gradually Declining Star Formation, and the Main Sequence of Star-forming Galaxies*.

Nonino M., Dickinson M., Rosati P., Grazian A., Reddy N., Cristiani S., Giavalisco M., Kuntschner H., Vanzella E., Daddi E., Fosbury R. A. E., Cesarsky C., 2009. ApJS, **183**, 244. *Deep U Band and R Imaging of Goods-South: Observations, Data Reduction and First Results*.

Olive K. A., Skillman E. D., 2004. ApJ, **617**, 29. *A Realistic Determination of the Error on the Primordial Helium Abundance: Steps toward Nonparametric Nebular Helium Abundances*.

Oort J. H., 1940. ApJ, **91**, 273. *Some Problems Concerning the Structure and Dynamics of the Galactic System and the Elliptical Nebulae NGC 3115 and 4494.*

Ownsworth J. R., Conselice C. J., Mortlock A., Hartley W. G., Buitrago F., 2012. MNRAS, **426**, 764. *Evolution of massive galaxy structural properties and sizes via star formation in the GOODS NICMOS Survey*.

Ownsworth J. R., Conselice C. J., Mundy C. J., Mortlock A., Hartley W. G., Duncan K., Almaini O., 2016. *MNRAS*, **461**, 1112. *The evolution of galaxies at constant number density: a less biased view of star formation, quenching, and structural formation*.

Peebles P. J. E., 1969. *ApJ*, **155**, 393. *Origin of the Angular Momentum of Galaxies*.

Peebles P. J. E., 1982. ApJ, **263**, L1. *Large-scale background temperature and mass fluctuations due to scale-invariant primeval perturbations*.

Peng C. Y., Ho L. C., Impey C. D., Rix H.-W., 2002. *AJ*, **124**, 266. *Detailed Structural Decomposition of Galaxy Images*.

Peng Y.-j., Lilly S. J., Kovač K., Bolzonella M., Pozzetti L., Renzini A., Zamorani G., Ilbert O., Knobel C., Iovino A., Maier C., Cucciati O., Tasca L., Carollo C. M., Silverman J., Kampczyk P., de Ravel L., Sanders D., Scoville N., Contini T., Mainieri V., Scodeggio M., Kneib J.-P., Le Fèvre O., Bardelli S., Bongiorno A., Caputi K., Coppa G., de la Torre S., Franzetti P., Garilli B., Lamareille F., Le Borgne J.-F., Le Brun V., Mignoli M., Perez Montero E., Pello R., Ricciardelli E., Tanaka M., Tresse L., Vergani D., Welikala N., Zucca E., Oesch P., Abbas U., Barnes L., Bordoloi R., Bottini D., Cappi A., Cassata P., Cimatti A., Fumana M., Hasinger G., Koekemoer A., Leauthaud A., Maccagni D., Marinoni C., McCracken H., Memeo P., Meneux B., Nair P., Porciani C., Presotto V., Scaramella R., 2010. ApJ, **721**, 193. *Mass and Environment as Drivers of Galaxy Evolution in SDSS and zCOSMOS and the Origin of the Schechter Function*.

Penzias A. A., Wilson R. W., 1965. ApJ, **142**, 419. *A Measurement of Excess Antenna Temperature at 4080 Mc/s.*

Press W. H., Flannery B., Teukolsy S., Vetterling W., 1988. *Numerical Recipes in C: The Art of Scientific Computing*, Cambridge University Press.

Ravindranath S., Ferguson H. C., Conselice C., Giavalisco M., Dickinson M., Chatzichristou E., de Mello D., Fall S. M., Gardner J. P., Grogin N. A., Hornschemeier A., Jogee S., Koekemoer A., Kretchmer C., Livio M., Mobasher B., Somerville R., 2004. ApJ, **604**, L9. *The Evolution of Disk Galaxies in the GOODS-South Field: Number Densities and Size Distribution*.

Retzlaff J., Rosati P., Dickinson M., Vandame B., Rité C., Nonino M., Cesarsky C., GOODS Team, 2010. A&A, **511**, A50. *The Great Observatories Origins Deep Survey. VLT/ISAAC near-infrared imaging of the GOODS-South field*.

Rubin V. C., Thonnard N., Ford, Jr. W. K., 1978. ApJ, **225**, L107. *Extended rotation curves of high-luminosity spiral galaxies. IV - Systematic dynamical properties, SA through SC*.

Sandage A., 1961. *The Hubble atlas of galaxies*.

Sanders D. B., Salvato M., Aussel H., Ilbert O., Scoville N., Surace J. A., Frayer D. T., Sheth K., Helou G., Brooke T., Bhattacharya B., Yan L., Kartaltepe J. S., Barnes J. E., Blain A. W., Calzetti D., Capak P., Carilli C., Carollo C. M., Comastri A., Daddi E., Ellis R. S., Elvis M., Fall S. M., Franceschini A., Giavalisco M., Hasinger G., Impey C., Koekemoer A., Le Fèvre O., Lilly S., Liu M. C., McCracken H. J., Mobasher B., Renzini A., Rich M., Schinnerer E., Shopbell P. L., Taniguchi Y., Thompson D. J., Urry C. M., Williams J. P., 2007. ApJS, **172**, 86. *S-COSMOS: The Spitzer Legacy Survey of the Hubble Space Telescope ACS 2 deg^2 COSMOS Field I: Survey Strategy and First Analysis*.

Santini P., Maiolino R., Magnelli B., Lutz D., Lamastra A., Li Causi G., Eales S., Andreani P., Berta S., Buat V., Cooray A., Cresci G., Daddi E., Farrah D., Fontana A., Franceschini A., Genzel R., Granato G., Grazian A., Le Floc'h E., Magdis G., Magliocchetti M., Mannucci F., Menci N., Nordon R., Oliver S., Popesso P., Pozzi F., Riguccini L., Rodighiero G., Rosario D. J., Salvato M., Scott D., Silva L., Tacconi L., Viero M., Wang L., Wuyts S., Xu K., 2014. A&A, **562**, A30. *The evolution of the dust and gas content in galaxies*.

Schaye J., Crain R. A., Bower R. G., Furlong M., Schaller M., Theuns T., Dalla Vecchia C., Frenk C. S., McCarthy I. G., Helly J. C., Jenkins A., Rosas-Guevara Y. M., White S. D. M., Baes M., Booth C. M., Camps P., Navarro J. F., Qu Y., Rahmati A., Sawala T., Thomas P. A., Trayford J., 2015. MNRAS, **446**, 521. *The EAGLE project: simulating the evolution and assembly of galaxies and their environments*.

Schechter P., 1976. *ApJ*, **203**, 297. *An analytic expression for the luminosity function for galaxies.*

Sellwood J. A., Kahn F. D., 1991. MNRAS, **250**, 278. *Spiral modes driven by narrow features in angular-momentum density*.

Sérsic J. L., 1968. *Atlas de galaxias australes*.

Shen S., Mo H. J., White S. D. M., Blanton M. R., Kauffmann G., Voges W., Brinkmann J., Csabai I., 2003. MNRAS, **343**, 978. *The size distribution of galaxies in the Sloan Digital Sky Survey*.

Simard L., Mendel J. T., Patton D. R., Ellison S. L., McConnachie A. W., 2011. *ApJs*, **196**, 11. *A Catalog of Bulge+disk Decompositions and Updated Photometry for 1.12 Million Galaxies in the Sloan Digital Sky Survey*.

Simmons B. D., Urry C. M., 2008. ApJ, **683**, 644. *The Accuracy of Morphological Decomposition of Active Galactic Nucleus Host Galaxies*.

Simmons B. D., Lintott C., Willett K. W., Masters K. L., Kartaltepe J. S., Häußler B., Kaviraj S., Krawczyk C., Kruk S. J., McIntosh D. H., Smethurst R. J., Nichol R. C., Scarlata C., Schawinski K., Conselice C. J., Almaini O., Ferguson H. C., Fortson L., Hartley W., Kocevski D., Koekemoer A. M., Mortlock A., Newman J. A., Bamford S. P., Grogin N. A., Lucas R. A., Hathi N. P., McGrath E., Peth M., Pforr J., Rizer Z., Wuyts S., Barro G., Bell E. F., Castellano M., Dahlen T., Dekel A., Ownsworth J., Faber S. M., Finkelstein S. L., Fontana A., Galametz A., Grützbauch R., Koo D., Lotz J., Mobasher B., Mozena M., Salvato M., Wiklind T., 2017. MNRAS, **464**, 4420. *Galaxy Zoo: quantitative visual morphological classifications for 48 000 galaxies from CANDELS*.

Springel V., White S. D. M., Jenkins A., Frenk C. S., Yoshida N., Gao L., Navarro J., Thacker R., Croton D., Helly J., Peacock J. A., Cole S., Thomas P., Couchman H., Evrard A., Colberg J., Pearce F., 2005. Nature, **435**, 629. *Simulations of the formation, evolution and clustering of galaxies and quasars*.

Strateva I., Ivezić Ž., Knapp G. R., Narayanan V. K., Strauss M. A., Gunn J. E., Lupton R. H., Schlegel D., Bahcall N. A., Brinkmann J., Brunner R. J., Budavári T., Csabai I., Castander F. J., Doi M., Fukugita M., Győry Z., Hamabe M., Hennessy G., Ichikawa T., Kunszt P. Z., Lamb D. Q., McKay T. A., Okamura S., Racusin J., Sekiguchi M., Schneider D. P., Shimasaku K., York D., 2001. AJ, **122**, 1861. *Color Separation of Galaxy Types in the Sloan Digital Sky Survey Imaging Data*.

Taniguchi Y., Scoville N., Murayama T., Sanders D. B., Mobasher B., Aussel H., Capak P., Ajiki M., Miyazaki S., Komiyama Y., Shioya Y., Nagao T., Sasaki S. S., Koda J., Carilli C., Giavalisco M., Guzzo L., Hasinger G., Impey C., LeFevre O., Lilly S., Renzini A., Rich M., Schinnerer E., Shopbell P., Kaifu N., Karoji H., Arimoto N., Okamura S., Ohta K., 2007. ApJS, **172**, 9. *The Cosmic Evolution Survey (COSMOS): Subaru Observations of the HST Cosmos Field*.

Taniguchi Y., Kajisawa M., Kobayashi M. A. R., Shioya Y., Nagao T., Capak P. L., Aussel H., Ichikawa A., Murayama T., Scoville N. Z., Ilbert O., Salvato M., Sanders D. B. B., Mobasher B., Miyazaki S., Komiyama Y., Le Fèvre O., Tasca L., Lilly S., Carollo M., Renzini A., Rich M., Schinnerer E., Kaifu N., Karoji H., Arimoto N., Okamura S., Ohta K., Shimasaku K., Hayashino T., 2015. PASJ, **67**, 104. *The Subaru COSMOS 20: Subaru optical imaging of the HST COSMOS field with 20 filters*.*

Taylor-Mager V. A., Conselice C. J., Windhorst R. A., Jansen R. A., 2007. *ApJ*, **659**, 162. *Dependence of Galaxy Structure on Rest-Frame Wavelength and Galaxy Type*.

Toft S., van Dokkum P., Franx M., Labbe I., Förster Schreiber N. M., Wuyts S., Webb T., Rudnick G., Zirm A., Kriek M., van der Werf P., Blakeslee J. P., Illingworth G., Rix H.-W., Papovich C., Moorwood A., 2007. ApJ, **671**, 285. *Hubble Space Telescope and Spitzer Imaging of Red and Blue Galaxies at $z \sim 2.5$: A Correlation between Size and Star Formation Activity from Compact Quiescent Galaxies to Extended Star-forming Galaxies*.

Toomre A. *Gas-hungry Sc spirals.*, p. 292. 1990.

Trujillo I., Feulner G., Goranova Y., Hopp U., Longhetti M., Saracco P., Bender R., Braito V., Della Ceca R., Drory N., Mannucci F., Severgnini P., 2006. *MNRAS*, **373**, L36. *Extremely compact massive galaxies at $z \sim 1.4$.*

Trujillo I., Conselice C. J., Bundy K., Cooper M. C., Eisenhardt P., Ellis R. S., 2007. *MNRAS*, **382**, 109. *Strong size evolution of the most massive galaxies since $z \sim 2$.*

van der Wel A., Bell E. F., Häussler B., McGrath E. J., Chang Y.-Y., Guo Y., McIntosh D. H., Rix H.-W., Barden M., Cheung E., Faber S. M., Ferguson H. C., Galametz A., Grogin N. A., Hartley W., Kartaltepe J. S., Kocevski D. D., Koekemoer A. M., Lotz J., Mozena M., Peth M. A., Peng C. Y., 2012. *ApJs*, **203**, 24. *Structural Parameters of Galaxies in CANDELS*.

van der Wel A., Franx M., van Dokkum P. G., Skelton R. E., Momcheva I. G., Whitaker K. E., Brammer G. B., Bell E. F., Rix H.-W., Wuyts S., Ferguson H. C., Holden B. P., Barro G., Koekemoer A. M., Chang Y.-Y., McGrath E. J., Häussler B., Dekel A., Behroozi P., Fumagalli M., Leja J., Lundgren B. F., Maseda M. V., Nelson E. J., Wake D. A., Patel S. G., Labbé I., Faber S. M., Grogin N. A., Kocevski D. D., 2014. *ApJ*, **788**, 28. *3D-HST+CANDELS: The Evolution of the Galaxy Size-Mass Distribution since $z = 3$.*

van Dokkum P. G., Whitaker K. E., Brammer G., Franx M., Kriek M., Labbé I., Marchesini D., Quadri R., Bezanson R., Illingworth G. D., Muzzin A., Rudnick G., Tal T., Wake D., 2010. *ApJ*, **709**, 1018. *The Growth of Massive Galaxies Since $z = 2$.*

van Dokkum P. G., Bezanson R., van der Wel A., Nelson E. J., Momcheva I., Skelton R. E., Whitaker K. E., Brammer G., Conroy C., Förster Schreiber N. M., Fumagalli M., Kriek M., Labbé I., Leja J., Marchesini D., Muzzin A., Oesch P., Wuyts S., 2014. *ApJ*, **791**, 45. *Dense Cores in Galaxies Out to $z = 2.5$ in SDSS, UltraVISTA, and the Five 3D-HST/CANDELS Fields*.

van Rijsbergen C., 1979. *Information Retrieval*, Butterworth-Heinemann.

Vogelsberger M., Genel S., Springel V., Torrey P., Sijacki D., Xu D., Snyder G., Nelson D., Hernquist L., 2014. MNRAS, **444**, 1518. *Introducing the Illustris Project: simulating the coevolution of dark and visible matter in the Universe*.

Vulcani B., Bamford S. P., Häußler B., Vika M., Rojas A., Agius N. K., Baldry I., Bauer A. E., Brown M. J. I., Driver S., Graham A. W., Kelvin L. S., Liske J., Loveday J., Popescu C. C., Robotham A. S. G., Tuffs R. J., 2014. MNRAS, **441**, 1340. *Galaxy And Mass Assembly (GAMA): the wavelength-dependent sizes and profiles of galaxies revealed by MegaMorph*.

Whitaker K. E., Labbé I., van Dokkum P. G., Brammer G., Kriek M., Marchesini D., Quadri R. F., Franx M., Muzzin A., Williams R. J., Bezanson R., Illingworth G. D., Lee K.-S., Lundgren B., Nelson E. J., Rudnick G., Tal T., Wake D. A., 2011. ApJ, **735**, 86. *The NEWFIRM Medium-band Survey: Photometric Catalogs, Redshifts, and the Bimodal Color Distribution of Galaxies out to* $z \sim 3$.

Whitaker K. E., van Dokkum P. G., Brammer G., Franx M., 2012. ApJ, **754**, L29. *The Star Formation Mass Sequence Out to* $z = 2.5$.

Windhorst R. A., Cohen S. H., Hathi N. P., McCarthy P. J., Ryan, Jr. R. E., Yan H., Baldry I. K., Driver S. P., Frogel J. A., Hill D. T., Kelvin L. S., Koekemoer A. M., Mechtley M., O'Connell R. W., Robotham A. S. G., Rutkowski M. J., Seibert M., Straughn A. N., Tuffs R. J., Balick B., Bond H. E., Bushouse H., Calzetti D., Crockett M., Disney M. J., Dopita M. A., Hall D. N. B., Holtzman J. A., Kaviraj S., Kimble R. A., MacKenty J. W., Mutchler M., Paresce F., Saha A., Silk J. I., Trauger J. T., Walker A. R., Whitmore B. C., Young E. T., 2011. ApJS, **193**, 27. *The Hubble Space Telescope Wide Field Camera 3 Early Release Science Data: Panchromatic Faint Object Counts for 0.2-2* μ*m Wavelength*.

Wolf C., Gray M. E., Meisenheimer K., 2005. A&A, **443**, 435. *Red-sequence galaxies with young stars and dust: the cluster Abell 901/902 seen with COMBO-17*.

Zhao D., Aragón-Salamanca A., Conselice C. J., 2015. *MNRAS*, **448**, 2530. *The link between morphology and structure of brightest cluster galaxies: automatic identification of cDs*.

Zwicky F., 1933. *Helvetica Physica Acta*, **6**, 110. *Die Rotverschiebung von extragalaktischen Nebeln*.